Tunable and Broadband Nanostructured Photonic Devices: Fabrication and Characterization

THÈSE N^{O} 4724 (2010)

PRÉSENTÉE LE 9 JUILLET 2010
À LA FACULTÉ SCIENCES ET TECHNIQUES DE L'INGÉNIEUR
INSTITUT DE MICROTECHNIQUE
SECTION DE MICROTECHNIQUE

ÉCOLE POLYTECHNIQUE FÉDÉRALE DE LAUSANNE

POUR L'OBTENTION DU GRADE DE DOCTEUR ÈS SCIENCES

PAR

Pierre-Yves BARONI

acceptée sur proposition du jury:

Prof. O. Martin, président du jury
Prof. H. P. Herzig , directeur de thèse
Prof. J. Jacot, rapporteur
Prof. W. Nakagawa, rapporteur
Dr. L. Sirigu, rapporteur

ÉCOLE POLYTECHNIQUE
FÉDÉRALE DE LAUSANNE

Lausanne, EPFL
2010

Résumé

Le sujet principal de cette thèse est la fabrication et la caractérisation de structures plus petites que la longueur d'onde de la lumière dans sa gamme visible ou infra-rouge.

Dans un premier temps, la création de structures périodiques uni- et bi-dimensionelles par une technique de photolithographie interférentielle est détaillée. Les périodicités fabriquées par ce procédé vont de 270 nm à quelques micromètres sur des surfaces allant jusqu'à 100 cm^2 et pour des profondeurs équivalant à la période.

Un réseau carré de pilliers de 270 nm de période a notamment été créé à la surface d'un réseau de microlentilles en quartz pour obtenir une atténuation de la réflectivité. Les mesures effectuées montrent une diminution de 15 % de la réflection et une augmentation de 3 % de la transmission de la lumière dans le spectre du visible.

La deuxième partie du manuscrit décrit les résultats expérimentaux (dans l'infrarouge) obtenus sur deux structures fabriquées par photolithographie à faisceau d'électrons (e-beam), de type cristal photonique. La première, un superprisme, est une structure de piliers de périodicité triangulaire recouverte de cristaux liquides dont dont le déplacement du spot de sortie de la lumière est de 20.5 μ pour une variation de la longueur d'onde de 27 nm. la longueur de la structure est de 70 μm. les propriétés de dispersion de la lumière sont équivalentes à celles d'un prisme de quartz dont les dimensions seraient 100 fois supérieures. La technologie *silicone* utilisée devrait permettre une parfaite intégration, en tant que multiplexeur/démultiplexeur, dans un micro-circuit optique. La seconde, une cavité résonante réglable, est un filtre ne laissant passer qu'une petite gamme de longueur d'onde dans l'infrarouge. La zone active est constituée d'un guide d'onde photonique composé de trous de périodicité triangulaire incluant des défauts de linéarité faisant office de cavité. La modulabilité du système est obtenue grâce à l'infiltration de cristaux liquides. Le déplacement du pic de lumière transmise à l'intérieur de la bande interdite est de 32 nm lorsque la température passe de l'ambiante à 45 °C.

Mots clés:
Nanostructures périodiques, photolithographie interférentielle, surface anti-reflet, cristaux photoniques, superprisme, cavité résonante.

Abstract

The main topic of this thesis is the fabrication and characterization of structures smaller than the wavelength of light, for operation in the visible or near infrared spectral range.

In the first part of this thesis, the fabrication of periodic structures in one and two dimensions with an interference photolithography technique is described in detail. The structure periodicities that have been fabricated with this process ranges between 270 nm and a few microns on areas that can be as large as 100 cm^2. Typical structure thicknesses are approximately equal to the period.

In particular, a square lattice of pillars with a period of 270 nm has been created on the (non-flat) surface of a quartz microlens array and exhibits anti-reflective properties. Experimental results show a 15 % attenuation of the reflectivity and a 3 % enhancement of the transmissivity over the visible spectral range.

In the second part of the thesis the structures are fabricated by e-beam lithography to ensure very precise devices shapes. The experimental results are obtained in the infrared range with two different structures, called photonic crystals. The first structure, a superprism, is a triangular lattice of pillars infiltrated by liquid crystals. A displacement of the output light spot is measured to be 20.5 μm for a wavelength variation of 27 nm. The structure length is 70 μm. The device, based on standard silicon technology, should allow integration of the device as a multiplexer/demultiplexer system into optical micro-circuits. The second structure, a tunable resonant cavity, is a wavelength filter working in the near infrared spectrum. The active area is composed of a photonic waveguide with a triangular lattice made of sub-micrometer holes. Additional nanostructuring in the light waveguide acts as a resonant cavity. The tunability of the device is obtained due to the liquid crystals which are infiltrated into the nanostructure. A 32 nm shift of the transmitted light peak inside the photonic band gap is measured by changing the temperature from room temperature to 45 °C.

Key words:
Periodic nanostructures, interference photolithography, anti-reflective surfaces, photonic crystals, superprism, resonant cavity.

Contents

Chapter 1

Introduction

Over the past few decades, technological advances have enabled the investigation of the interactions of electromagnetic waves with nano scale structures in both the theoretical and experimental domains. Nanostructures are defined to have, at least one dimension in the range of one to a few hundred nanometers. Such miniaturization allows the integration of a large number of functionalities on areas that can be smaller than one square millimeter for electronic and optical purposes. Furthermore, in photonics, many useful properties of nanostructures arise when their dimensions are comparable or smaller than the wavelength with which they are designed to operate. The range of potential applications for these nanostructures is extremely broad. Examples that illustrate this diversity include engineered metamaterials for optimized optical properties, the enhancement of solar cell efficiency, and extremely strongly confined optical field emitters for high-resolution optical imaging and high-sensitivity detection.

In particular, periodic photonic structures possess a number of interesting properties, and are the focus of this work. When the period is greater than the wavelength of the incident light, classical diffraction gratings [1] are obtained. When the period is subwavelength, the properties of the nanostructures can be separated into two groups that will both be treated in this thesis: photonic crystals (PhCs) and the artificial refractive index materials. The first case is that of the PhC, where resonance effects between the wavelength of the optical fields and the period of the nanostructure result in a number of interesting and useful phenomena (similar to an electronic semiconductor). The second case is the artificial refractive index material, where the effective optical properties of a composite nanostructure can be engineered through the choice and layout of the constituent materials.

In 1888, Lord Rayleigh first described [2] a phenomenon that, one century later would come to be named photonic crystals, after Yablonovitch and John published two milestone articles [3,4]. PhCs are composed of periodic dielectric or metallo-dielectric nanostructures that affect the propagation of light by introducing allowed and forbidden energy bands. Consequently, PhCs allow control over the light propagation within a small volume.

A one-dimensional example of a PhCs is the Bragg mirror, formed by a periodic modulation of the refractive index along the light propagation direction. The many reflections created by such a structure interfere constructively and destructively forbidding the propagation of light for a specific wavelength range and state of polarization. By appropriately selecting the materials and thicknesses, one can obtain dielectric mirrors [5] or fiber Bragg gratings [6] that can have specific behavior with respect to the wavelength. Another applications of one-dimensional PhCs is the Vertical Cavity Surface Emitting Laser (VCSEL) [7] where Bragg reflectors are used to confine light for an integrated laser cavity.

By adding periodicity in a second direction, one creates two-dimensional PhCs. First used as filters [8] due to the band gap exhibited by PhC's, they have enabled a large range of integrated optical components such as complex waveguides [9–11], lasers [12,13], cavities [14,15], modulators [16–18], switches [19] and superprisms [20–22] for multiplexing and demultiplexing. At the same time, the tunability of these devices remains a challenge and several techniques have been used in order to make tunable PhCs, such as acousto-optic [23] or electro-optic [24] effects, nonlinear properties of the materials or thermal [25] effects. The tunability of a resonant peak by modifying the cavity holes geometry and infiltrating liquid crystals has already been observed [26]. Nevertheless, experimental demonstration of tunable cavities using liquid crystal properties are still rare [27,28].

There are many groups that have realized 2-D PhCs devices in semiconductors [29–41] either as freestanding membranes or on solid substrates. Different materials have been used and single components or devices have been realized [42–45].

Preliminary reports on fabricated three dimensional PhCs can be found at the end of the last century where the three principal fabrication methods are: layer-by-layer fabrication using a lithographic approach [46,47], colloidal self-assembly [48] and holographic lithography technology [49]. Nevertheless, due to available technology, the majority of the studies in this field address two dimensional PhCs. The structures have become feasible with higher and higher resolution over the last two decades thanks to highly capable processes such as focused ion beam, electron beam lithography, phase mask lithography and laser beam interference structuring. This has enabled the miniaturization of electronic and optical components as well as building complex devices directly on chip.

Note that subwavelength periodic structures can also provide amazing color properties that can be found in nature, for example in insect wings [50,51], and that can be mimicked [52]. If the interference pattern of the light diffracted by these complex structures create angularly dependent colors, simpler, well designed, two-dimensional structures on the surface of a device can exhibit antireflective properties by creating a thin layer with an artificial effective refractive index.

This work explores a number of relatively new concepts and methods in photonic nanostructure fabrication and design. Specifically, two types of device are investigated: structures fabricated over large areas using optical interference lithography; and devices based on PhCs fabricated using standard semiconductor technology and modulated using infiltrated liquid crystals. A more detailed description of each chapter of the thesis is given below.

Chapter 2 presents a method to fabricate nanostructures that uses the coherence properties of an ultra-violet laser to produce an interference pattern. This light pattern is used as an exposure mask for the photoresist layer. This technique can be compared to a standard contact mask photolithography process. The main advantage is that there is no physical contact with the photoresist surface. Therefore it is compatible with non-planar surfaces. Moreover, the achievable resolution is on the order of a few hundreds of nanometers (directly related to the illumination wavelength), whereas it is barely below one micrometer for the standard mask lithography process. Since the structures fabricated with the aid of this interference photolithography process are by nature periodic, we have developed methods to locally alter the periodicity in order to produce different kinds of devices. The desirable properties of this technique are the large area (several square centimeters) that can be produced quite quickly and at relatively low cost. Nevertheless, the resolution of the fabricated structures is not as good as obtained by e-beam writing. A crucial point is that the periodic structure is not sufficient to realize many (more complex) devices. It is necessary to modify the PhC locally to make functional elements [53]. A method for direct writing of defects (local suppression of the nanostructures) has been developed to be easily combined with the interference photolithography process using a microscope stand, a UV lamp and an X - Y piezo-electric translation stage.

In chapter 3, a subwavelength-scale square lattice optical nanostructure is fabricated using an interference photolithography process on the surface of a quartz microlens array. This nanostructuring of the quartz surface introduces an antireflective effect, reducing reflectivity between 10% and 30% and enhancing the transmissivity by 3% over the visible spectrum. This approach permits fast fabrication on a 4-inch wafer covered with microlenses (a non-flat surface) and produces monolithic devices which are robust to adverse conditions such as temperature variations.

In chapter 4, the strong dispersion of light due to band-edge effects in the PhC, called the superprism effect, is demonstrated theoretically and experimentally with good agreement. The device, fabricated by e-beam lithography on a Silicon On Insulator (SOI) wafer, has been designed to work in the telecommunications wavelength range. It is composed of a triangular lattice of pillars surrounded by input and output waveguides. The experimental results show a wavelength-dependent transverse beam deflection of 0.74 μm / nm with an active length of the device of 70 μm. This miniaturization, compared to a monolithic material, and the use of standard silicon technology opens the door to fully integrated multiplexer/demultiplexer systems.

In Chapter 5, we report on the fabrication and optical characterization of a tunable

PhC nanocavity actuated by liquid crystals. This device acts as a filter, presenting a moveable transmission peak in the telecom wavelength band (around $\lambda = 1550$ nm). Passing from the anisotropic (oriented crystals) to the anisotropic state of the liquid crystals, a shift of $\Delta\lambda = 13$ nm has been measured, which confirms the theoretical predictions obtained by finite integral time domain simulations. This tunable optical filter based on PhC nanocavities, liquid crystal infiltration, and standard fabrication technologies may have applications in areas such as optical communications, spectroscopy, and environmental monitoring.

Finally, a short conclusion is given in chapter 6.

List of published papers:

P.-Y. Baroni, B. Päivänranta, T. Scharf, W. Nakagawa, M. Roussey, M. Kuittinen, and Herzig, H. P. *Nanostructured surface fabricated by laser interference lithography to attenuate the reflectivity of microlens arrays*, JEOS-RP., **5**, 10006 (2010).

B. Päivänranta, M. Pudas, O. Pitkanen, K. Leinonen, M. Kuittinen, P.-Y. Baroni, T. Scharf, and H.-P. Herzig, *Liquid phase deposition of polymers on arbitrary shaped surfaces and their suitability for e-beam patterning*, Nanotechnology **20**(22), 225305 (2009).

B. Päivänranta, P.-Y. Baroni, T. Scharf, W. Nakagawa, M. Kuittinen, and H. P. Herzig, *Antireflective nanostructured microlenses*, Microelectronic Engineering, **85**(5-6), 1089-1091 (2008).

P.-Y. Baroni, T. Scharf and H.P. Herzig, *Fabrication of large-area two-dimensional photonic crystals using interference lithography and direct writing of defects*, Photonic Crystal Materials and Devices III, SPIE-The International Society for Optical Engineering, Bellingham, USA, 2006, 61821V-1-61821V-9.

List of submitted papers:

P.-Y. Baroni, V. Paeder, Y.-C. Chang, M. Roussey, W. Nakagawa, and H. P. Herzig, *Demonstration of superprism effect in silicon pillar 2D photonic crystal infiltrated with liquid crystals*, Opt. Ing..

P.-Y. Baroni, Q. Tan, V. Paeder, A. Cosentino, M. Roussey, T. Scharf, W. Nakagawa, and H. P. Herzig, *Tunable photonic crystal cavity by liquid crystal infiltration*, JEOS-RP.

List of conference presentations:

Fourth International Conference on Surface Plasmon Photonics (SPP4), *Near infrared superprism effect in a hexagonal photonic crystal made of silicon pillars* (Poster), June 21st - 26th, 2009, Amsterdam, The Netherlands.

European Optical Society (EOS) Annual Meeting 2008, *Antireflective nanostructured microlenses in quartz* (Talk), September 29th - October 2nd, 2008, Paris, France.

Society of Photographic Instrumentation Engineers (SPIE) Photonics Europe 2006, *Fabrication of large-area two-dimensional photonic crystals using interference lithography and direct writing of defects* (Talk), April 3rd - 7th, 2006, Strasbourg, France.

Laboratoire européen associé en microtechniques (LEA) fourth edition, *Direct fabrication of 2-D photonic crystals by holography and nanostructuration* (Poster), September 8th - 9th, 2005, Arcs et Senans, France.

Chapter 2

Periodic micro and nano structuring using interference lithography

2.1 Introduction

Interference lithography is a powerful method to produce periodic structures on large surfaces. In this chapter, we describe the basic process (Lloyd's mirror configuration [54, 55]), which we use to fabricate one and two dimensional gratings. We also show methods to modify locally the periodicity and to select the shape of the working areas. These techniques are summarized in Table 2.1.

	Elements	**Dimension**	**Techniques**
I	Waveguides	Macro	Mask lithography Micro mask lithography
II	Active area shaping	Micro	Micro mask lithography
III	Periodic structures	Nano	Interference lithography
IV	Alteration of the periodic structure	Nano	Direct writing microscope lithography

Table 2.1: Overview of the techniques presented in this chapter to fabricate macro, micro and nano structures.

Figure 2.1 presents two examples of fabricated structures where the roman number identify which techniques are used according to Table 2.1. The SEM image shown in Fig. 2.1 a) is a photonic crystal slab made of silicon pillars, with a half circle like shape where we observe one SU8 waveguide on the right and several on the left. Figure 2.1 b) shows an triangular photonic crystal slab made of 700 nm high silicon pillars with a submicron periodicity. One observe an horizontal line in the center of the image where the pillars have been erased. Problems specific to these techniques are discussed and finally, results of transferring structures into optical materials are presented.

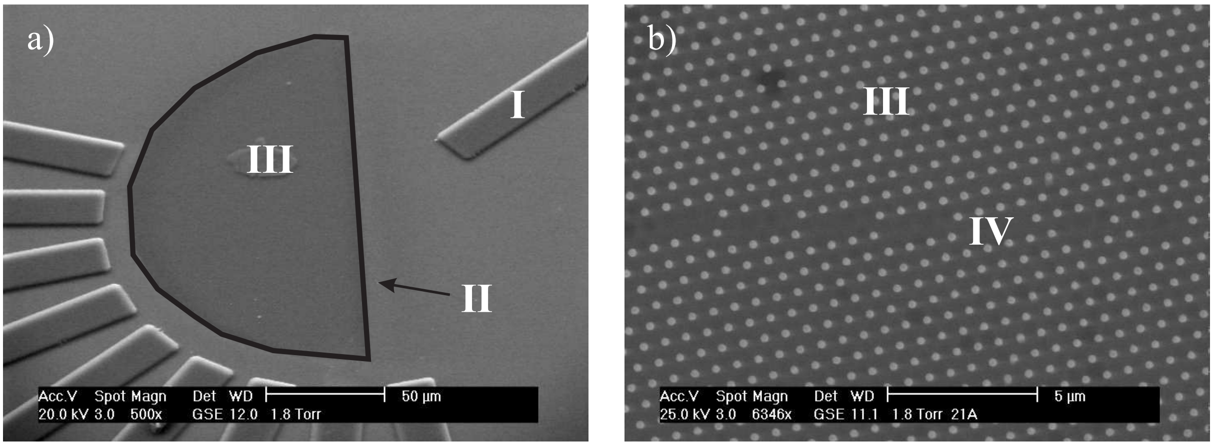

Figure 2.1: Sem pictures of fabricated structures where the techniques used to fabricate the different parts of the devices are evidenced. a) Half circle selection of submicron triangular grating made of silicon with SU8 waveguides. b) Submicron triangular grating made of silicon pillars with removed pillars

2.2 Description of the experiment

Principle

We have developed a process for the direct fabrication of one and two dimensional gratings on large area surfaces. The substrate (glass, quartz, silicon, multilayer, ...) is selected depending on the targeted application of the structures. The schematic in Fig. 2.2 presents the different steps of our process. The positive photoresist, Clariant AZ^{R} 1518 used for all experiments, is spun onto a substrate. It is then pre-baked in an oven at 40°C for 30

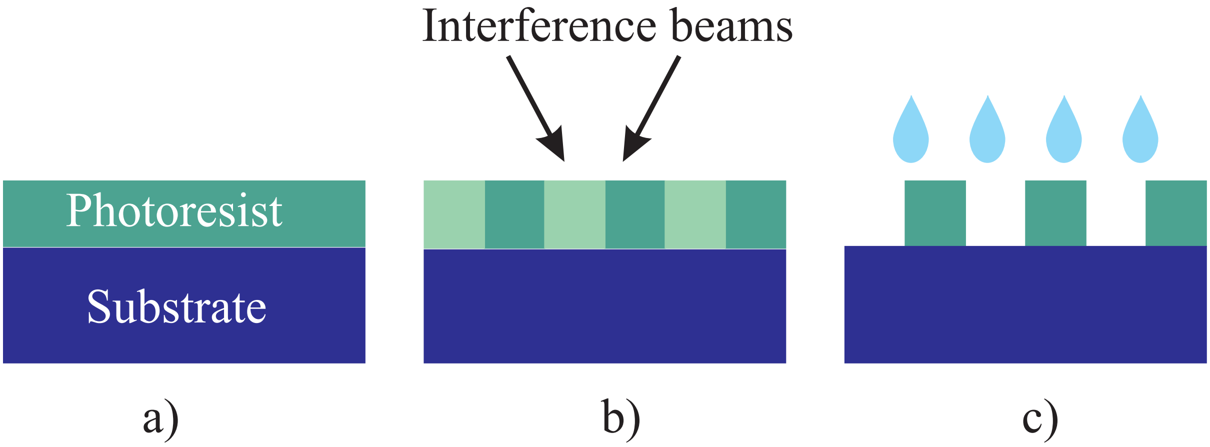

Figure 2.2: Scheme of the interference lithography process used to create gratings in photoresist. a) The photoresist is spun on the substrate. b) The interferences pattern is recorded. c) The photoresist is developed.

min. and at 50°C for 30 min. Fig. 2.2 a). Then, the wafer is exposed with an interference pattern created by two coherent wavefronts Fig. 2.2 b). In a last step, the photoresist is developed during several minutes Fig. 2.2 c) with a Clariant AZ^R 351B developer diluted in a 1 : 9 proportion for several minutes to preserve high aspect ratio structures. The last step consists of a post-bake of 40 minutes in an oven at 85°C. Note that unwanted back reflections from the substrate can distrub the realized pattern. In that case, techniques presented in Chap. 2.5.3 must be used

Description of the setup

The schematics of the setup used for the fabrication of one and two-dimensional gratings are shown in Fig. 2.3 a) and b) while Fig. 2.3 c) and d) are pictures of the corresponding setup. It is composed of a Krypton laser with the main wavelength at 413 nm, a microscope objective (20X), a 8 μm pinhole and a substrate holder. The laser beam is focalized onto the pinhole with the microscope objective. The beam diverges due to the microscope objective and is spatially filtered by passing through the pinhole. The distance between the pinhole and the substrate holder is approximately 2 m.

Equation (2.1) gives the wavefront curvature of a Gaussian beam. z is the distance between the position of the minimum waist W_0 (very close to the objective) and the substrate. z_0 is the distance where the beam waist $W = \sqrt{2}W_0$. In our situation, $z \gg z_0$, so that the beam curvature is 2 m.

$$R(z) = z[1 + (\frac{z_0}{z})^2] \tag{2.1}$$

An interferential periodic intensity is created at the substrate position by combination of direct light from the pinhole and the light reflected by a mirror positionned at 90° to the sample (Lloyd's mirror configuration) [56] as shown in Fig. 2.3 b). The total intensity composed of the two superimposed beams and the interference pattern intensity is given by the Eq. (2.2) (Ref. [57] page 66):

$$I(y, z, \theta) = 2I_0(1 + cos(\frac{4\pi y}{\lambda} sin(\frac{\theta}{2}))) \tag{2.2}$$

Approximating the beam curvature by a planar wavefront, the grating period (Λ) is selected by adjusting the angle (θ) between the two incident beams following Eq. (2.3). Where λ is the wavelength of the laser and θ the angle between the two incident beams.

$$\Lambda = \frac{\lambda}{2\sin(\frac{\theta}{2})} \tag{2.3}$$

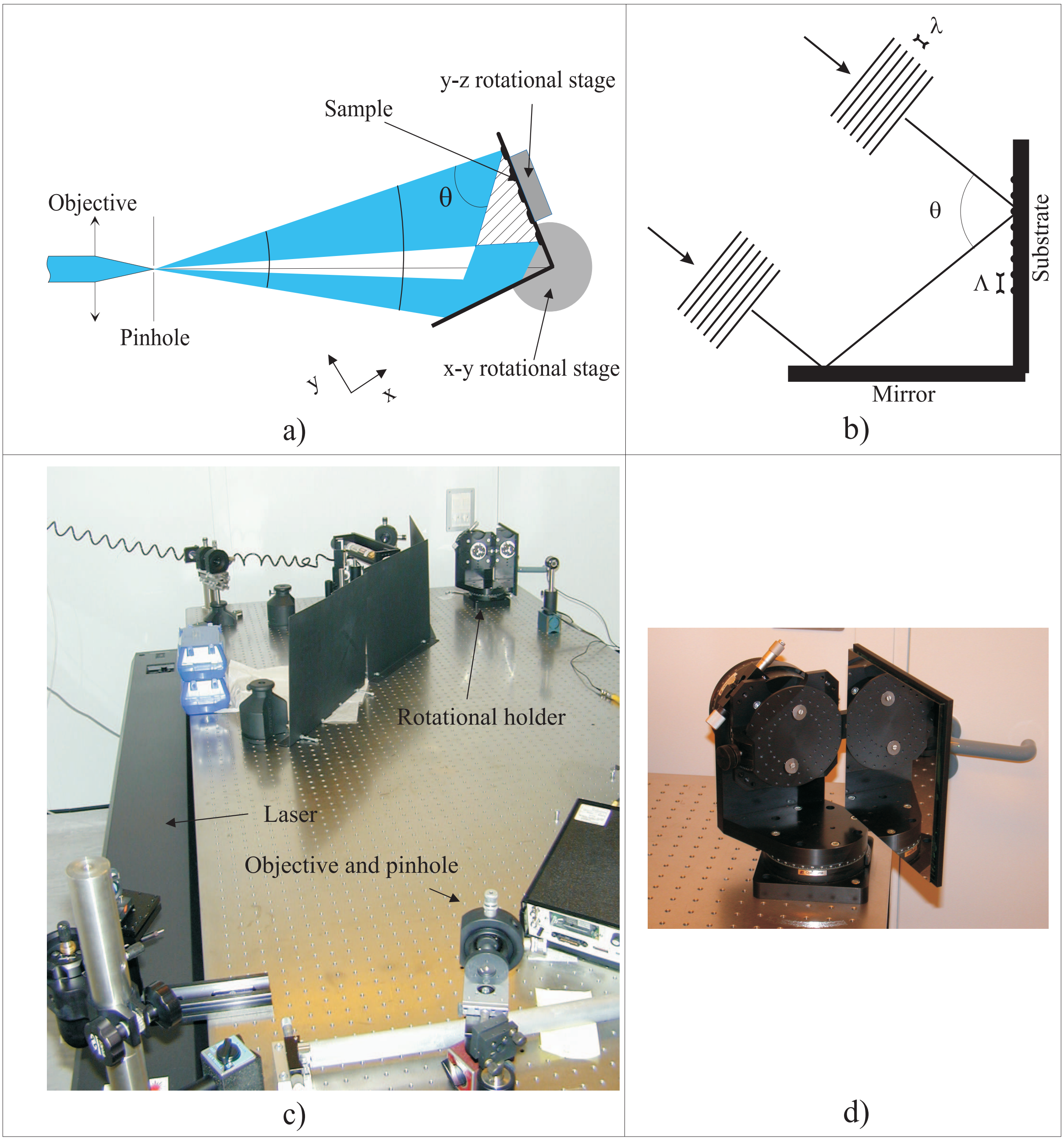

Figure 2.3: a) and c) are scheme and picture of the illumination setup where interference fringes are formed by superposition of direct and reflected light issued from a single diffraction pinhole. b) and d) are scheme and picture from the wafer holder which is composed of a mirror fixed at 90° degrees compared to the wafer position. the wafer can be rotated in plane and the entire system can be rotated around a vertical axis.

In practice, the substrate holder stands on a rotational stage with a vertical axis that allows to change the angle of incidence of the beams onto the substrate. The substrate is mechanically fixed on a disc like holder fitted with three magnetic positioning balls. It can be rotated in the plane and conveniently fixed and removed from the holder.

Note that the exposure time and power must be set precisely in order to have the minimum and maximum intensity of the interference fringes below and above the sensitivity threshold of the photoresist.

2.3 Fabrication of periodic gratings

2.3.1 One-dimensional gratings

One dimensional gratings have been fabricated as a model system using our technique to study our process and to determine the parameters. The characterization of the samples

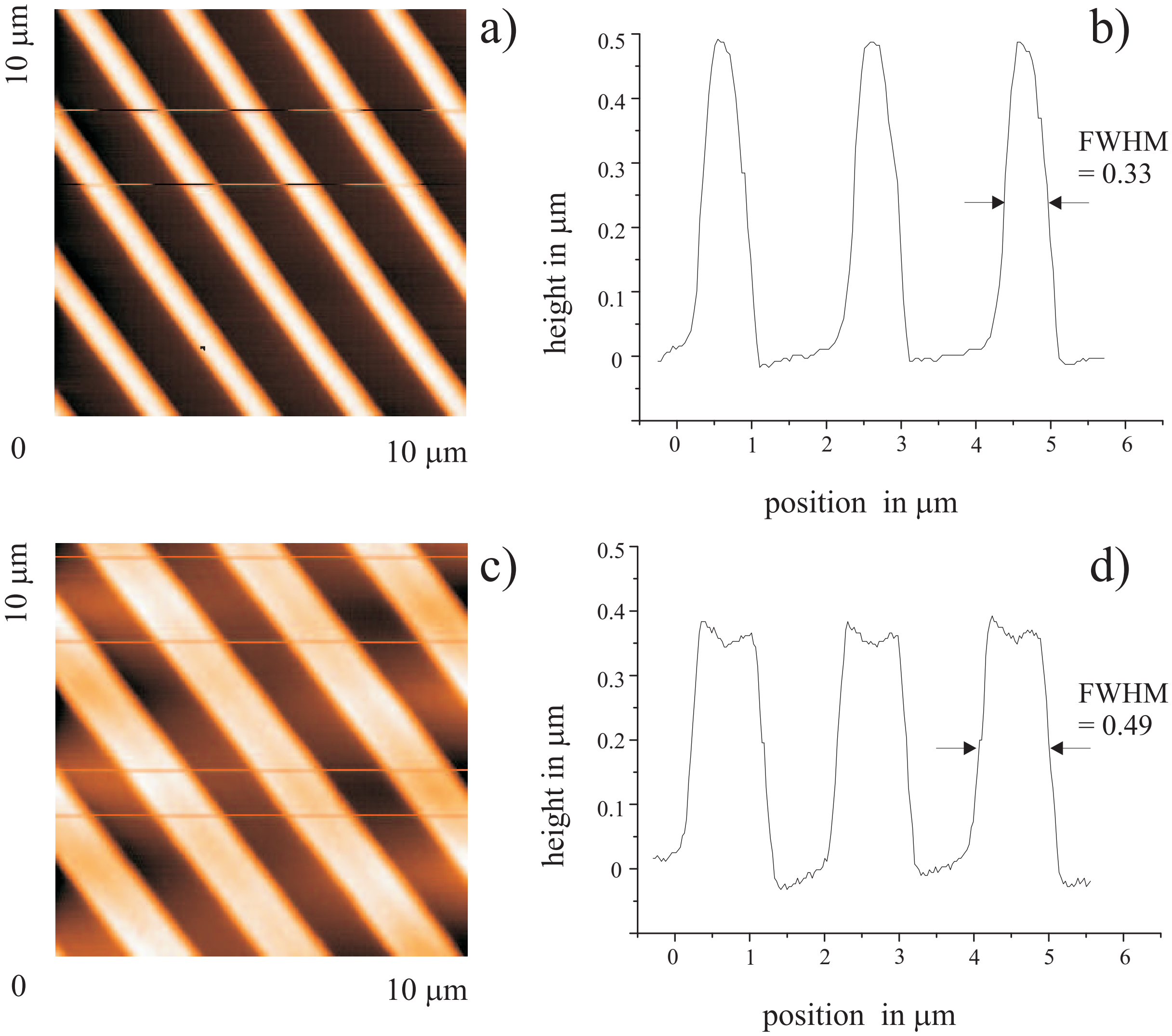

Figure 2.4: a) and c) are AFM images of surface and b) and d) the corresponding profiles for two different exposure doses for one-dimensional gratings in photoresist.

(profile measurements) has been made with an atomic force microscope (AFM) working in dynamic mode. Figure 2.4 presents examples of two gratings and their corresponding profiles.

The fabrication of the gratings starts with the deposition of photoresist onto the substrate. For the fabrication of the structure shown Fig. 2.4, 600 nm of photoresist is spun onto a glass plate and the angle of incidence of the interference beams is set to obtain 2 μm grating period samples. In Fig. 2.4 a) and b), the exposure dose (intensity x time) is 45.5 $\frac{mW}{cm^2}s$. In the first sample, we obtain a ratio between the period and the profile FWHM of 0.325. By decreasing the exposure dose to 40.5 $\frac{mW}{cm^2}s$, this ratio increase to 0.49. At the same time, the profile thickness decreases from 600 nm to 350 nm. In this case, the exposure dose did not allow to obtain a grating for the complete photoresist thickness. It indicates that the photoresist thickness cannot be chosen arbitrarily but in relation with the desired profile shape.

By decreasing the exposure dose down to 30 $\frac{mW}{cm^2}s$, the resulting grating is only 200 nm high. Moreover, the combination of the photoresist light absorbtion and the sinusoidal shape of the interference pattern produces a rounded grating shape as observed in Fig. 2.5. This profile is not expected in some cases (Photonic crystals) but acceptable or even targeted in other ones (diffraction gratings, anti reflective surfaces, liquid crystal alignement, ...).

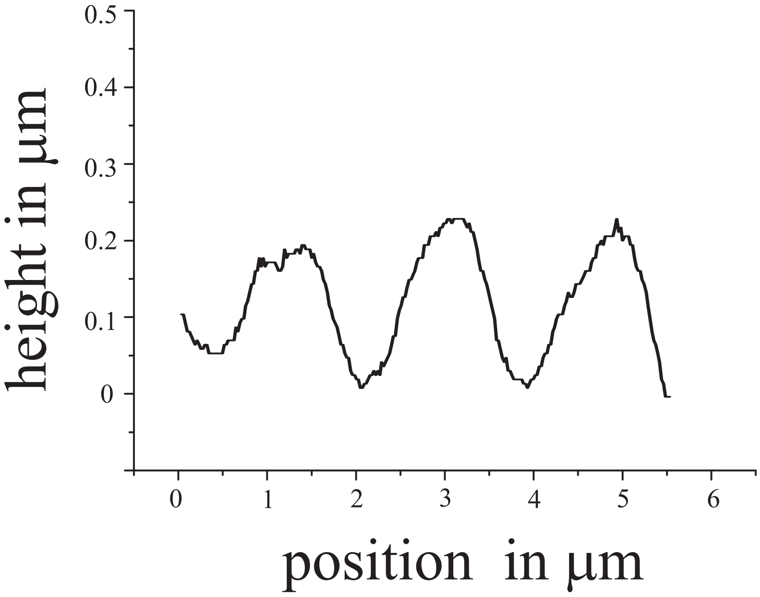

Figure 2.5: AFM measurement of a rounded shape grating produced at the surface of the photoresist layer thanks to the too small exposure dose to develop the photoresist through its entire thickness.

To summarize, it is possible to produce gratings with different profiles from sinusoidal like shape to rectangular like shape by increasing the exposure dose. The photoresist thickness must be chosen in relationship with the targeted shape. Our process allows the fabrication of gratings with periods between 250 nm and a few micrometers. The surface area that can be covered depends on the exposure angle and on the mirror size (20 cm × 20 cm). It is 12 cm for a 250 nm grating and decreases to about 1 cm for a 5 μm grating.

2.3.2 Two-dimensional gratings

To obtain a two-dimensional lattice, the sample is exposed two or three times while rotated in the plane of the wafer with an in-plane rotation angle. Typical exposure times vary between 10 and 30 seconds for an intensity of 1.1 mW/cm^2 on the substrate. The large range of exposure times depends on the thickness of the coated photoresist that can be chosen. Long development times of several minutes at low developer concentrations are chosen to get high aspect ratio structures. With such a process we obtain wafers covered by a two dimensional lattice made of photoresist structures.

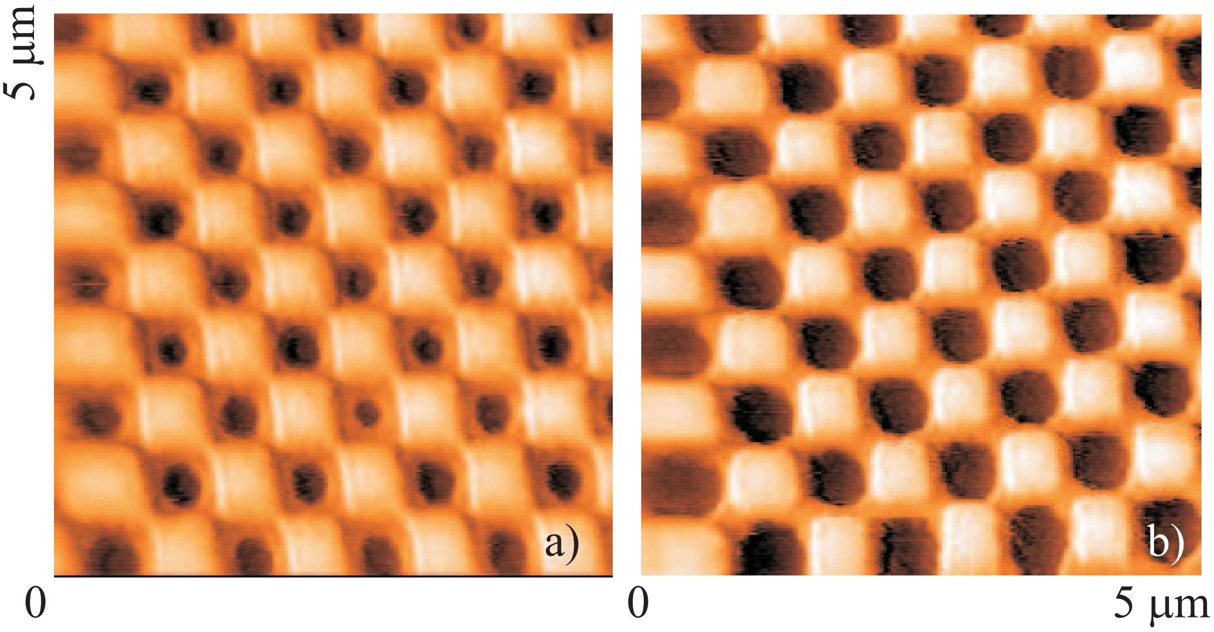

Figure 2.6: AFM mesurements of two dimensional square lattices with two different exposure times. a) The exposure dose is too weak to obtain a square shape over the entire photoresist thickness. b) By increasing the exposure time, a square shape is obtained down to the bottom of the photoresist layer.

The AFM images in Fig. 2.6 show two square lattices obtained by superposition of two exposures while rotating the substrate by 90° degrees. The grating periods are 1 μm in both horizontal and vertical directions. The structures are 730 nm deep, which corresponds to the thickness of spun photoresist. In Fig. 2.6 a), one observes that the photoresist on the bottom is not completely developed (round shape), while in Fig. 2.6 b), the holes are completely open. The difference between the two shapes comes from the exposure time which is two seconds longer in both direction for the second example. Note that the grating period must not necessarily be the same in the two directions. The angle between them can be chosen arbitrarily.

To create lattices with triangular symmetry as shown in Fig. 2.7, the sample is exposed three times while rotated in-plane by 60°. A magnetic sample holder with three small positioning balls is used in order to rotate the sample with a precision good enough to avoid misalignment. This system has a precision better than 0.003 degrees. It should be noted that the accurate alignment of the three exposures and uniformity of the grating period are critical to produce a high-quality, large-area hexagonal PhC pattern.

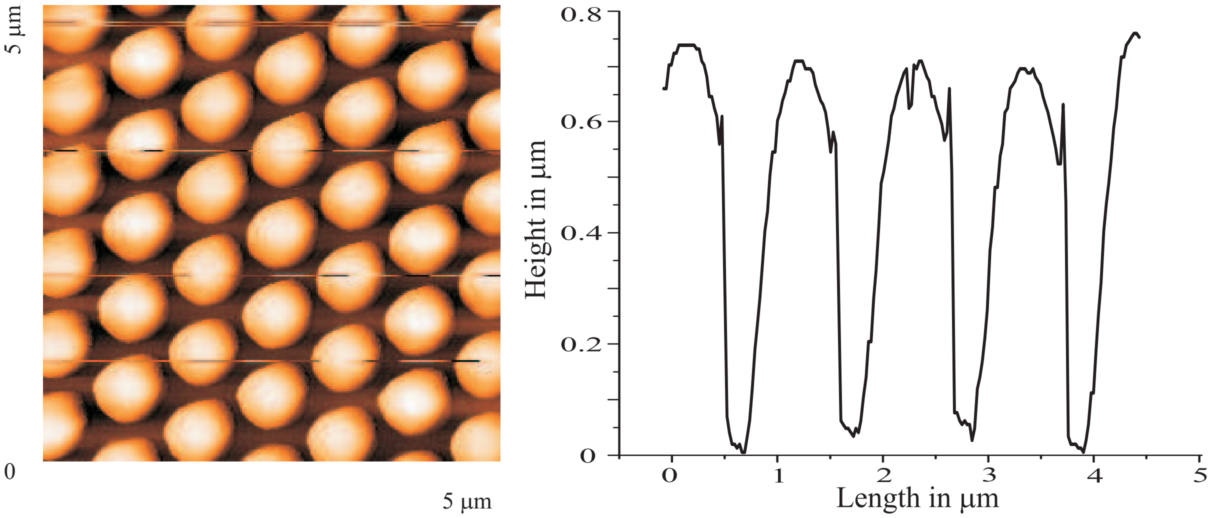

Figure 2.7: Top view and profile, measured by AFM, of a triangular lattice of pillars.

2.3.3 The Moiré effect

In multiple exposures, each exposure leads to a linear grating that can be described by a grating vector Eq. (2.4), where Λ is the periodicity of the grating.

$$||\vec{k}|| = \frac{2\pi}{\Lambda} \tag{2.4}$$

The vector direction is perpendicular to the modulation and its orientation can be chosen arbitrarily. If the vector sum can not be zeroing, because of a deviation of either the grating period or the angular orientation, then a spatial beat frequency results as schematically depicted in Fig. 2.8. Consequently, the resultant exposed pattern in the resist will vary across the sample.

In our experiment, the wavefront, created by the laser beam focused through a pinhole as shown in Fig. 2.3, is spherical. This induces that the angle of incidence of the two

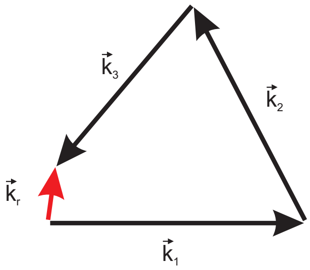

Figure 2.8: The sum of the grating vectors can not be zeroing which induced the existence of a resulting grating vector $\vec{k}_r$.

wavefronts varies slightly along the substrate. Thus, the grating period varies following Eq. (2.3). The Table 2.2 presents the variation of periodicity versus the position on the wafer. In the center of the wafer, we assume to have the targeted period. Note that for a 2 μm period, the mirror size (20 cm) limits the surface where the interference pattern can be created to 2 cm from the substrate center.

Distance from the center	0.2 cm	0.5 cm	1 cm	4 cm
$\Lambda_1 = 300nm$	299.7 nm	299.2 nm	298.5 nm	293.9 nm
$\Lambda_2 = 800nm$	797 nm	793.7 nm	785.6 nm	744.6 nm
$\Lambda_3 = 2000nm$	1981 nm	1954 nm	1910 nm	–

Table 2.2: The table presents the variation of the periodicity for different wavelengths due to the spherical wavefront of the exposure beam.

AFM measurements show that for a grating period of 805 nm in the center, the period increase at 3.5 cm from the center to becomes 860 nm. With a triple illumination at 60°, it produces a concentric spatial beat frequency also called Moiré pattern that is shown in Fig. 2.9.

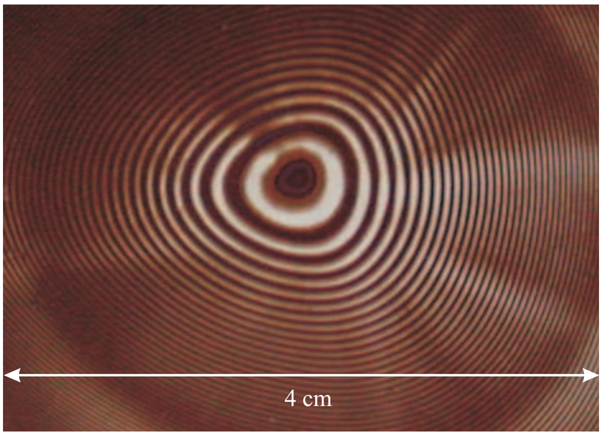

Figure 2.9: Picture of a concentric Moiré pattern produced by a triangular 800 nm period grating, on a 4 inches wafer. The Moiré pattern appears because the wavefront is spherical, rather than planar. The diameter of the uniform central area is about 2 mm.

The grating period variation, produced by the spherical wavefront, also produces a variation of the structures shape depending on the position on the wafer (dark or bright on Fig. 2.9). Thus, the produced structures could vary from pillars [Fig. 2.10 a)], up to round and triangular holes [Fig. 2.10 b) and c)] passing by intermediate structures [Fig. 2.10 d)] depending if the maximum of the three gratings are all in phase or not. It leads to a working area, in the center, of about 2 mm^2, where the photonic crystal is regular and made of pillars if the exposure dose is accurate.

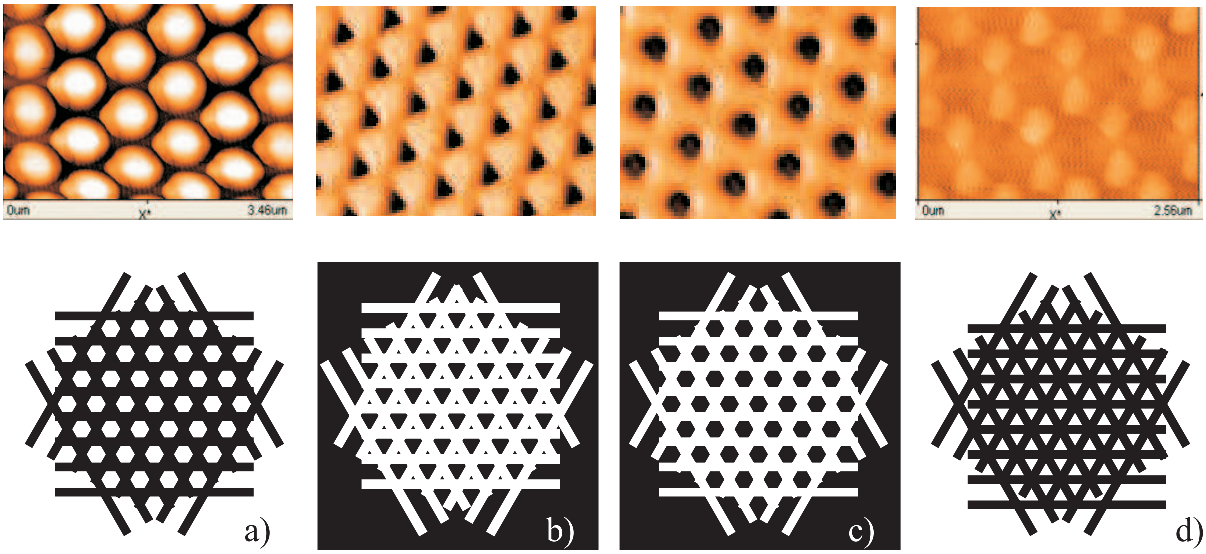

Figure 2.10: AFM images of photonic crystal made of photoresist with its geometrical schema of creation below. Due to the variation of the grating period on the wafer, the structures obtained change depending on the phase of the three gratings. The exposure dose for (c) is lower than for (d) which induces structures where only intersections of the maximal intensity of the fringes have been printed into the PR.

For a better understanding of this effect, a simulation of the interference fringes has been done within Matlab. We considered two punctual sources emitting spherical wave fronts to simulate the direct and reflected illumination. The sources are not exactly symmetric with regards to the normal of the wafer due to the geometrical parameters of the set-up inducing small differences in angle and length for the two optical paths. Superimposing three interference gratings at 60° degrees, we obtain, on the sample surface, an intensity pattern as shown in Fig. 2.11. The sampling needed for a grating period of 800 nm doesn't allow us to simulate the pattern on a surface larger than a few μm^2 with a simple method because of the size of the matrix required. By choosing images of the interference pattern at different positions on the sample surface, we observe two distinct structures: a two dimensional grating made of pillars [Fig. 2.11 a)] and another made of holes [Fig. 2.11 b)] between which intermediate structures made of triangular pillars and holes are found [Fig. 2.11 c)]. To compare the figures found experimentally with the simulations, we must consider that the response of the photoresist is not linear with the exposure dose. It is almost linear only for a certain range of dose. Due to the relatively good match between experiments and simulations, we can state that our chosen exposure dose is close to the linear working zone.

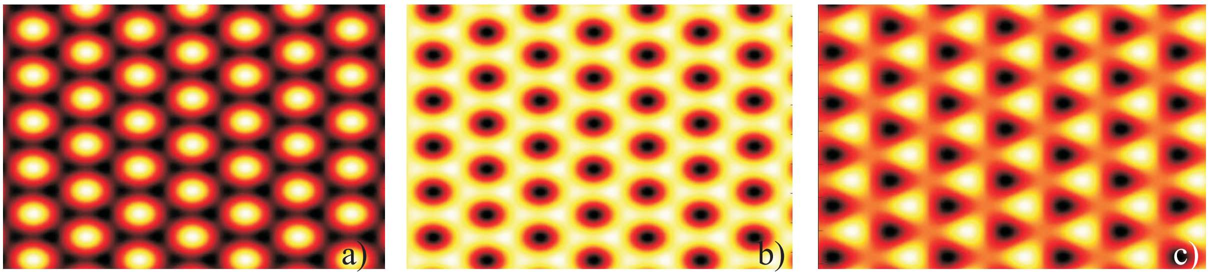

Figure 2.11: Matlab calculated intensity distributions simulating the interference structure with the geometrical parameters of the illumination setup: a) pillars' pattern with grating's period of 800 nm, b) holes' pattern stood 2 mm far from a), c) represents triangular structures standing between a) and b).

2.4 Modification of the grating by additional non standard photolithography or direct writing

In this section, we show how to fabricate structures where the periodicity obtained by the interference lithography process is perturbed. This is crucial to produce devices where defects have to be introduced in the periodicity to obtain the targeted functionality such as photonic waveguides or resonant cavities. An other point is to be able to fabricate structures with particular shape and to fabricate waveguides to access them such as superprism devices (see Chap. 2.5.2). In the following section, we present two processes that we have developed to break the periodicity of the perfect grating and to select a working area and fabricate waveguides.

2.4.1 Introduction of defect in two dimensional grating using an optical microscope

As a first step to produce defects in a photonic crystal lattice, we fabricate a two dimensional grating made of photoresist with interference photolithography. Note that, after the development step, the photoresist is not postbaked so that another lithography step can be performed on the same layer. To produce defects, the structure is positioned on a piezo-electric x-y table under a Leica DM microscope. The orientation of the grating is determined using a HC PL Fluotar 100X objective from Leica. The setup used for the direct writing is shown in Fig. 2.12.

A mercury high pressure lamp is mounted in the microscope and used as light source. To obtain a small spot, a 8 μm diaphragm is imaged onto the substrate. The power of the

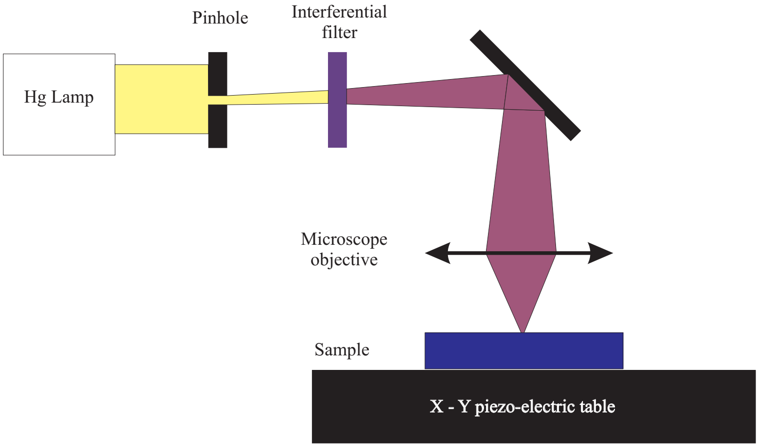

Figure 2.12: Scheme of a microscope used for lithography.

lamp is 100 W. Light is focused by a 100x objective with a numerical aperture of 0.90. The minimal spot size is given by the resolution of the objective to be $\delta = 1.22\ \lambda/\mathrm{NA}$. The photoresist is sensitive for wavelengths in the UV up to 450 nm. Thus, the minimal spot size that we can obtain using the full spectrum of the lamp is approximately 610 nm. In order to control the position and the displacement of the wafer when illuminating, the wafer is set on a piezo-electric table which allows lateral displacements up to 200 μm on the X and Y axis and a precision of 20 nm. The complete process flow to obtain a defect line in a two dimensional grating made of photoresist is described below:

1. Spin the photoresit.
2. Produce the two dimensional grating by interference photolithography.
3. Develop the photoresist.
4. Determine the grating orientation under the microscope.
5. Select the desired initial position.
6. Move the sample with the piezo-electric table while exposing through the pinhole.
7. develop the photoresist

The dose threshold to modify the photoresist properties depends on intensity and exposure time (dose). The width of the lines depends of the focalized spot size and the writing speed. We assume that the shape of the focal spot is Gaussian (see Fig. 2.13). Thus, when slowing down the writing speed, the dose gets larger and consequently, the surface where the photoresist exposure threshold increases. This is shown schematically in Fig. 2.13. This process also allows us to write defect points and two-dimensional structures.

To find a convenient starting point for defect writing we use the following method. Light with wavelengths outside the sensitive range of the resist is used for observation. We have chosen the yellow HG line at 582 nm. The positioning of the start point of a line

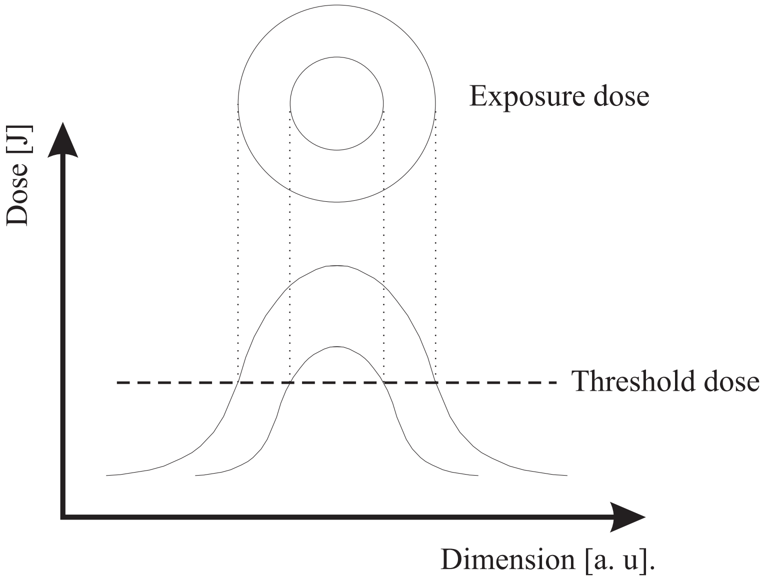

Figure 2.13: The defect width depends on the exposure dose and on the photoresist sensitivity (threshold).

or of a single defect point can be visualized relative to the regular grid structure of the pattern. Figure 2.14 shows an AFM measurement of a 800 nm periodic triangular lattice of pillars where three defect lines haves been written. The writing speeds are 2 μm/s, 1 μm/s and 0.5 μm/s leading to line width of 1 μm, 2 μm and 4 μm respectively.

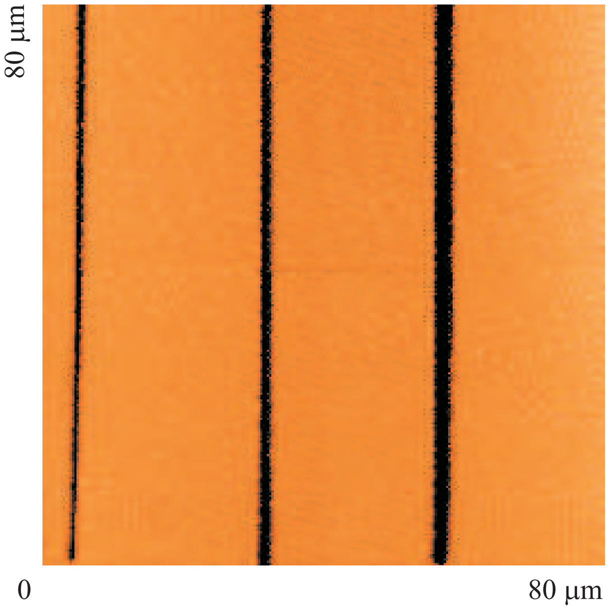

Figure 2.14: Defect lines written at different speeds (2, 1 and 0.5 μm/s) printed into a triangular periodic grating. The width of the line is 1, 2 and 4 μm respectively and depends on the speed of the substrate and shape of the spot.

Figure 2.15 shows a SEM picture of a 700 nm period triangular lattice on a glass wafer coated with 600 nm of amorphous silicon where two defect lines have been created and then, transferred into the silicon substrate by Reactive Ion Etching (see chap. 2.5.1 for details). The substrate speeds for the Fig. 2.15 a) and b) are 3 μm/s and 2 μm/s which create line widths of 0.7μm and 1μm respectively. The non-uniformity at the bottom of the lines is due to "the step by step" advance of the piezo-electric table which we use for the writing process. When the speed is higher than 2 μm/s, it is seen that the movement is not uniform anymore. This creates alternations of space where the photoresist is attacked down to the substrate and where it is not, after its development. This problem can be fixed by reducing the speed while decreasing the exposure intensity.

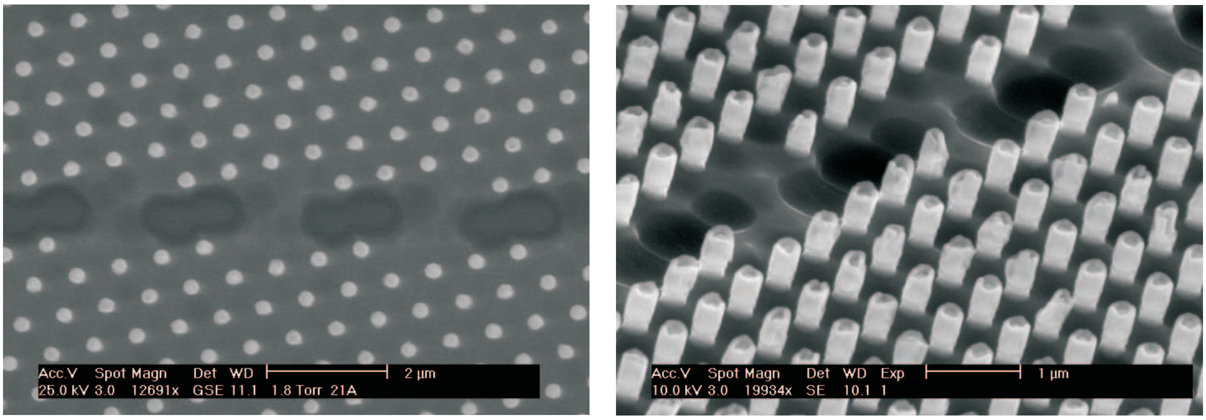

Figure 2.15: a) Top view of a SEM image of a transferred structure with a 600 nm defect line not aligned with the grating. b) A 60° view of a 1 μm defect line on the same wafer. The height of the pillars is 600 nm and the defect line is 700 nm due to a slight over etch in the glass. The height of the silicon coating is 600 nm.

Conclusion

We have described a process combining interferometry and direct writing to produce large area (> 1 mm^2) one- and two-dimensional periodic gratings with controlled defects or defect lines. The process needs two steps. First, printing interference fringes to obtain a two-dimensional grating of photoresist, thus focusing the light of an Hg lamp on the structures to write defect lines down to 600 nm width. After each steps, the photoresist is developed.

2.4.2 Selection of an area by micro-mask contact photolithography under microscope

In many devices with two dimensional structures, the shape of the lattice area needs to be precisely designed and waveguides must be created to connect optically the selected active area. Contact mask photolithography is a well known technique, adapted for this work. It suits particularly well with our interference photolithography technique. Nevertheless, the alignment between the mask and the subwavelength structure is not trivial. Indeed, The industrial mask contact machine cannot be used in our case due to the impossibility to have alignment marks and thus to obtain an angular matching between the mask and the grating direction. The positioning between the periodic lattice and the mask needs the use of a high magnification.

A micro-mask contact photolithography setup mounted on a Leica DM microscope stand using a HC PL Fluotar 100x objective from Leica has been developed specifically. It consists, as shown in Fig. 2.16 a), of a micro-mask holder with 4 degrees of freedom that are translations in x, y and z directions and rotation in the micro-mask plane. A schematic of the setup using a microscope is shown Fig. 2.16 b). The grating direction and the position of the area of interest is first referenced by imaging it with the 100x objective using a mercury lamp and a 582 nm interferential filter, then mechanically fixed. Then, the mask is mounted on the rotational stage to be matched angularly with the grating and the structured photoresist surface is put in contact with the micro-mask. The lithography exposure is performed through an objective whose magnification is chosen depending on the surface that has to be exposed. The mask is finally removed and the photoresist developed and post baked.

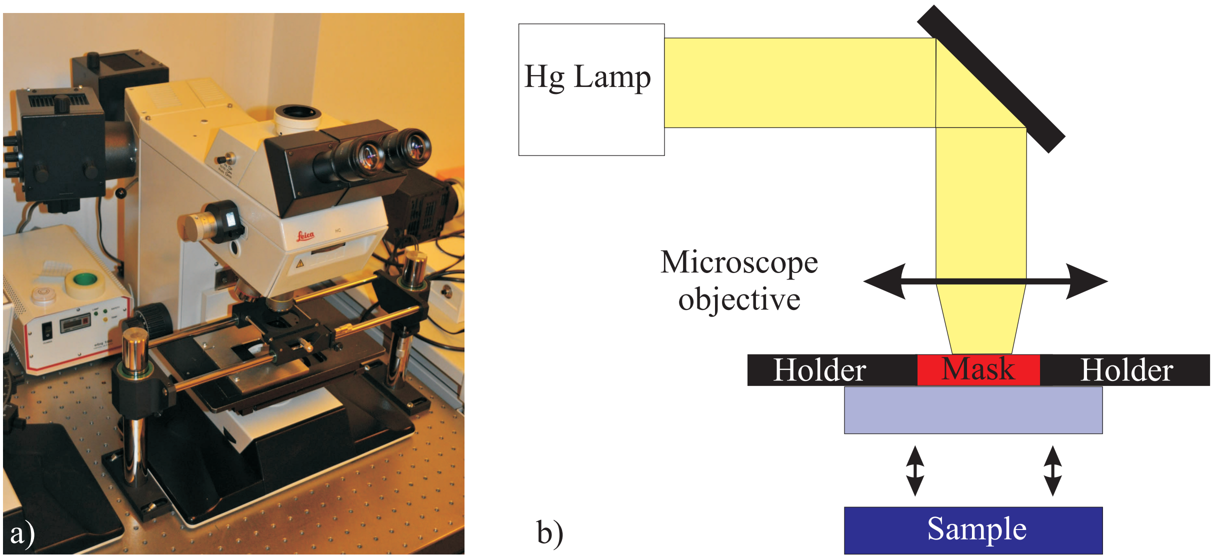

Figure 2.16: Picture and scheme of a contact mask setup mounted on a microscope that can be used to align the micro mask and sub micrometer gratings.

Typical exposure times are included between 0.5 and 3 seconds depending on the photoresist thickness. The SEM image (Fig. 2.17) shows the result of the process with a mask consisting of 10 μm lines and the interferential structure a triangular lattice of pillars. Other shape of mask can also be achieved as it will be shown in Chap. 2.5.2.

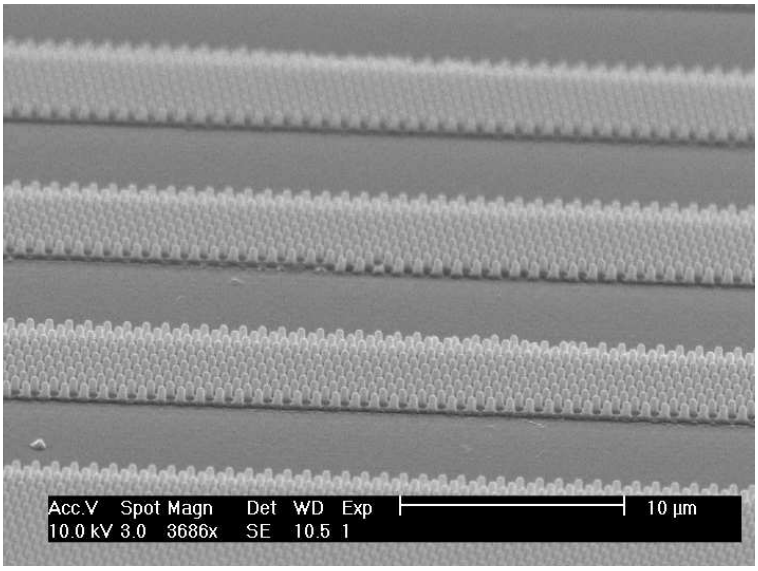

Figure 2.17: SEM image of a triangular periodic lattice of pillars where 10 μm lines have been selected using the micro-mask photolithography technique. One can observe a perfect matching between the grating and the lines direction.

2.5 Transfer of the structures into optical materials

The photoresist, Clariant AZ^R 1518, which we use in our lithography techniques, is not dedicated to be used in optical devices but only for intermediate fabrication steps. Thus, it is colored and degenerates progressively when aging. In the next section, we present the method used to transfer the structures into optical materials such as quartz and silicon.

2.5.1 Transfer into silicon or quartz by Reactive Ion Etching

To transfer micro and nanostructures into quartz and silicon, we use an Inductively Coupled Plasma (ICP) source for the Reactive Ion Etching (RIE) from Surface Technology System (STS) company.

The wafer is placed inside a vacuum chamber in which one or several gases are introduced with a specified flow and a specified pressure. Plasma is initiated in the reactor by using an RF (radio frequency) power source. The created ionic bombardment can physically etch some material by transferring some of their kinetic energy. The ionic bombardment is anisotropic (vertical profile) and non-selective. An isotropic etching also occurs due to chemical reactions with the etchant gas. In our case, the etchant gases are SF_6 and C_3F_8 to etch silicon and quartz, respectively. Typical parameters to etch sub-micron periodic gratings made of photoresist into silicon and quartz are shown in the Table 2.3.

	Etchant gas		Power		Pressure	Photoresist etching rate	Substrate etching rate
	SF_6	C_3F_8	Coil	Platen			
Silicon	20 sccm		600 W	200 W	5 mTorr	10 nm/s	20 nm/s
Quartz		30 sccm	600 W	200 W	2.7 mTorr	6.2 nm/s	5 nm/s

Table 2.3: Table showing typical parameters used to etch silicon and quartz by RIE.

O_2 Plasma can be used to etch selectively the photoresist. Argon (Ar) and methane (CH_4) are also available in our machine and can be used to improve the surface state and selectivity. More details on RIE can be found in [58].

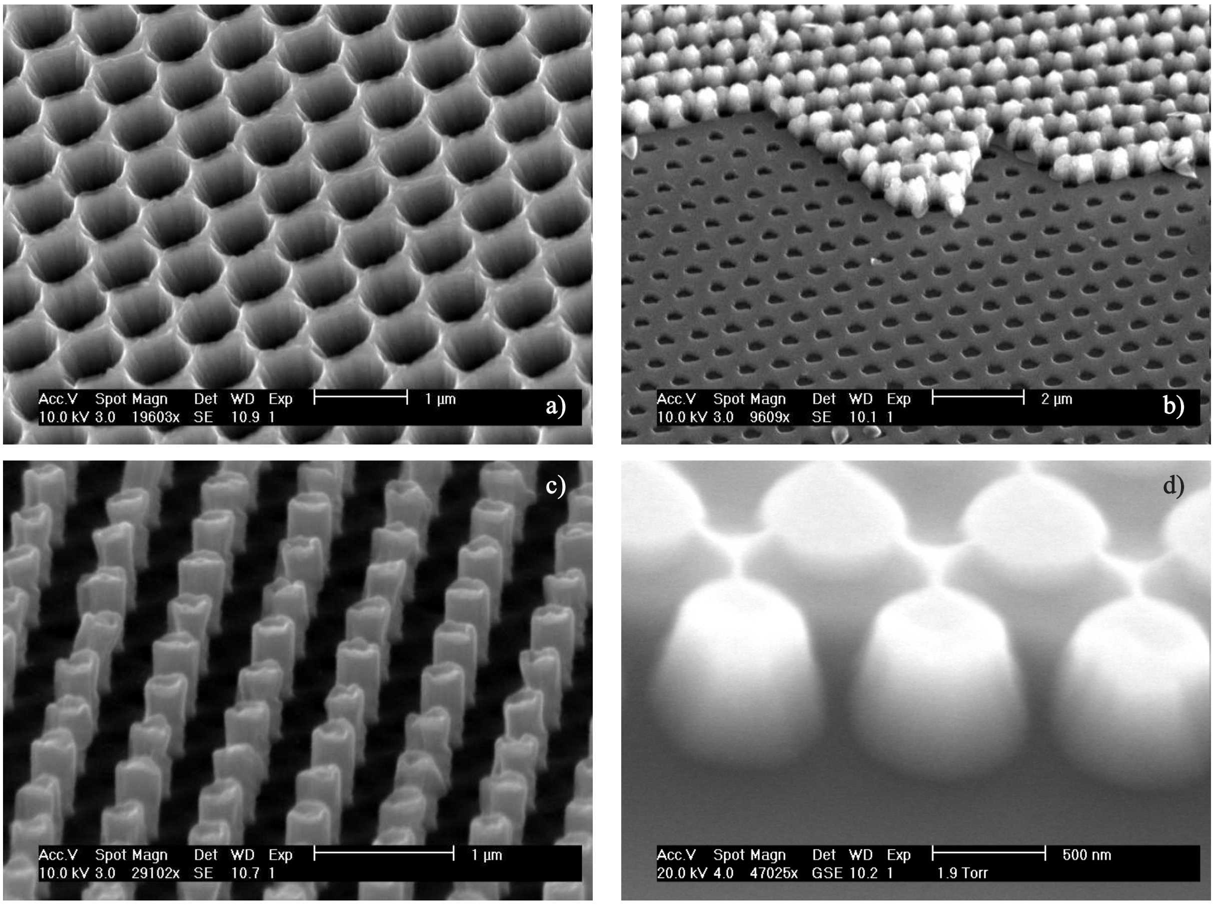

Figure 2.18: SEM pictures of sub-micron periodic structures transferred into a 700 nm coating of amorphous silicon grown on a glass wafer.

The SEM pictures in Fig. 2.18 show some examples of transferred structures on a 700 nm coating of amorphous silicon grown by Plasma Enhanced Chemical Vapor Deposition on a 4 inch glass wafer. All the structures are 700 nm high. Figure 2.18 a) shows a 800 nm periodic triangular lattice of holes, Fig. 2.18 b) shows a 800 nm periodic triangular lattice of holes where one can still see some unremoved photoresist on the upper part of the image. Figure 2.18 c) shows a 700 nm periodic lattice of pillars and Fig. 2.18 d) shows a 700 nm periodic lattice of pillars with a bridge between the pillars. The variation of holes and pillars sizes that we can observe on those images is the consequence of the different parameters used for the interference photolithography process.

Figure 2.19 shows a 100 nm high nanostructure with a periodicity of 270 nm that have been transferred into quartz using the parameters of Table 2.3. This specific structure will be discussed in more detail in Chap. 3.

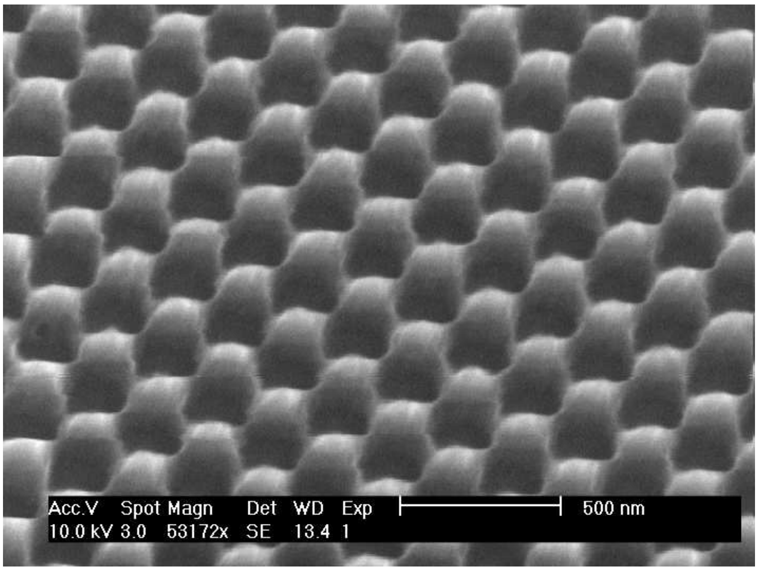

Figure 2.19: SEM picture of 270 nm periodic square lattice of 100 nm high pillars transferred into quartz by RIE

2.5.2 Superprism device

A structure, designed to exhibit high dispersion of light, known as superprism has been fabricated using interference lithography (Chap. 2.3.2) and our contact mask lithography setup (Chap. 2.4.2) to shape the photonic crystal area and to built waveguides in SU8 (a negative photoresist with a refractive index in the infrared of 1.57). The parameters of the structures were chosen according to theoretical simulations. One can find examples in Chap. 4.

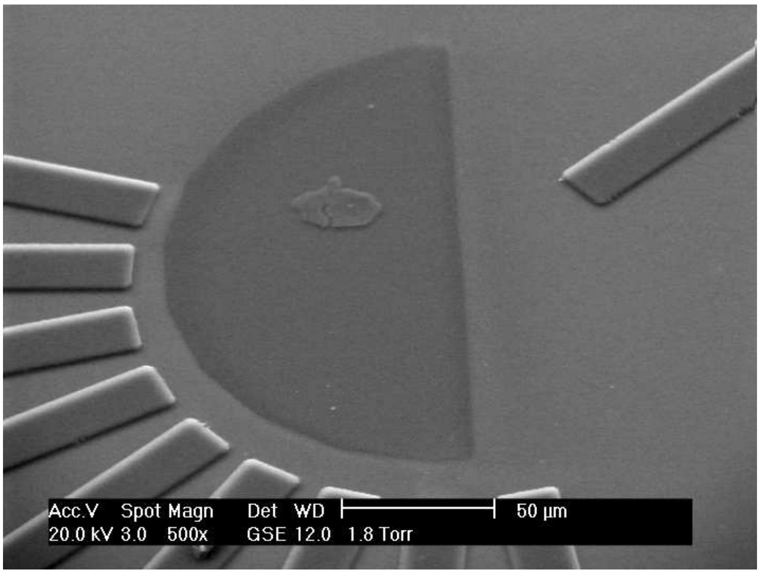

Figure 2.20: SEM picture of a half circle photonic crystal with an input SU8 waveguide on the right and several output SU8 waveguides on the left.

The final structure obtained, shown in Fig. 2.20 was fabricated with the following four steps on a glass wafer coated with 700 nm of amorphous silicon:

1. Interference lithography to produce a 800 nm triangular periodic lattice.
2. Contact mask lithography under microscope to select the half circle.
3. Transferring the structure into the silicon by RIE.
4. Coating the wafer with SU8 followed by a contact mask lithography under microscope to fabricate input and output waveguide made of SU8.

Non-optimized mask design and, most of all, the intrinsic limitation of our interference photolithography technique to obtain vertical pillars and to control accurately the ratio between the period and the pillar's diameter lead to a high difficulty to produce photonic crystals that can be measured. A better control of the limiting parameter must be obtained to fabricate such a sensitive structure like superprism devices. Those main parameters are :

1. Temperature and humidity stability in the clean room.
2. Exposure intensity reproductibility for the interference photolithography. (We still have an accuracy of ± 5% onto the substrate surface).
3. The transfer into silicon by RIE should be done in a system dedicated to only one type of etched material.

2.5.3 The standing wave effect

In this section, we will present an interesting particularity of our interference photolithography process produced by a standing wave parallel to the surface that is created during the interference photolithography by the back reflection of the exposure beam onto the substrate surface. This phenomenon has been shown years ago [59–62] and theoretically studied and named Aztec structures [52]. Similar structure exhibiting impressive color effects can be found in nature. Wings of a few butterflies, beetles elytra or peacock's feather are well known examples [63].

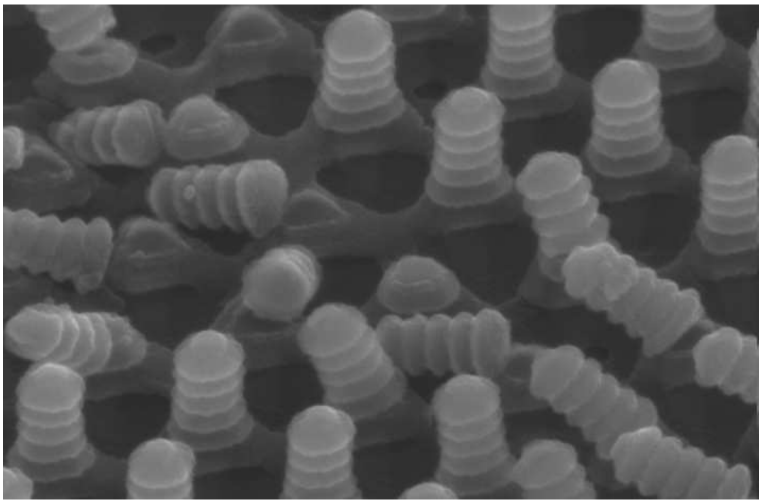

Figure 2.21: SEM picture of *Xmas tree* like shape pillars of photoresist

Figure 2.21 shows such a structure fabricated with our interference photolithography technique. In this case, we can recognize a triangular lattice of pillars produced by three exposures to interference pattern while rotating the sample by 60° degrees. Note that some pillars fell down probably due to a mechanical shock. We can see that each pillar has its own periodic vertical modulation which is due to interference wavefronts created by reflection of the substrate and the exposure beam. The period of the modulation δ depends on the illumination angle inside the photoresist (Bragg condition) Eq. (2.5).

$$\delta = \frac{\lambda_{Pr}}{2\cos(\frac{\alpha}{2})} \tag{2.5}$$

Where α is the angle between the input beam and its reflection from the substrate. Using Snell's law Eq. (2.6), the alteration of the wavelength passing through a media in Eq. (2.7) (chap. 2.2 of [57]) and the grating equation Eq. (2.3), we can establish a relation linking the period of the lattice (Λ), the wavelength (λ) and the period of the pillars modulation (δ) as shown in Eq. (2.8).

$$n_{air}\sin(\frac{\theta}{2}) = n_{Pr}\sin(\frac{\alpha}{2}) \tag{2.6}$$

$$\lambda_{Pr} = \frac{\lambda}{n_{Pr}} \tag{2.7}$$

$$\delta = \frac{1}{2}\frac{\Lambda\sin(\theta)}{\sqrt{n_{Pr}^2 - sin^2(\frac{\theta}{2})}} \tag{2.8}$$

For the fabricated structures, the modulation produced by the standing wave is an artifact that we want to minimize. Indeed, our photonic structures have to be transferred by RIE into silicon as shown in Chap. 2.5.2 or quartz as in Chap. 3. Therefore, this modulation has to be avoided to obtain shapes of the nanostructures as good as possible. An overview of the different strategies proposed can be found in Table 2.4 and further discussed in the following paragraphs. Note that when the substrate is not transparent to the exposure wavelength (413 nm), the reflected beam reflects from the photoresist - substrate interface, whereas it reflects mostly from the backside when the substrate is transparent.

Strategy	Quartz or glass	Silicon
Thick photoresist layer	Possible	Possible
Antireflection photoresist coating	Possible	Possible
Backside dark absorber	Possible	Not possible
Index matching oil	Possible	Not possible

Table 2.4: Overview of the strategies that we propose to minimize the standing wave.

Other strategies could also be envisaged. We mention here only two more, as they are very simple. The first consists of post baking the photoresist between the exposure and the development steps [64]. The high temperatures used (100°C to 130°C) cause diffusion of the photoactive compound, thus smoothing out the standing wave modulation. The second, limited to specific applications and quite expensive, consists of using a black glass substrate [65].

Silicon substrate

For the silicon substrate, the reflectivity on the wafer surface is almost 30 %. Thus, strategies to attenuate the reflected light on this surface need to be applied. The SEM picture, Fig. 2.22 a), shows a side view (parallel to the substrate) of a 800 nm triangular periodic lattice of pillars that are 700 nm high. This height corresponds to the initial thickness of photoresist deposited on the silicon wafer. It is important to obtain structures that go through the complete photoresist when those structures should serve as a mask and have to be transferred by etching into the substrate. When the structures must not be transferred, a thicker photoresist coating can be spun to absorb the light and avoiding the reflection. Figure 2.22 b) shows a pattern exposed with the same parameters than previously on a 1.5 μm photoresist coating. One can observe that no patterning parallel to the substrate has been created. The height of the pillars is, this time, 500 nm. This decrease is due to the decrease of the total exposure dose experienced by the photoresist as there is less light reflected back from the substrate surface.

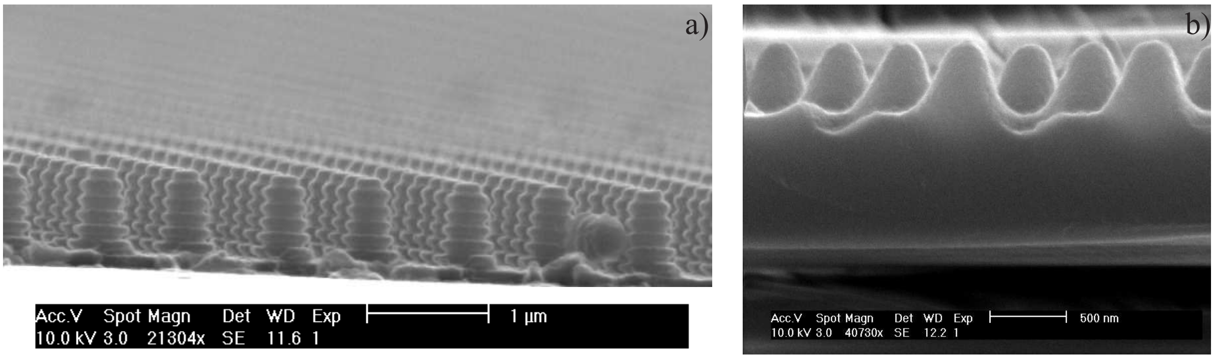

Figure 2.22: SEM pictures of gratings made into 700 nm (a) and 1.5 μm (b) thick photoresist coatings on silicon.

To attenuate the reflection without coating a too thick photoresist layer, a 100 nm antireflective coating of ARC^R XLT positive photoresist from *Brewer Science, Inc.* is spun onto the silicon wafer. The standard proceeding is 100°C for 20 seconds and 190°C for 50 seconds on a hot plate. The layer is sandwiched between the substrate and the usual photoresist AZ^R 1518. The ultra-violet photo-sensitivity of both layers are comparable. The exposure parameters have been slightly increased to compensate the attenuation of the back reflection. The reflectance ($\Re$) of the photoresist - silicon interface, at normal incidence, without the antireflective coating can be calculated with the aid of Eq. (2.9). Using n_{Pr} = 1.7 and n_{Si} =5.39 at 400 nm, we get $\Re$ = 27 %. The data sheet for the ARC^R XLT photoresist coating give a reflectance of $\Re$ = 2 %.

$$\Re = (\frac{n_{Pr} - n_{Si}}{n_{Pr} + n_{Si}})^2 \tag{2.9}$$

Figure 2.23 shows structures obtained by this technique where the modulation, although still visible, are strongly suppressed compared to the one shown in Fig. 2.22 a).

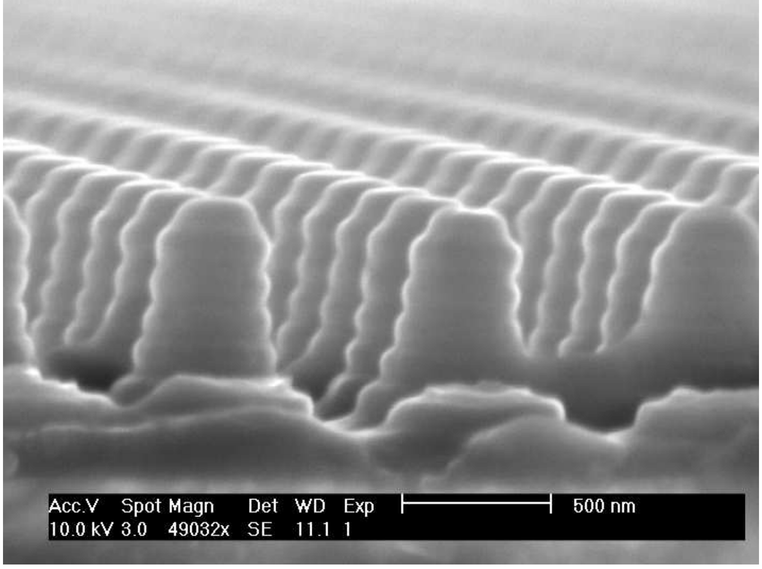

Figure 2.23: SEM picture of a 800 nm periodic triangular lattice of pillars in photoresist using an antireflective coating layer.

Glass and quartz substrates

For quartz and glass substrates the same modulation appears but with a smaller amplitude, as shown in Fig. 2.24 a) and b) for a triangular lattice of pillars with a period of 800 nm and a height of 600 nm (with some bridges remaining between the pillars) and a structure made of holes, respectively, with the same parameters.

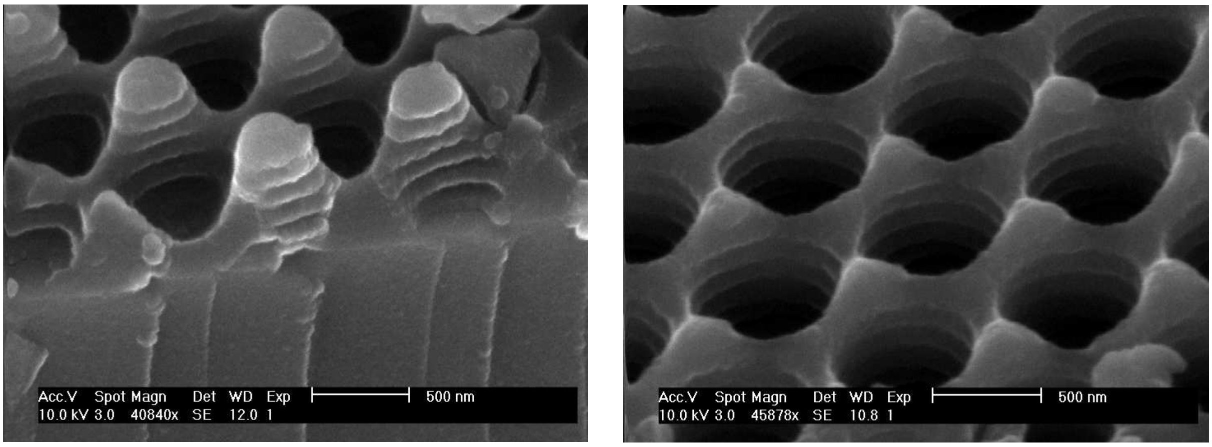

Figure 2.24: SEM pictures of structures of pillars a) and holes b) made of a 600 nm thick coating of photoresist on a glass wafer without antireflective techniques.

On these substrates, the reflection producing the modulation comes from the second interface (glass - air) of the wafer. The first interface (photoresist - glass) can be neglected due to the relative good matching between the refractive index of glass ($n_{glass} = 1.52$) and photoresist ($n_{Pr} = 1.7$) which leads to a reflectance $\Re = 0.3$ %. The reflectance at the second interface is $\Re = 4\ \%$. This, rather, small value explains why the modulation is weaker than with a silicon substrate. Figure 2.25 shows a SEM picture of three techniques detailed below that can be used to attenuate the back reflection.

- **(I) Antireflective photoresist coating**: One can observe that, using the antireflective coating as describe above, the modulation is almost fully suppressed. The drawback is that the ARC^R XLT photoresist has not been developed at the same rate than the Clariant AZ^R 1518 and is still visible at the bottom of the pillars.
- **(II) Backside dark absorber**: By spraying a dark absorbing paint on the back side of the wafer, the reflection at its interface is strongly attenuated. The drawback is here that some processes will be disturbed or even impossible to be realized due to the paint such as the use of acetone, high temperature process or holding the sample with vacuum pumping.
- **(III) Index matching oil**: This technique consists of a deposition of index matching oil between the wafer and the substrate holder which is used as a light absorber. The drawback here is that the oil has then to be removed with isopropanol or acetone, which is not trivial without damaging the photoresist.

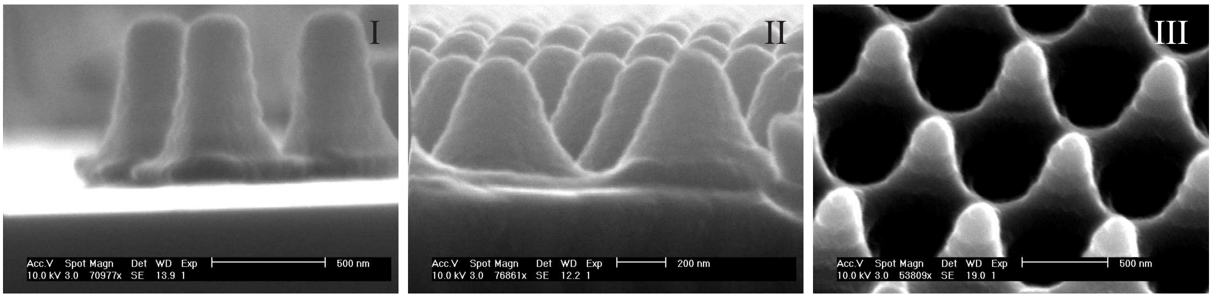

Figure 2.25: SEM images of photoresist pillars fabricated with interference photolithography. Three different techniques have been used to suppressed the vertical modulation: (I) Antireflective photoresist coating, (II) Backside dark absorber, (III) Index matching oil.

To conclude, depending on specific needs, one can choose between these techniques to obtain the desired structures.

2.6 Conclusion

We have presented, in this chapter, an interference photolithography technique usable to pattern one- and two-dimensional periodic gratings on large area. We have demonstrated practically how to introduce defects in the grating by focusing the light of a mercury lamp with a microscope. A micro-mask setup has been realized in order to define the specific surface shape of photonic devices and to fabricate waveguides. The combination between those techniques is a crucial point. They are all based on the same photoresist technology which decreases the number of steps required to fabricate complex devices as shown for the superprism. All substrate shapes and sizes can be equally used and we have shown how to overcome the standing wave artifacts for different materials. The transfer of the nanostructures have been performed by RIE into silicon and quartz. All these technologies allow the fabrication of optical micro and nano devices quickly, inexpensively and on large scale in comparison with the same structures fabricated by a standard E-beam photolithography process. The price to pay, is the impossibility to tune, on the same grating, the periodicity and a non negligible difficulty to obtain structures with sharp angle rather than rounded. A better stability of parameters such as the cleanroom humidity and temperature, homogeneity of the exposure dose and etching with the RIE should allow to produce photonic structures with a sufficient accuracy.

The main strengths of interference lithography technique are the small feature size ($< \lambda/4$) that can be fabricated, the large surface that can be produced at a time at relatively low cost and its ability to produce structures on non-flat surfaces. With standard mask contact lithography the minimum feature size is comparable to the wavelength used for the exposure ($\approx \lambda$). Using a deep-UV stepper (the mask is imaged and reduced by a lens onto the substrate), the minimum feature size (σ) is describe by $\sigma = \mathrm{k}\lambda \ / \ \mathrm{NA}$, (where k is a coefficient expressing process-related factors, λ is the wavelength of the light, and NA is the numerical aperture). This leads approximately to a $\sim \lambda/4$ resolution for very advanced (and expensive) systems. A roadmap for optical lithography is shown in [66]. An intrinsic property of the interference lithography is to produce a pattern in the volume. This allows the fabrication of periodic gratings on non-flat surface such as microlenses, as shown in the next chapter.

Chapter 3

Antireflective nanostructures on microlenses

3.1 Introduction

The fabrication of microlens arrays has been extensively explored [67–69] as they are widely used in a large range of applications, often to link between macro and micro optical components [70]. Antireflective (AR) coatings and surface treatments on microlenses have been proposed for different materials and wavelengths [71–73] and theoretical analysis have been performed [74]. The principal solution proposed in a number of papers consists of an antireflective coating (thin film) deposited on the structure. Although this method is quite evolved, there are some applications where having a monolithic material structure is advantageous, such as under extreme temperature conditions or particularly aggressive environments, as presented in [75] for planar surfaces.

An alternative approach to thin film coatings are structures having engineered effective index properties. Such nanostructures reduce the reflectivity and enhance the light transmission through lenses. The principle of an AR nanostructured surface is analogous to an AR thin film (Fig. 3.1 where the nanostructure acts as a coating with an effective index of refraction (n_{eff}).

$$\epsilon_{eff}^{TE} = F\epsilon_{air} + (1-F)\epsilon_{quartz} \tag{3.1}$$

$$\epsilon_{eff}^{TM} = \frac{1}{\frac{F}{\epsilon_{air}} + \frac{1-F}{\epsilon_{quartz}}} \tag{3.2}$$

The permittivity (ϵ) and the permeability (μ) are the material constants that define the refractive index n = $\sqrt{\epsilon\mu}$. For a grating, the permittivity varies following Eq. (3.1) and Eq. (3.2) for different polarization of light, where F is the fill factor of the grating. The permeability stays close to 1. By this technique, refractiveindices can be realized that do not exist in nature.

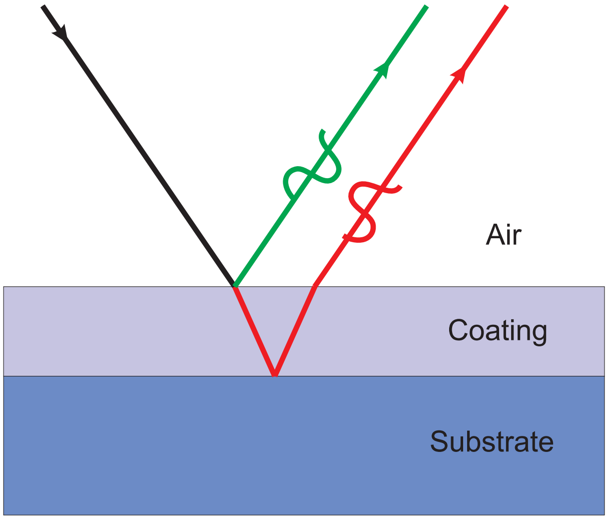

Figure 3.1: Principle of an antireflective thin coating.

For AR coatings, the optimum is obtained when the light reflected at the air - coating interface has the same amplitude than the light reflected at the coating - substrate interface but in phase opposition. The first criterion is obtained equalling the power reflectance (Eq. (3.3)) at the two interfaces which is obtained for $n_c = \sqrt{n_s}$, where n_c and n_s are the refractive indices of the coating and substrate, respectively.

$$\Re = (\frac{n_2 - n_1}{n_2 + n_1})^2 \tag{3.3}$$

The phase opposition of the two reflected beams is obtained if the optical path inside the coating (2 × n_c × coating thickness) is equal to half the wavelength (at normal incidence). Thus, if, for instance, the coating thickness is thinner than targeted, the optimized antireflective effect occurs for shorter wavelength.

In this work we demonstrate the feasibility of fabricating such nanostructures on a large, non-flat surface. Note that one-dimensional larger grating produced by interference lithography and hot embossing replication has been demonstrated [76] for plastic microlenses. In the following, we will present experimental results on such nanostructured monolithic (quartz) lenses, which, although not ideal, exhibit significant AR characteristics.

3.2 Fabrication

We describe here the fabrication of a subwavelength AR layer on the surface of a quartz microlens array with interference photolithography and plasma etching. The challenge is to obtain an homogenous structure on the entire surface of each lens and on a large array of microlenses. The shape of the nanostructures we produce with this method is not as rectangular as the structures often studied. However, these more rounded, non-rectangular nanostructures still possess significant AR properties. Moreover, it allows the production of nanostructures quickly, inexpensively and on large areas.

First, an hexagonal array of 145 μm diameter microlenses is produced by photolithography and a reflow process [77] on a 4 inch quartz wafer. Then, the microlenses, which are 14 μm high, are transferred into the quartz by RIE. The first line of the Table 3.1 shows the used parameters.

	Gases			Photoresist etching rate	Quartz etching rate
	C_3F_8	O_2	Argon		
Microlenses	34 sccm	20 sccm	3 sccm	5 nm/s	5 nm/s
Nanostructures	30 sccm		1 sccm	6.6 nm/s	3.3 nm/s

Table 3.1: Table showing the parameters used to etch microlenses and nanostructures onto quartz wafer. Sccm stands for *standard cubic centimeter per minutes.* Note that the pressure is set at 2.7 mTorr, the coil power at 600 W and the platen power at 200 W.

For the AR nanostructured surface, a 400 nm diluted photoresist (0.5 : 1) is spun at 400 rpm for 25 seconds, in order to cover fully the surface of the microlenses. The Scanning Electron Microscope (SEM) picture (Fig. 3.2) presents a side view of a microlens coated by the photoresist already structured. One can see that due to the slope induced by the microlens curvature, the height of the photoresist coating is not uniform over the entire surface [78]. Indeed, the photoresist thickness varies between the lower (~1 μm) and the upper (~450 nm) parts of the microlenses with a minimum around 200 nm where the slope is greatest. This requires that the exposure parameters for the photolithography be set for the thinnest part of the resist in order to avoid overexposure.

A 270 nm periodic square lattice of pillars is recorded using interference photolithography as explained in Chap. 2 and transferred into the quartz by RIE with the parameters presented in Table 3.1. The shape of the microlenses is only minimally affected, as shown below, thanks to the small thickness that has to be etched by this step. After removing the photoresist, we obtain a 4 inch wafer covered with microlenses having a nanostructured AR surface in quartz.

Fig. 3.3 shows SEM pictures of a nanostructured microlens [Fig. 3.3 a)] and close-up views of the shape of the nanostructures on different areas of the lens [Fig. 3.3 b), c) and d)].

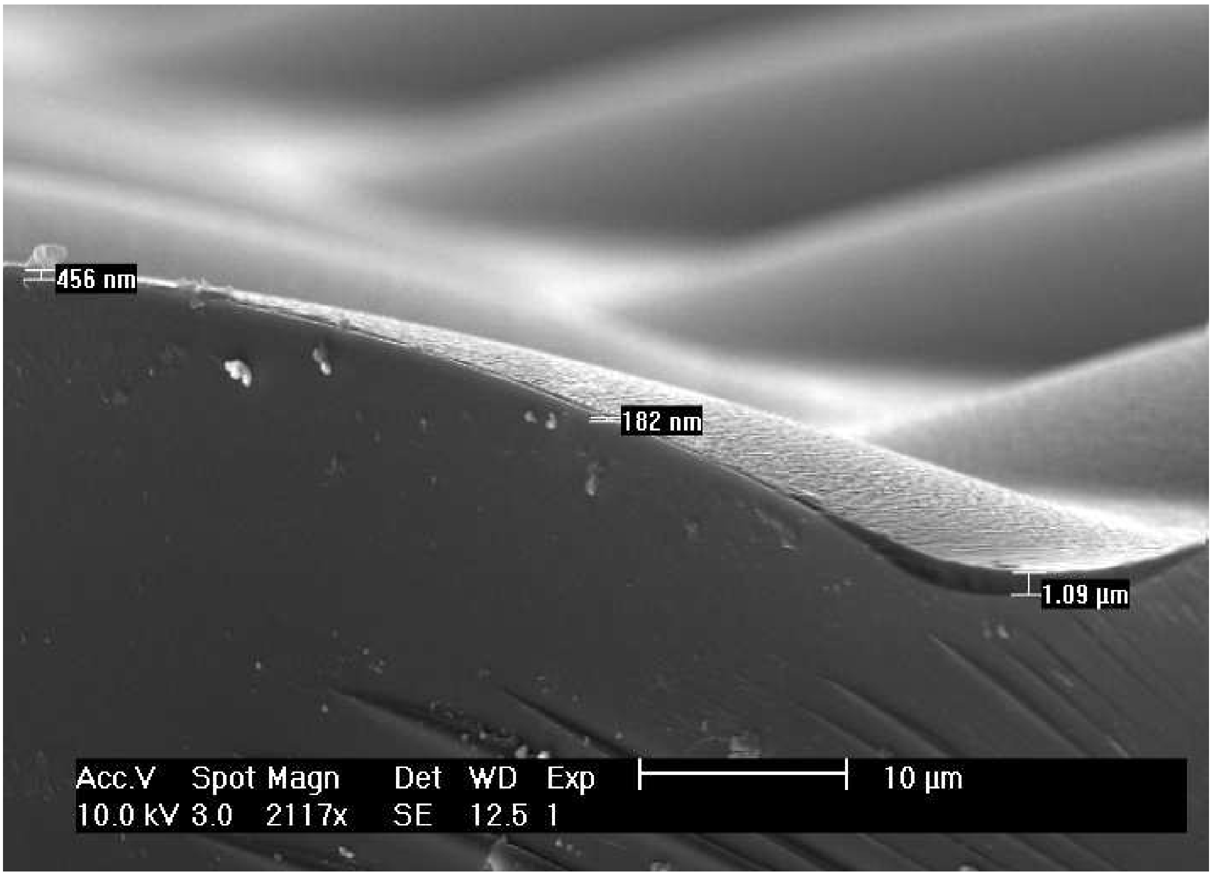

Figure 3.2: Side view of a microlens with nanostructured photoresist shows that photoresist covers the entire surface of the microlenses, with varying thickness depending on the position and on the local slope.

The annular rings (Moiré effect) observed in the SEM picture in Fig. 3.3 a) show that the nanostructures completely cover the two-dimensional surface consisting of microlenses. The periodicity is 270 nm in both directions, independent of the position on the lens. The nanostructures in the central region of the lens [Fig. 3.3 b)] are approximately 100 nm deep, and have a slightly rounded shape as compared to the rectangle structures studied theoretically [71]. In addition, one can observe some bridges between the pillars. In the maximum slope region [Fig. 3.3 c)], we can see that the bridges between the pillars have disappeared, and the structures are approximately 40 nm deep. In the external part of the lens [Fig. 3.3 d)], the shape of the nanostructures have the same aspect as in the central region [Fig. 3.3 b)]. The variations in the aspect ratio of the nanostructures are due to the inhomogeneity of the PR thickness as shown Fig. 3.2.

Note that the non-rectangular nanostructure profile does not, a priori, impact the desired properties of our device, as our goal is not to obtain a wavelength filter but rather a broadband AR effect. An optimization of the PR deposition process shall be envisaged to improve the homogeneity. Nevertheless, as we will demonstrate, these nanostructures result in a significant reduction in the reflectivity of the microlens surface.

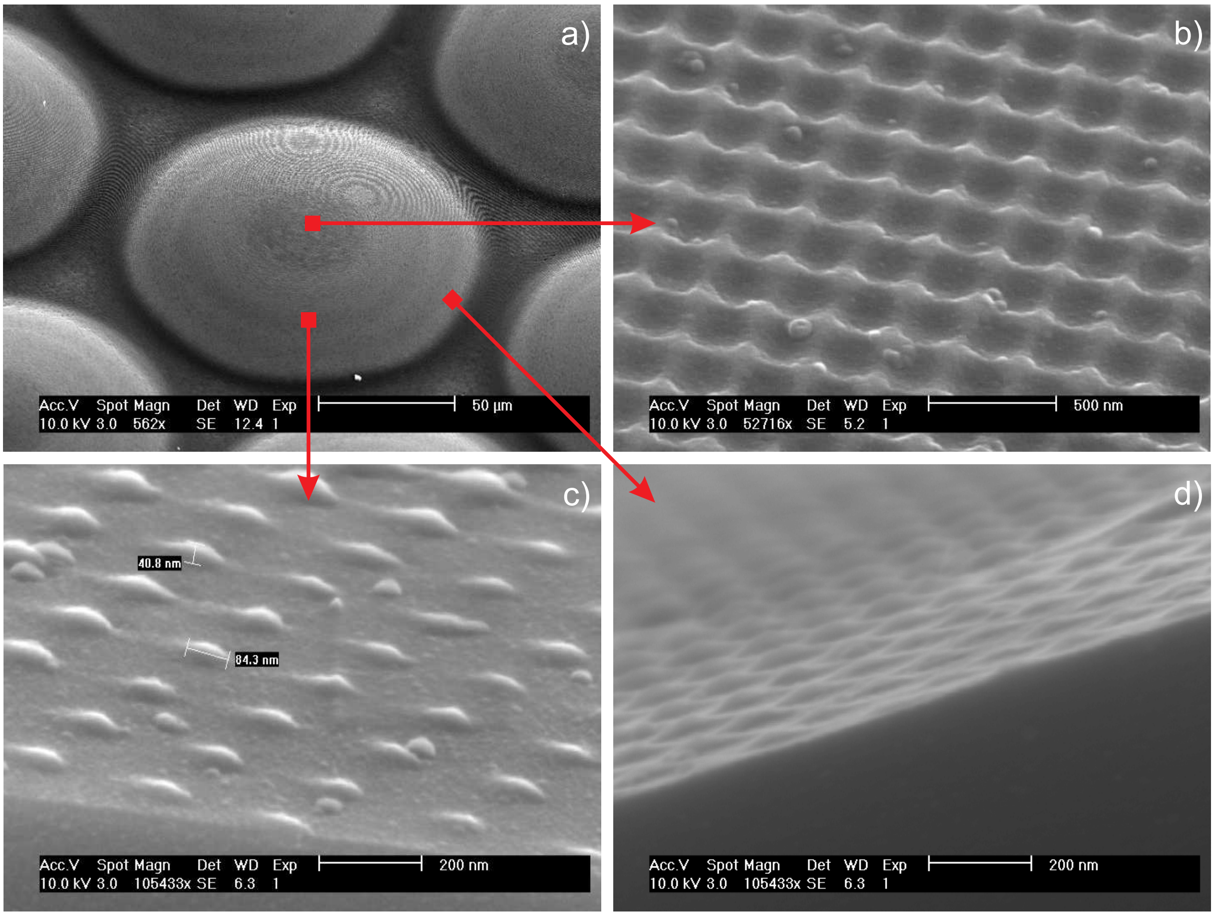

Figure 3.3: : a) SEM picture of a 145 μm diameter microlens with the entire surface covered by a square array of nanopillars. SEM pictures with higher magnification of different parts of the microlens: b) top region, c) maximum slope region, and d) edge region.

The quality of the microlenses is measured using a Mach-Zehnder interferometric microscope, using an iris to select a single lens [79]. The phase and intensity of the interference pattern are measured, then the Strehl ratio of the lenses is calculated. The Strehl ratio is the ratio between the peak diffraction intensities of an aberrated versus a perfect wavefront. Conventionally, the acceptable value for the Strehl ratio is greater than 0.8, which corresponds to an rms wavefront error of $\lambda/14$ (Marechal criterion [80]). For the quartz microlenses without nanostructure, we obtain Strehl ratios between 0.92 and 0.99 depending on the specific lens selected. After the plasma etching, due to the PR thickness variation, the shape of the microlenses changes slightly and the Strehl ratio is measured to be around 0.9. The measurements are done on different areas of two wafers of each type. From the phase image Fig. 3.4, we observe that the aberrations come mostly from the outer part of the lens.

From these measurements, we demonstrate the feasibility of producing a nanostructured AR metamaterial on a quartz microlens array without significantly reducing the

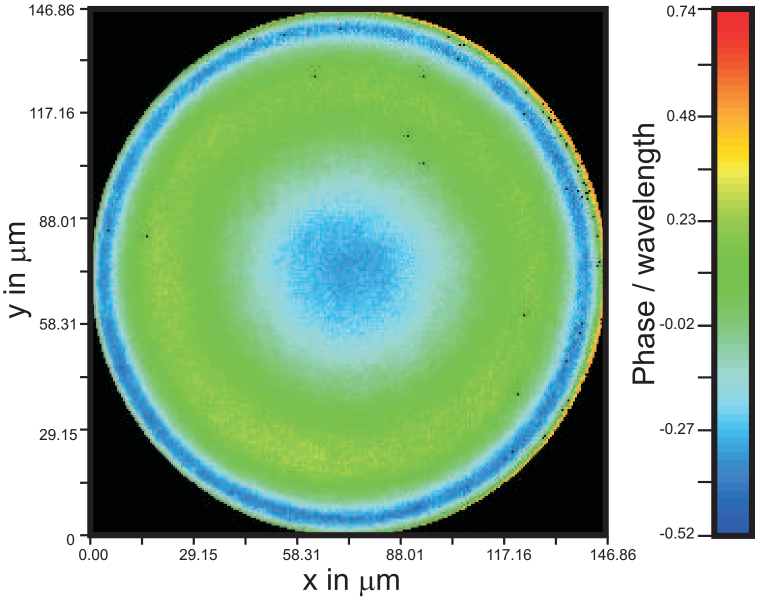

Figure 3.4: Measured phase image of a nanostructured microlens using an interference microscope, working at 632 nm wavelength, to characterize the Strehl ratio.

quality of the lenses. Indeed, the challenge here is to fabricate a combination of micro- and nano-scale structures on a large surface in the same material.

3.3 Characterization in reflection

In the previous section, we demonstrated the fabrication of a microlens array with its entire surface covered by a nanostructured AR square grating. However, the fabricated nanostructures were non-ideal in several respects, including variability in the nanostructure size depending on the position on the lens, and deviation of the pillar shape from the rectangular profile of the original design [71]. In this section, we will show through experimental characterization that these non-ideal nanostructures still provide a significant attenuation of the reflectivity of the microlens array.

The setup used for the reflection measurements is shown schematically in Fig. 3.5. It is based on a standard microscope stand (Leica DMR) with a spectrometer (Ocean Optics 2000) mounted at the end of the light path. Three objectives have been used: 100X (NA = 0.9), 40X (NA = 0.6) and 20X (NA = 0.4). An adjustable circular diaphragm is added in the path light to be imaged onto the sample. It allows control of the active area to be measured. This setup will be used for all reflection measurements of our samples.

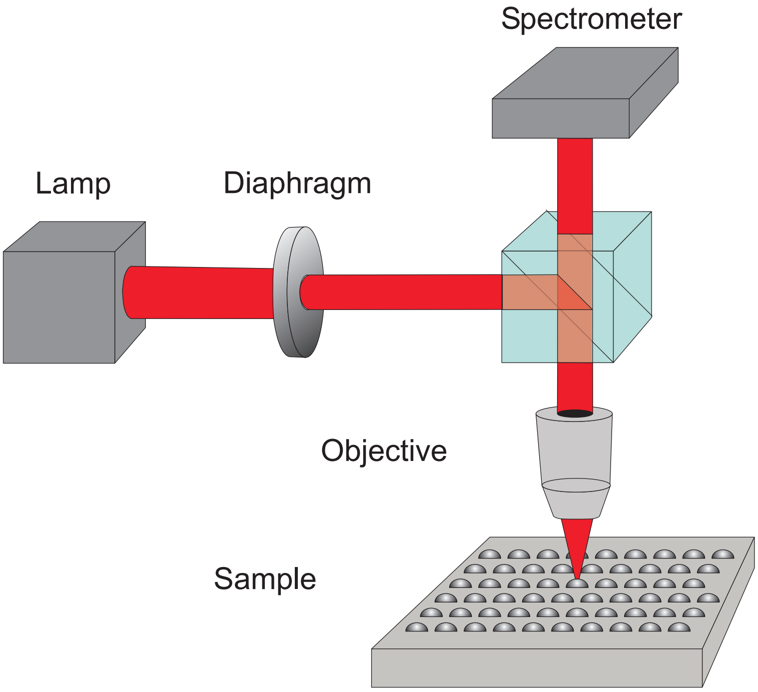

Figure 3.5: Schematic drawing of the setup for reflectivity measurements of different samples. The light from a halogen lamp is focused onto the sample and the reflected light is then collected to be analyzed by a spectrometer.

The first step is to characterize the performance of the nanostructured AR surface on a flat substrate. A flat quartz wafer without nanostructures is measured to obtain a reference signal (R_{ref}) with the image of the diaphragm is set at 140 μm diameter. Then, the reflection of the nanostructured sample is measured (R) with the same parameters of illumination and detection. The graph (Fig. 3.6) shows the ratio between the spectral response of the nanostructured surface and the reference signal. The red curve is the result using a 100X objective with a numerical aperture of 0.9 and the black curve using a 40X objective with a numerical aperture of 0.6. The reflectivity is decreased between 10 % and 35 % with the 100X objective and between 5 % and 10 % with the 40X objective. This means that the nanostructure layer has an antireflective effect over the entire visible wavelength range, as was predicted theoretically and already demonstrated experimentally in [71] where the AR layer consists of a nanostructured coating of photoresist. Furthermore, using a higher numerical aperture (i.e. a larger illumination angle) reduces the reflectivity, which qualitatively agrees with the theoretical predictions presented in Table 2 of Ref. [74]. The reflectivity varies as a function of the wavelength, as demonstrated in [81]. In the results shown in Fig. 3.6, the largest attenuation is obtained for smaller wavelengths. Theoretically, the minimum of reflection should be centered around 550 nm. However, since the height of the nanopillars is lower than in the design, it is to be expected that this minimum is shifted to lower wavelengths.

Moreover, measurements are made on different areas of the sample with essentially

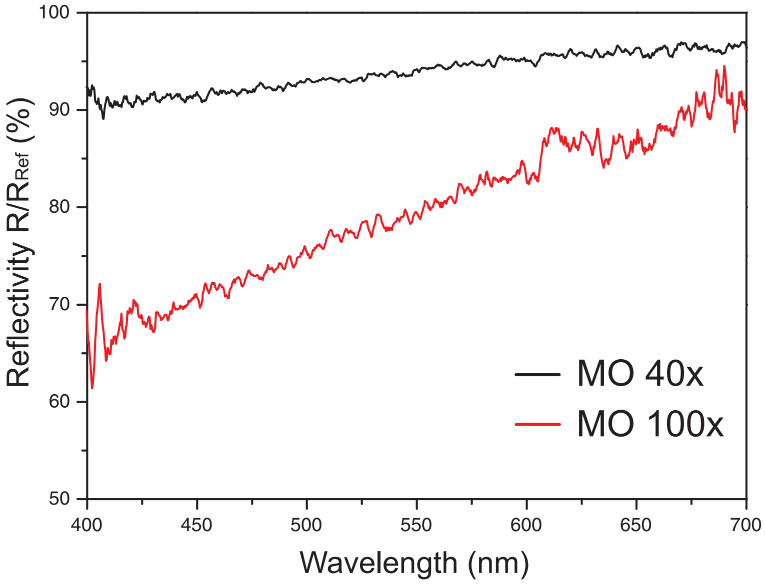

Figure 3.6: Reflectivity spectra of the AR nanostructures on a flat substrate normalized by the reflectivity of a flat non-structured wafer, using a 100X objective, NA = 0.9 (red curve) and a 40X objective, NA = 0.6 (black curve).

identical results (less than 5 % variation). This shows that the nanostructures are relatively homogenous over the entire 4 inch wafer.

From these results, we have demonstrated that we are able to fabricate a square lattice of nanopillars with a periodicity of 270 nm on a 4-inch wafer. A non-negligible attenuation of the reflectivity has been observed and could be improved by producing taller nanostructures.

The objective is then to determine whether the nanostructures maintain the same AR behavior on a microlens array instead of on a flat surface. The setup shown in Fig. 3.5 is used to characterize these samples. In this case the reference is defined by measuring the reflectivity of an array of quartz microlenses without AR nanostructures. All the results are normalized by this reference.

Two different studies have been performed. The first consists of the measurement of the reflectivity of a surface containing several nanostructured microlenses (~7). In this case, a 20X objective with a numerical aperture of 0.4 is needed to image a large enough area (450 μm diameter). For both the sample and the reference, the center of one microlens is positioned in the middle of the light path. The results are shown in Fig. 3.7.

The attenuation of the reflectivity is between 30 % and 15 % over the visible spectrum. The curve shown is an average of two measurements acquired on two different areas of the sample. The second experiment measures the behavior of a single microlens. In this case, a 100X objective is aligned with the centre of one microlens. Diaphragms with different aperture diameters are used to observe the effect of the curvature of the microlens on the

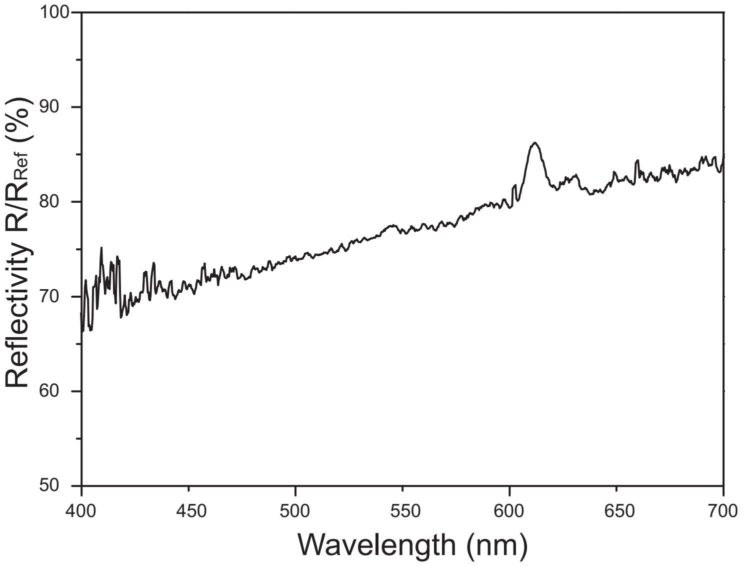

Figure 3.7: Normalized reflectivity spectrum for an area containing several nanostructured microlenses.

AR properties. The normalized reflectivity measurements are plotted (Fig. 3.8) for image diameters of 47 μm, 93 μm, 117 μm and 140 μm. The largest aperture corresponds to nearly an entire microlens. Each curve is the average of three measurements performed on different areas of the wafer. Note that the reference is always measured with the same diaphragm size as the sample.

The curves in Fig. 3.8 show that better attenuation, between 20 % and 11 %, is obtained when nearly the entire microlens is considered.

Comparing Fig. 3.6 and Fig. 3.8, one can see that the attenuation of the reflectivity is better (by roughly a factor of two) for the flat nanostructures than for the microlenses. This can be explained by the variation of the nanopillar height as a function of their position on the microlens, as shown in Fig. 3.3. An improvement of the fabrication process is necessary in order to produce a more homogeneous layer of photoresist [78]. Antireflective properties have been observed on nanostructured flat surfaces (Fig. 3.6) as well as on single microlenses (Fig. 3.8) and an area composed of several microlenses (Fig. 3.7). In this last case the attenuation of the reflectivity is greater than for the single lens, which shows that the flat area between the microlenses also contributes to this effect.

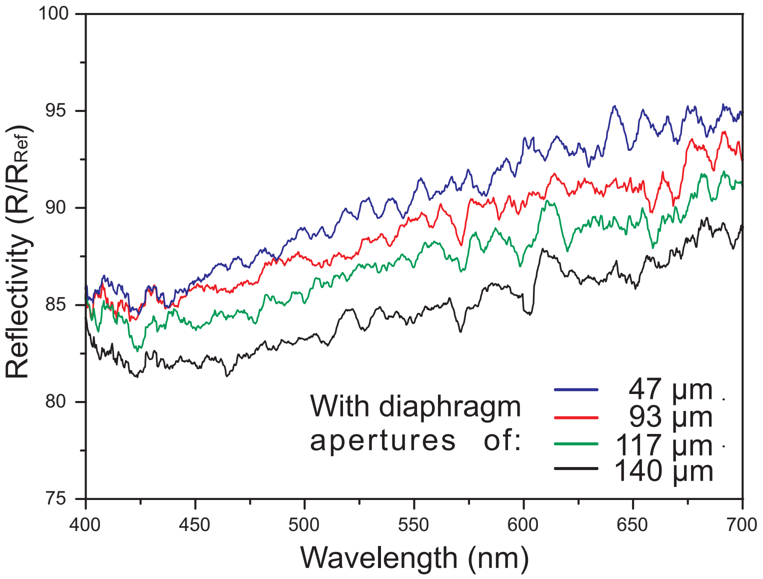

Figure 3.8: Reflectivity ratio between lenses with and without AR nanostructures for aperture diameters of 140 μm (black), 117 μm (green), 93 μm(red) and 47 μm (blue). The reflectivity is decreased between 14 % and 5 % over the visible spectrum.

3.4 Transmission characterization

In most cases, microlenses are used in transmission to focus light (e.g. onto a sensor array). To complete the study of our device, transmission measurements were performed.

The experimental setup used for transmission measurements is shown in Fig. 3.9. Due to technical issues, the sample must be illuminated from backside. In order to focus light on the side of the wafer with the structure, a condenser with a numerical aperture of NA = 0.6 is used. Light is collected by a microscope objective (100X) and analyzed using a spectrometer.

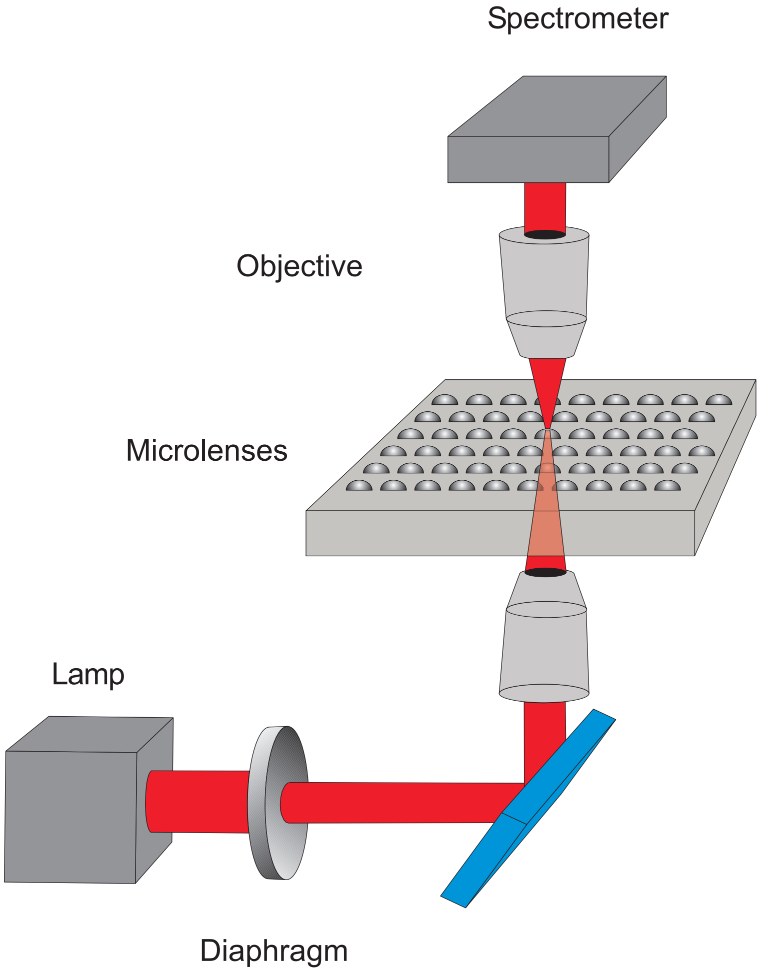

Figure 3.9: Setup for transmission measurements of microlenses with and without AR nanostructures.

Once again, the reference for the experimental measurements is a microlens without nanostructures. The normalized transmissivity curve shown in Fig. 3.10 is the smoothed mean of three measurements taken on different areas of the wafer. The enhancement of the transmission over the visible range is 3 % on average. For comparison, the maximum expected transmissivity of this device has been calculated using the ray tracing simulation software FRED from Photon Engineering (applying the Fresnel equations at the interfaces). By evaluating a microlens without nanostructures with the same illumination and collection microscope objectives (numerical apertures are taken into account) as in the experiment, we estimate the maximum transmission enhancement to be 5 % according to this model.

As in the reflectivity measurements, the fabricated non-ideal nanostructures still show significant AR properties, increasing the transmissivity of the microlenses by an average of 3 % across the visible spectrum. This improvement is also an appreciable fraction of the theoretical maximum enhancement of 9 %.

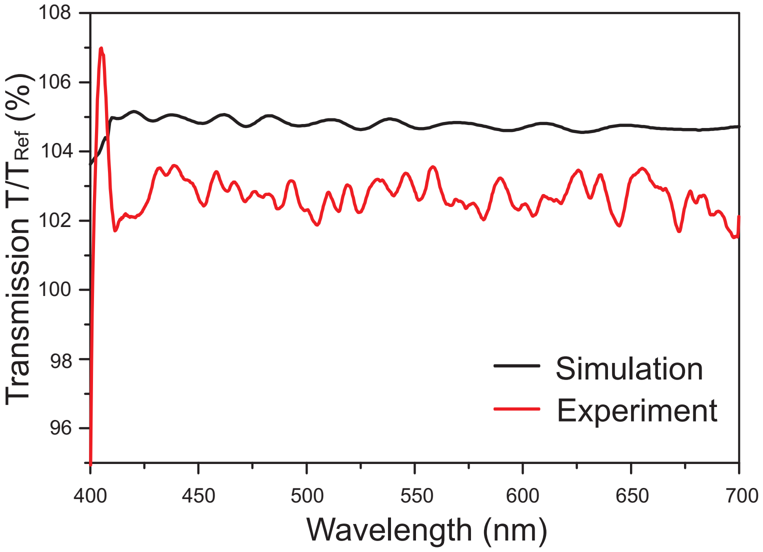

Figure 3.10: The ratio between the transmitted light through a quartz microlens with and without AR nanostructures (red curve). The black curve shows the maximum potential transmittance.

3.5 Temperature stability

One of the major challenges with other approaches for AR coatings, such as multilayer thin films, is robustness to adverse conditions such as high temperatures.

In order to test the temperature stability of our AR nanostructures, transmission measurements are performed before and after heating the sample in an oven at 250°C for one hour and cooling to room temperature. A 300 μm area is illuminated and the transmitted light is collected by a 100X microscope objective from Leica (NA = 0.9). The results in Fig. 3.11 show that the enhancement of the transmissivity stays essentially constant, which indicates that the AR nanostructure is not materially damaged by this temperature cycling. The black and red curves represent the measurements performed before and after heating respectively normalized by a reference (microlenses without nanostructures). Each curve is the average of two measurements performed on different areas of the wafer.

The durability of the AR nanostructure with respect to temperature cycling is not surprising, as the only material in the device is quartz. Moreover, as these structures are composed of a monolithic, homogenous material, they may better tolerate adverse environments, including extreme temperatures, variable humidity, immersion in liquids, or caustic surroundings. This suggests an important potential class of applications for single-material microlenses with an AR surface.

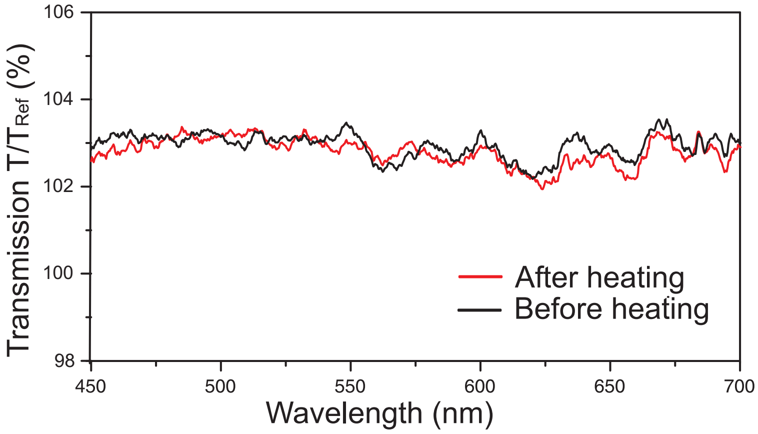

Figure 3.11: Normalized transmission spectra of the nanostructured microlenses before and after baking at 250°C for one hour.

3.6 Conclusion

In this paper, the feasibility of fabricating an anti-reflective layer by surface nanostructuring large area microlens arrays (4-inch wafer) has been demonstrated. The reduced reflectivity of the microlens surface is based on the engineered effective refractive index properties of a nanostructure, in this case an array of pillars that covers the entire surface of the microlenses. Although the structures on quartz microlens arrays are not perfect, the reflectivity measurements show a 15 % improvement compared to unstructured microlenses. Transmission measurements, obtained with a different setup show an enhancement of approximately 3 % of the transmission. Incremental improvements in the fabrication process can further improve the performance of the antireflective surface, facilitating their incorporation into more complex micro-optical systems. Deeper structure could, for instance, be realized by improving the RIE process. An antireflective treatment of the backside of the wafer, either through nanostructuring or other methods, could also be envisaged.

We have demonstrated the interference lithography technique as a suitable method for the delicate fabrication of a nanostructure on a large, non-flat surface. This work has shown promising results consistent with theoretical predictions.

Finally, we have shown that a single-material device is stable and robust, for example to variations in temperature, which suggests that these devices may be suitable for applications involving extreme environmental conditions.

Chapter 4

The superprism device

4.1 Introduction

Photonic crystals (PhCs) are composed of periodic dielectric or metallo-dielectric nanostructures that affect the propagation of electromagnetic waves by defining allowed and forbidden energy bands. Essentially, photonic crystals contain regularly repeating internal regions of high and low dielectric constants. Photons propagate through this structure – or not – depending on their wavelength. The wavelengths of light that are allowed to travel are known as modes, and groups of allowed modes form bands. Disallowed bands of wavelengths are called photonic bandgaps. This gives rise to distinct optical phenomena such as inhibition of spontaneous emission, high-reflecting omni-directional mirrors and low-loss-waveguiding, amongst others.

Since the basic physical phenomenon is based on diffraction, the periodicity of the photonic crystal structure has to be of the same length-scale as half the wavelength of the electromagnetic waves.

One of the interesting optical properties of Photonic Crystals [3, 4] is the so-called superprism effect [20, 82, 83], producing a strong angular dispersion for frequencies near the edges of the photonic bandgaps. A summary on the superprism effect is given in [84]. The superprism effect could enable compact, on-chip devices such as multiplexer-demultiplexers [85,86] or ultrafast switches [21]. In particular, a tunable superprism device would be very useful for such applications, and a number of tuning mechanisms have been explored, including electro-optic control [87,88], nonlinear materials [22,89], temperature dependent materials [90] or infiltration with liquid crystals [91, 92]. Most of the studies on demultiplexer system use PhC lattices made of air holes [93–95].

In this chapter, we investigate planar triangular-lattice PhC structures made of pillars [96, 97] and infiltrated with liquid crystals to realize a tunable superprism effect.

4.2 Design and fabrication

In order to study the superprism effect, the device, shown in the SEM image of Fig. 4.1, is realized. It is composed of an input waveguide followed by a photonic crystal region whose orientation is rotated by 15 degrees relative to the input waveguide. A planar output waveguide conducts light to the edge of the device. The PhC is composed of a triangular lattice of pillars with a period of 860 nm and a height of 340 nm. The pillars diameter is 602 nm, which represents a filling factor of 0.7. The structure is filled with liquid crystals (5CB from Merck) having refractive indices at $\lambda = 1500$ nm of $n_o = 1.51$ and $n_e = 1.63$ at room temperature and n = 1.57 above 35.5°C (isotropic liquid).

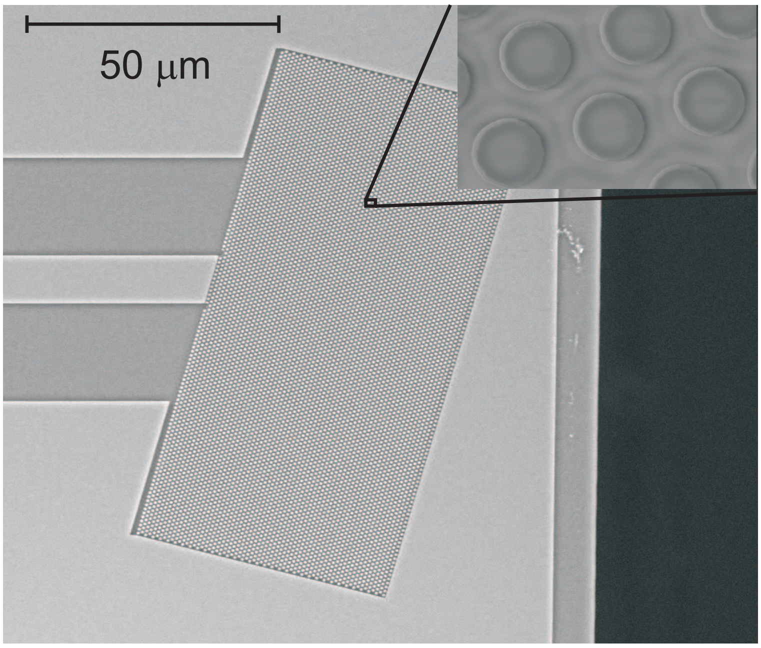

Figure 4.1: SEM picture of the superprism device fabricated on an SOI wafer. Incident light arrives from the left in the ridge waveguide, then encounters the PhC structure rotated by 15° with respect to the waveguide axis.

The samples are fabricated at the Center of MicroNanoTechnology (CMI-EPFL) by Yu-Chi Chang with a standard e-beam photolithography process on SOI wafer whose process flow is the following:

1. Cleaning the 4-inch SOI (Silicon On Insulator) wafer.
2. E-beam lithography on a spin-coated 100 nm thick photoresist (ZEP520A) and development.
3. Transferring the structures into the 340 nm thick silicon layer by Inductively Coupled Plasma Reactive Ion Etching (ICP-RIE).

4. Stripping the resist by oxygen plasma.

5. Contact mask lithography on a 8 μm thick spin-coated photoresist (AZ9260) to define the perimeter lines of the sample.

6. Transferring the perimeter lines of the sample by ICP-RIE into the 1 μm thick silicon oxyde (SiO_2) and 350 μm of the silicon bottom layer.

7. Stripping the resist by oxygen plasma and wet etching in a specific remover.

8. Separating the samples using the perimeter lines.

4.3 Theory

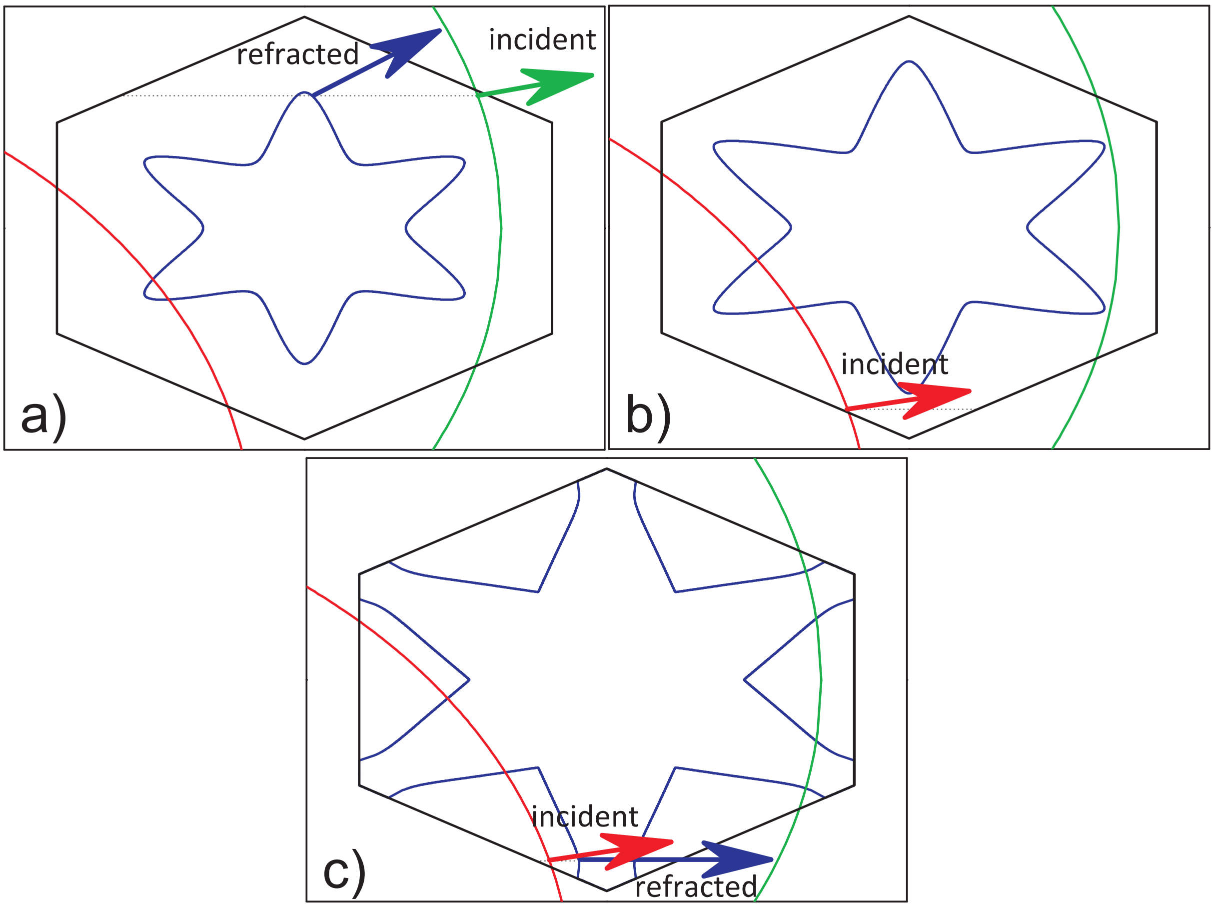

Figure 4.2: Isofrequency contours at three different wavelengths; a) $\lambda = 1522$ nm (superprism regime), b) $\lambda = 1494$ nm (forbidden band), c) $\lambda = 1463$ nm (superprism regime). The red and green curves represent two translated copies of the IFC in the incident medium.

A theoretical analysis of the PhC structure has been conducted using the MIT Photonic Bands (MPB) [98] software by Vincent Paeder from the Optics group of the *Institut de Microtechnique* (EPFL). Isofrequency contours (IFC) for band 5 (TM polarization) are shown in Fig. 4.2. They highlight two different superimposed effects. At longer wavelengths, a superprism effect is obtained due to the large curvature of the IFC. Moving towards shorter wavelengths, a forbidden band appears, caused by the transition of the incident medium IFC through the Brillouin zone (BZ) boundary [99]. This effect is entirely determined by the period of the structure. Since the incident medium IFC is large compared to the BZ, it is folded multiple times in the BZ. The incident wave vector can lie on any of the foldings depending on the angle of incidence and the frequency. By choosing the angle carefully, the wave vector can be set close to the edge of the BZ. Varying the frequency hence makes the wave vector hop from one folding to another, mimicking the presence of a bandgap. Below this gap, the incident wave matches a second region with super-refracting properties.

From the IFC, we extract the refraction angle at the PhC interface. This angle is presented in Fig. 4.3 for three values of the liquid crystal refractive index. The two discrete regions where the slope of the curves is greatest indicate a superprism effect for two of the refractive index values. In contrast, for the extraordinary index ($n_e = 1.63$), only one region exhibits a superprism effect. One can observe a red shift by increasing the refractive index of the surrounded media.

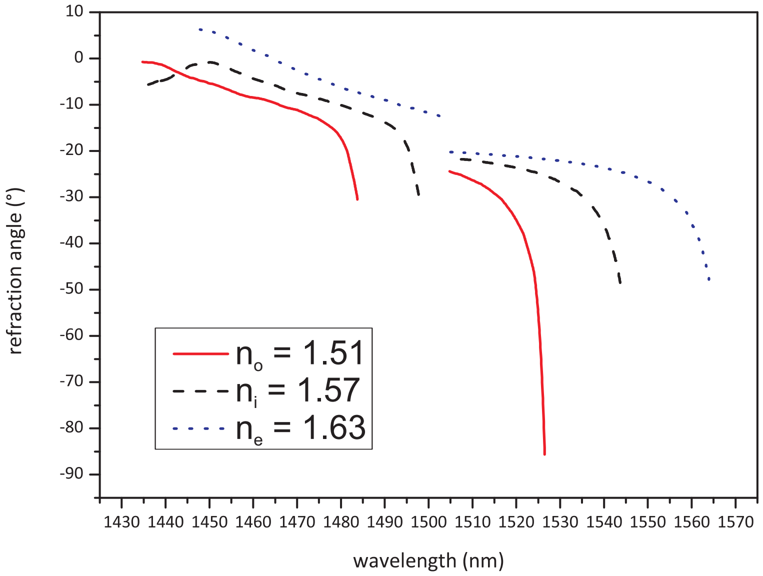

Figure 4.3: Refraction angle at the waveguide-PhC interface for three refractive index values of the liquid crystals, computed using MPB. With $n_o = 1.51$, $n_i = 1.57$ and $n_e = 1.63$ being the ordinary, isotropic and extraordinary refractive indices of the liquid crystal at 1500 nm.

4.4 FITD simulations

Two-dimensional finite integral time domain (FITD) simulations with effective index approximation have been performed on the design of the structure, using CST Microwave Studio. As expected from the MPB simulations, a superprism effect is present as shown in Fig. 4.4. A displacement of the output spot of 30 μm is obtained (solid line) corresponding to a displacement rate of 1.2 μm / nm. Note that the origin of the output spot displacement scale is defined to be at the center of the input waveguide. The dashed curve shows the output spot intensity. Large insertion losses, as describe in other work [100, 101], are particularly visible. At longer wavelengths, the intensity of the light coupled to the edge of the 4th PhC band is seen to overwhelm the effect of interest. Note that according to the MPB results, the 4th band lies outside the investigated frequency range. However, beam dispersion at the output of the waveguide and finite size effects can account for the small fraction of light transmitted in the 4th band.

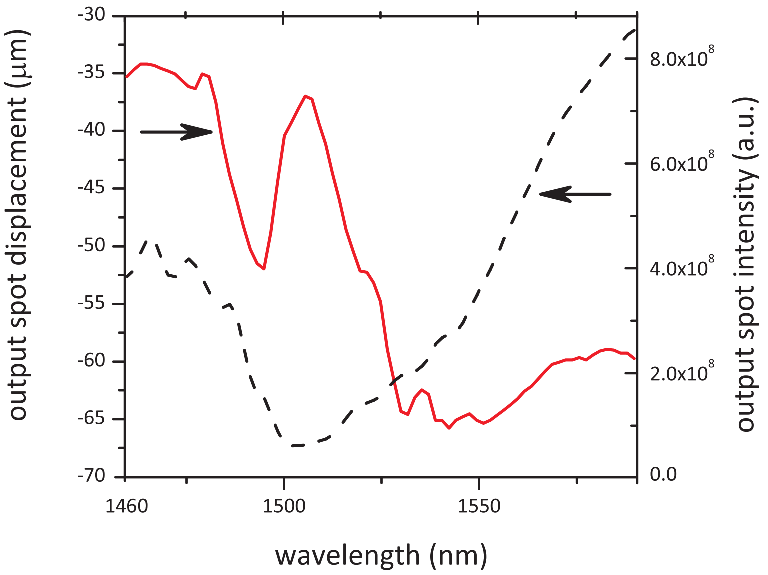

Figure 4.4: Two dimensional simulation of the structure showing the displacement of the output spot from the device (red curve) and the related intensity of the output spot (black dashed curve). The steep shift of the output spot around wavelengths 1490 nm and 1520 nm indicate a superprism effect.

Nevertheless, the simulations have exhibited two regions with a higher light dispersion where the superprism effect is present and should be confirmed experimentally.

4.5 Experimental results

In the experiment, light from a tunable laser (1460 - 1590 nm) is polarized in a TM mode and injected into the waveguide through a lensed fiber. The detection is performed by imaging the output edge using an InGaAs infrared (IR) camera (Polytec model SU320MS-1.7RT) positioned in front of the planar output waveguide. Figure 4.5 shows the schematic diagram of the setup.

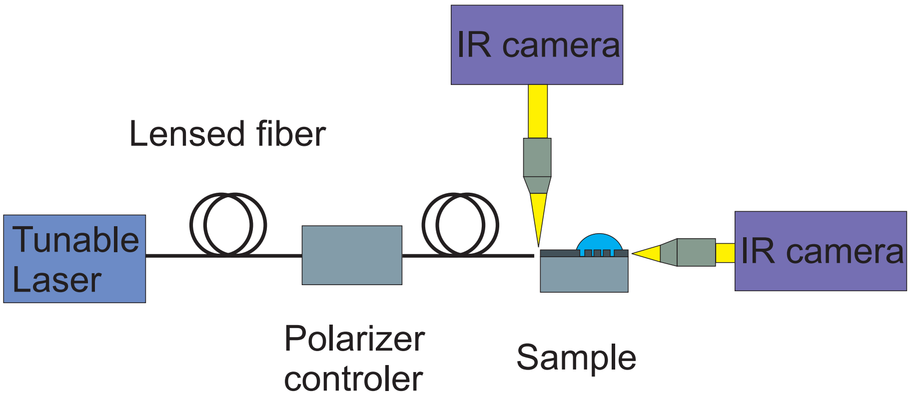

Figure 4.5: Schematic drawing of the setup used to characterize the superprism devices.

Measurements are performed with wavelength steps of 0.5 nm. Another IR camera is mounted above the sample in order to align precisely the injection into the planar waveguide. The device is designed to work with liquid crystal surrounding the structure, so, a droplet of liquid crystal is deposited on the active area.

4.5.1 Superprism effect

The experimental result (see Fig. 4.6) shows two distinct regions where a superprism effect is observed (emphasized by the red lines). Note that in Fig. 4.6 the origin of the output spot displacement is arbitrary. The greatest displacement, equal to 20.5 μm, is measured between 1541 nm and 1568 nm and corresponds to a displacement rate of 0.74 μm / nm. The region included between 1493 nm and 1515 nm exhibits a displacement rate of 0.55 μm / nm. These values are smaller than the ones predicted by the FITD model (1.2 μm / nm). This difference could arise from the difficulty of detecting the adjacent sharp dip and peak observed in Fig. 4.4. We also observe a red shift of the area of interest between the simulations and the experiment that could be due to imperfect alignment of the liquid crystal with respect to the pillars. Nevertheless, the superprism effect is demonstrated for the first time for a PhC made of silicon pillars infiltrated with liquid crystals.

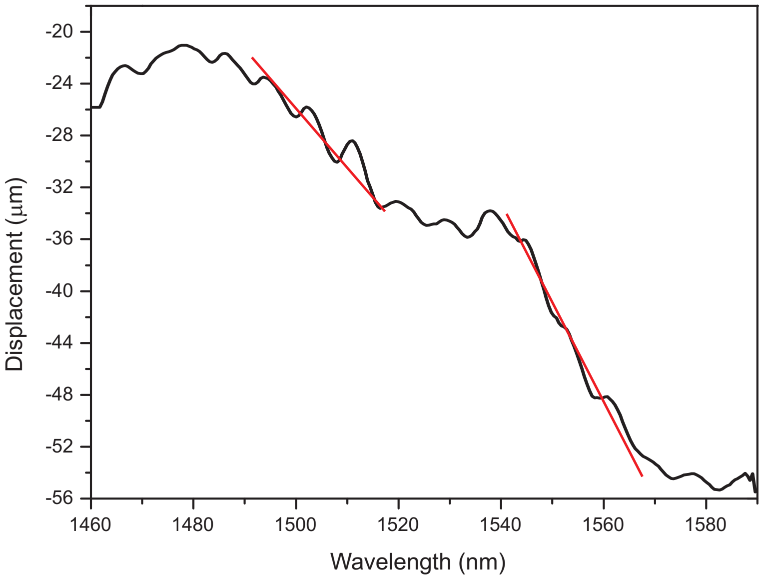

Figure 4.6: Experimental result demonstrating a superprism effect in the infrared range using silicon pillars surrounded by liquid crystals. The red lines indicate the regions where the effect is obtained.

4.5.2 On/off switch effect by heating the liquid crystal

In addition to the supeprism effect, an on/off switch functionality can also be realized due to the infiltrated liquid crystal and their phase variation with temperature. The optical properties of the liquid crystal changes from anisotropic (oriented) to isotropic above 35.5°C. In this experiment, a Pelletier element is used to heat the silicon layer and the liquid crystal from room temperature to 45°C. Fig. 4.7 shows the images, obtained by the in-plane camera, of the spot refracted by the PhC at a wavelength of 1510 nm. Figures 4.7 a) and c) show the spots before and after the heating whereas Fig. 4.7 b) shows the same area with the liquid crystal in the isotropic state. The spots intensity variation between Fig. 4.7 a) and Fig. 4.7 c) are most likely explained by the automatic calibration of the infrared camera. The disappearance of the output spot at the higher temperature is due to the extreme sensitivity of the superprism effect to the surrounding refractive index. This temperature-based (slow) on/off switch could be enhanced by using the electro-optic properties of the liquid crystal.

Note that to obtain the same displacement of the spot using a standard flint glass prism ($n = 1.76$ and $dn / d\lambda = 0.00051$ nm^{-1} [102]), the device would occupy more 5 mm and the light would be in free propagation mode, whereas the active zone of our device is smaller than 50 μm and the light is confined in a waveguide. Moreover, the liquid crystal infiltration adds a second functionality that makes our structure promising for the future generation of very compact optical systems.

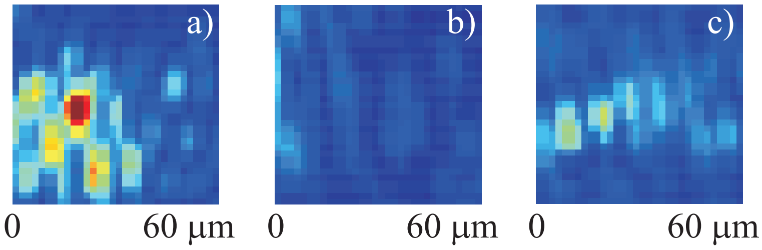

Figure 4.7: An on/off switch effect is shown from the images from the infrared camera where the dispersed light spot appears at room temperature a) and c) respectively before and after a heating at 45°C. At the higher temperature there is no observable output spot b).

4.5.3 Discussion

In our experiment, we have used the refractive index variation of the liquid crystal using its physical state (isotropic and anisotropic) sensitivity to the temperature. The experimental deposition of the droplet of liquid crystal onto the active area of the wafer is fast and easy to realized. Nevertheless, two points must not be neglected, particularly when considering further development of the device.

The first point, illustrated by Fig. 4.8, is the long time needed to heat and cool the liquid crystal. The black curve show that the time to stabilize the liquid crystal at 45°C from room temperature is approximately 7 minutes (420 sec.). The time to return to the initial state by switching off the heater is equivalent, as shown with the red dashed

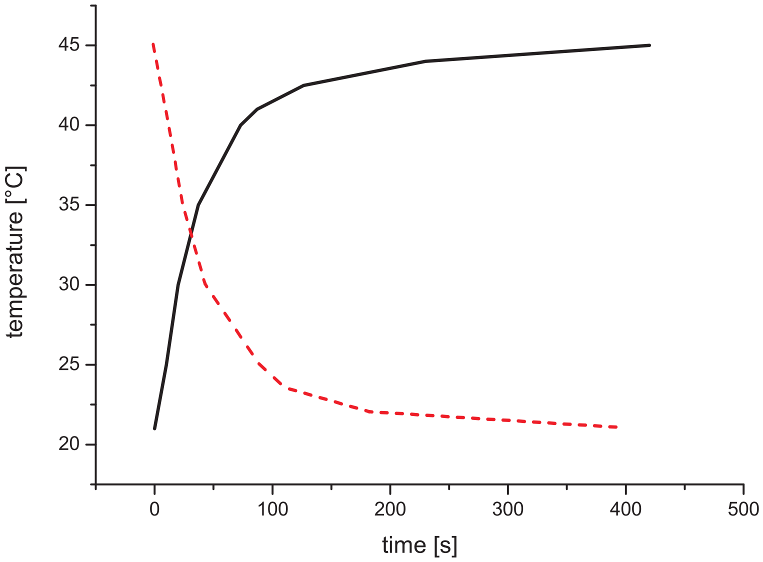

Figure 4.8: Heating (black curve)and cooling (red dashed curve) time necessary to heat the liquid crystal from 21°C to 45°C and vice versa, with the sample standing on the Pelletier element.

curve. Note that our sample simply stands onto the Pelletier element. Consequently, the heat transfer performance could be enhanced with a more advanced heater design or by choosing another method to heat the liquid crystal such as an infrared light source or a laser [103].

The second point to be considered is that in some cases, one can observe a displacement of the intensity spot that does not completely corresponds to the simulations. Indeed, in Fig. 4.9, the superprism effect is clearly observable (red line) only in one region rather than in two regions, as expected from Fig. 4.3 and Fig. 4.4. The displacement is equal to 10 μm between 1511 nm and 1524 nm which corresponds to a displacement rate of 0.77 μm / nm. This result (only one superprism region) can be explained by the liquid crystal rearrangement when cooling down. Indeed, the orientation of liquid crystals is not precisely controlled in the anisotropic phase in our device.

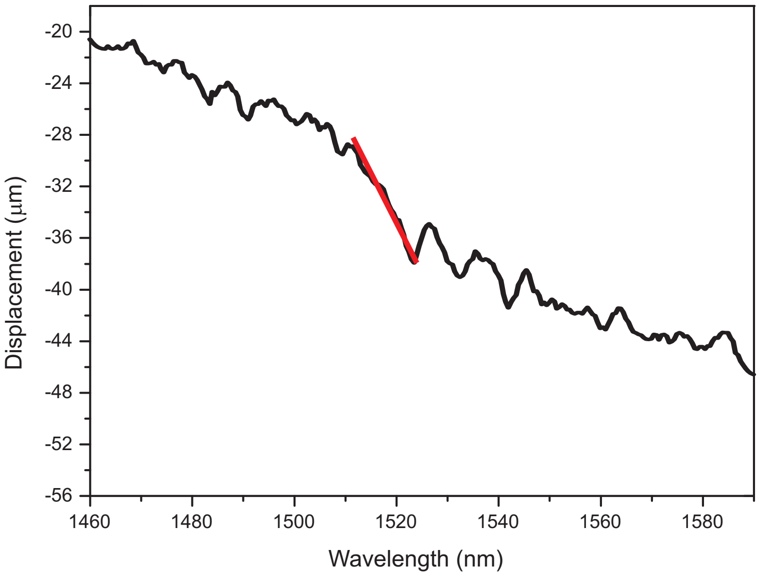

Figure 4.9: Displacement of the output spot where only one region exhibits a superprism effect of 0.77 μm / nm (emphasized by the red line).

These two points that appear to be crucial for further developments could both be overcome by using the electro-optic properties of the liquid crystals to orient the particles and thus, control the refractive index. This method requires a more complex design where the liquid crystal is sandwiched between electrodes.

4.6 Conclusion

We have simulated, fabricated and characterized a device exhibiting a superprism effect in a two-dimensional PhC made of silicon pillars infiltrated by liquid crystals. We achieve a 0.74 μm shift per nm change in wavelength in the near infrared, which is more than 100 times better than a quartz prism. We have also shown that, with the same device, two functionalities can be achieved: a superprism effect and an on/off switch. The obtained results and the standard silicon-based technology used to fabricated our device, open the door to industrial development to realize ultra compact, highly capable demultiplexers for the telecommunication community. An improved time response and control of the orientation of the liquid crystals would be achieved by applying a voltage. The next step to develop further this promising device could be to ameliorate the beam compactness as has been done in recent work for a rhombohedral lattice of holes [104]. Another goal for our device will be its fabrication with interference lithography, which would allow efficient production at very low cost.

Chapter 5

Photonic crystal cavity used as a single wavelength tunable filter

The tunability of photonic crystal effects can be achieved by several methods (not exhaustive) such as:

- Liquid crystals infiltration, where the orientation of the liquid crystals is varied by an applied voltage. An other possibility is to use their temperature sensitivity to tune their refractive indices [105].
- Pockels electro-optic effect, where an applied voltage is used to tune the birefringence of the material proportionally to the electric field. The effect occurs only in crystals that lack inversion symmetry, such as lithium niobate $LiNbO_3$ [106] and in other noncentrosymmetric media such as electric-field poled polymers or glasses.
- Kerr effect, where the refractive index of the material change with the square of the applied electric field [107].
- Thermo-optic materials, where the refractive index of the material is obtained by varying the temperature. This effect can be observed specially for polymers [108].
- Mechanically by approaching an AFM tip, where the AFM tip induces a damping effect when approaching a PhC cavity [109].

In this chapter, we present a tunable photonic crystal filter where liquid crystals (5CB from Merck) are infiltrated inside the nanostructure [110] to achieve tunability of the optical characteristics. At room temperature the liquid crystal is in its order phase and exhibits anisotropy. The orientation at the silicon surface is preferentially parallel to the surface [111]. Above the phase transition temperature for 5CB at 35.5°C the liquid crystal is isotropic. The refractive indices vary when changing the phase of the liquid crystals from anisotropic (with ordinary and extraordinary refractive indices $n_o = 1.51$ and $n_e = 1.63$) to isotropic ($n_i = 1.57$). If the liquid crystals are infiltrated into the nanostructure, we can act on the photonic bandgap properties of the device by changing the temperature.

The filtering is achieved by placing a nanocavity in the center of a photonic crystal waveguide. The aim of this study is to shift the transmission peak generated by the nanocavity by changing the refractive index and the state of the liquid crystals infiltrated into the device. Tuning the position of a Photonic band gap using liquid crystal infiltration has already been shown [112,113] as well as temperature shifting of a resonant peak using the temperature dependency of the liquid crystal anisotropic phase [114]. Recent works have even demonstrated the tuning of a resonance peak using the same effect as we use [115,116] but the resonant cavity was not embedded in a photonic waveguide.

5.1 Design and fabrication

The basis for the design of the structure studied in this chapter is presented in Fig. 5.1 a) and b). The device consists of a PhC waveguide in a freestanding silicon membrane. A nanocavity is inserted in the center of the guide. The purpose of this study is to characterize the behavior of this nanocavity depending on the material infiltrating the cavity - liquid crystals or air. The device is composed of a 340 nm thick silicon (Si) membrane on a layer of Silicon Oxide (SiO_2, thickness of 1 μm) deposited on a substrate of Silicon. The photonic crystal is composed of 34 rows of holes in the propagation direction and 16 periods in the transverse direction. The PhC waveguide consists of 1 row of missing holes. The hole diameter is d = 300 nm and the period is p = 450 nm (see Table 5.1). Light reaches the PhC waveguide using a taper from 10 μm at the input of the sample to 580 nm at the input of the photonic waveguide. Note that using a freestanding membrane should facilitate the infiltration of liquid crystals in the PhC structure.

Two types of nanocavities have been studied. They are shown in Fig. 5.1 c) and d) and the parameters are listed in Table 5.1. The first, composed of 7 holes, is designed to work when surrounded by air (without liquid crystals) and the second, composed of 5 holes, works when infiltrated with liquid crystals. The temperature dependency of the liquid crystal is used to modify its refractive index [117].

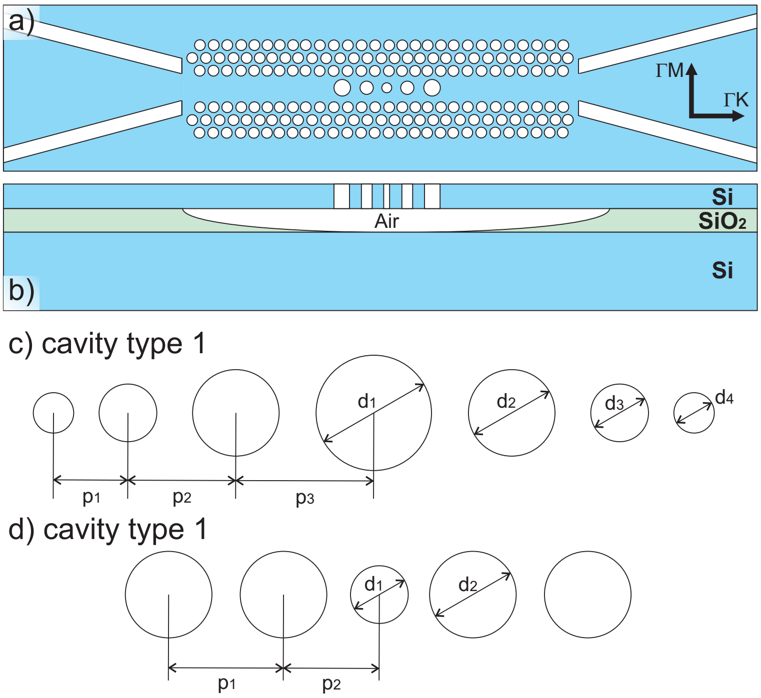

Figure 5.1: Schematic diagram of the structure: a) top view, b) cross section along the propagation direction, in the middle of the cavity. Cavity design and parameters for the nanocavity design to operate c) without liquid crystal and d) with infiltration of liquid crystals.

Table 5.1: Parameters of the two types of nanocavities.

	Cavity type	1	2
Periods	$p_1(nm)$	360	380
	$p_2(nm)$	360	470
	$p_3(nm)$	482	–
Diameters	$d_1(nm)$	290	220
	$d_2(nm)$	260	260
	$d_3(nm)$	200	–
	$d_4(nm)$	170	–
PhC parameters	$p_{PhC}(nm)$	450	430
	$d_{PhC}(nm)$	300	320

These samples have been fabricated at the Center of MicroNanoTechnology (CMI-EPFL) by Armando Cosentino from the Optics group of the *Institut de Microtechnique* (EPFL). The process flow is the following:

1. Cleaning the 4 inch Silicon On Insulator (SOI) wafer.

2. E-beam lithography on a spin-coated 100 nm thick e-beam resist (ZEP520A) and development.

3. Transferring the structures into the 340 nm thick silicon layer by Inductive Coupled Plasma Reactive Ion Etching (ICP-RIE).

4. Stripping the resist by oxygen plasma.

5. Contact mask lithography on an 8 μm thick spin-coated photoresist (AZ9260) to define the perimeter lines of the sample.

6. Transferring the perimeter lines by ICP-RIE into the 1 μm thick silicon oxide (SiO_2) and 350 μm of the silicon substrate layer.

7. Stripping the resist by oxygen plasma and wet etching in a specific remover.

8. Removing the SiO_2 under the PhC area by HF vapor etching to create the free standing membrane.

9. Separating the samples using the perimeter lines.

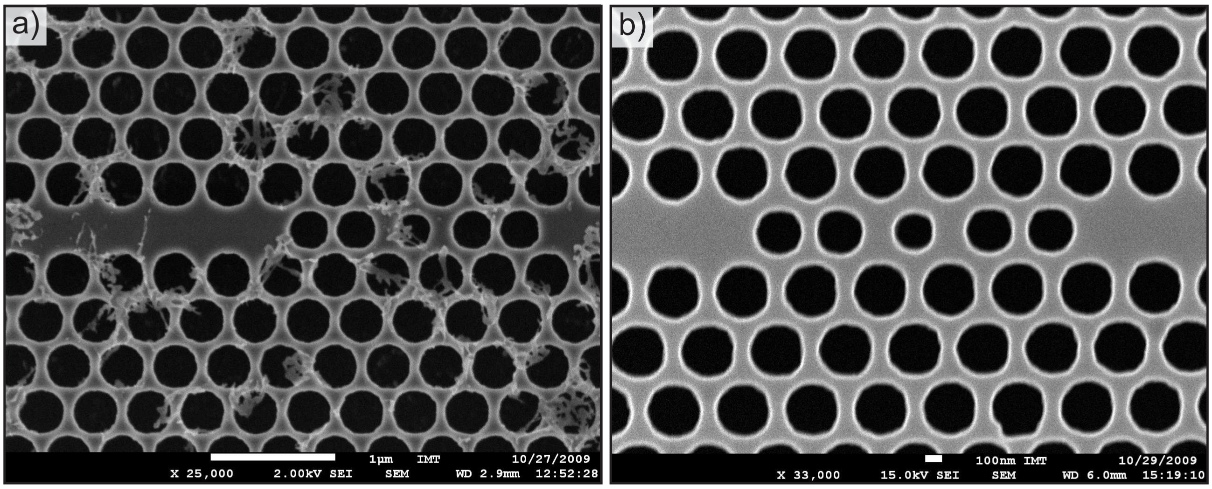

Figure 5.2: SEM image of the sample (nanocavity type 2): a) before cleaning, b) after cleaning.

The SEM pictures presented in Fig. 5.2 show a cavity of type 2. One can note the good accuracy between the designed and fabricated devices. Nevertheless, one can also observe in Fig. 5.2 a) that some photoresist used in the fabrication remains on the surface of the sample. This can result in poor infiltration of the liquid crystals into the nanocavity. Additional cleaning steps leads to the clearer structures as shown in Fig. 5.2 b). Note that measurements on both structures have been performed.

5.2 Nanocavity characterization

The characterization setup is described in Fig. 5.3. A fibered infrared tunable laser (1460 nm $<\ \lambda\ <$ 1590 nm) is used as a light source (*Hewlett Packard Tunable laser source 8168F*). Light passes through a fibred polarization controller and is injected into the waveguide using a tapered optical fiber. In order to avoid the noise due to light passing above the sample or through the substrate, the light is collected on top of the output waveguide as shown in Fig. 5.3. This is possible due to a small step created on the sample that reflects a part of the output light. Moreover, since the waveguide is very thin, the output beam is highly divergent and more light can be collected using a system composed of a long focal length microscope objective (Leica ×20, NA = 0.4)and a highly sensitive InGaAs infra-red camera (*Polytec SU 320 MS-1.7RT*). The intensity of light coming from the cavity can be measured as a function of the wavelength.

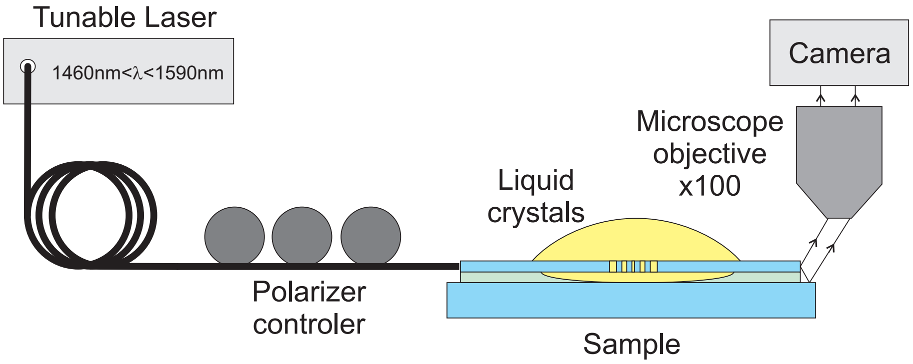

Figure 5.3: Schematic diagram of the setup used for the device characterization.

Three-dimensional simulations have been performed by Qing Tan from the Optics group of the *Institut de Microtechnique* (EPFL) using a commercial FITD software (CST). The red curve in Fig. 5.4 shows the computed spectrum. One can observe a transmission peak centered at $\lambda = 1501$ nm, having a full width at half maximum of FWHM = 8 nm and a maximum intensity of $I_{max} \simeq 63$ % of the incident light. The black curve represents the experimental measurements. Note that the two transmissivity scales are different and cannot be directly compared. Nevertheless, one can observe the presence of a transmission peak centered at $\lambda = 1536$ nm.

Moreover a shift of $\Delta\lambda = 35$ nm can be observed between the theoretical and the experimental peaks. This can be explained by a small change in the diameters of the holes of the nanocavity. Figure 5.5 shows the results of simulations where the sizes of the holes of the nanocavity have been changed by less than 2 % (20 nm), which is close to the resolution limit of e-beam lithography. A displacement of the resonance peak of $\Delta\lambda \simeq 70$ nm is obtained. The difference between the two peaks in Fig. 5.4 can thus be attributed to fabrication errors on the order of 10 nm.

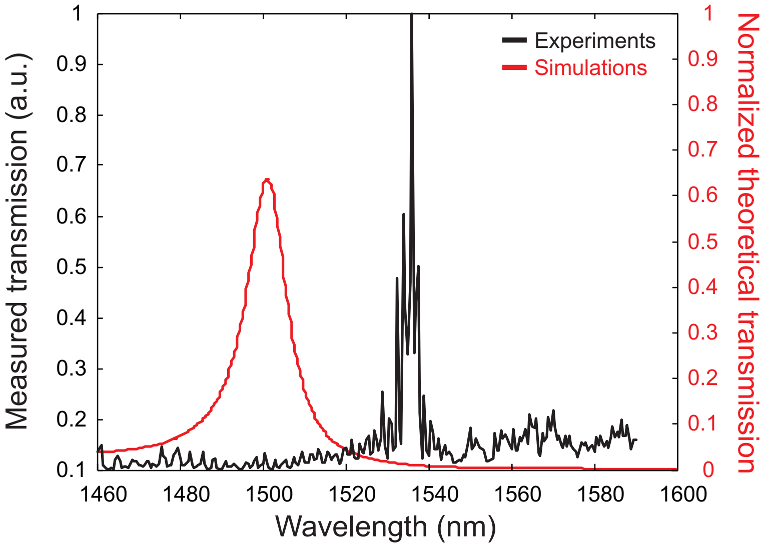

Figure 5.4: Comparison between experimental measurements (black curve) and simulation results (red curve) of the transmission through the nanocavity without liquid crystal (type 1).

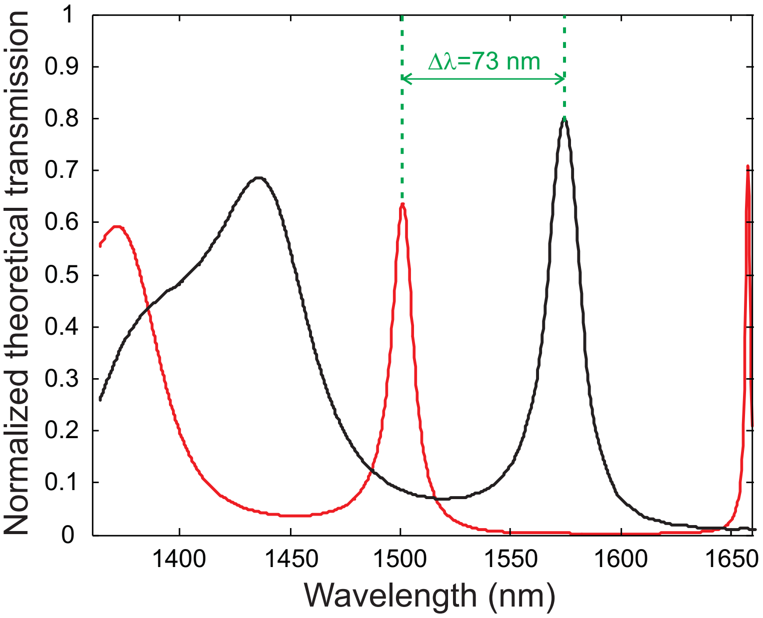

Figure 5.5: Simulation of the type 1 cavity with a variation of 20 nm of the diameters of the holes of the cavity.

5.3 Tunable nanocavity measurements

One of the most important parameters in this study is the liquid crystal infiltration inside the nanocavity holes. In order to define the influence of the presence or absence of the liquid crystals, we have performed FITD calculations for three different situations. The first one is the ideal case, where liquid crystals fill the cavity as well as the area above and below the Silicon membrane (Fig. 5.6 a)). The second case considers liquid crystals only above and below the cavity, but not inside the holes (Fig. 5.6 b)). Finally, the third case is the non-infiltration configuration where the liquid crystals are only found above the silicon membrane (Fig. 5.6 c)).

The parameters used for modeling the liquid crystals consist of the indices of refraction at two temperatures. At room temperature, the liquid crystals are in planar orientation and the optical propagation depends mostly on the extraordinary index ($n_e = 1.63$ at $\lambda = 1.55\ \mu$m). To obtain the isotropic phase of the liquid crystal, it must be heated to a temperature of $T_c = 35.5$°C or above. In our experiment the temperature is set to T = 45°C, and the index of refraction of the isotropic phase is assumed to be $n_i = 1.57$ [118].

Figure 5.6 presents for these cases, the response of the cavity at the room temperature (red curve) and at T = 45°C (black curve). Three principal effects are observed when the infiltration of the liquid crystals is reduced. First, the maximal amplitude of the transmission peaks decreases drastically. Second, the photonic band gap and the transmission peak shift to the blue and consequently the peak changes position inside the photonic band gap. Third, the shift between the two peaks corresponding to the state of the liquid crystals decreases from 32 nm (complete infiltration of liquid crystals) to 8 nm (liquid crystals only at the surface of the structure).

Using the same experimental setup as above, we have performed transmission measurements at the two temperatures through the sample before cleaning (see Fig. 5.2 a)). The results are presented in Fig. 5.7. The expected shift corresponds to Fig. 5.6 c), where liquid crystals are not infiltrated in the nanostructure due to the residual resist that alters the surface tension of the sample and partially covers the holes.

One can observe that the transmission peak does not shift when the state of the liquid crystals changes. In that case, the orientation of the liquid crystals are perturbed by the remaining resist which make the surface of the sample rough. It means that the liquid crystal has no preferential orientation and is in an isotropic-like state, and the refractive index is close to n_i.

In order to facilitate the orientation of the liquid crystals, the sample has been cleaned (as shown in Fig. 5.2 b)) and measured again (Fig. 5.8). The cleaning of the sample was performed using a sulfuric acid (H_2SO_4) bath concentrated at 90%, followed by an oxygen plasma. A shift of $\Delta\lambda = 13$ nm is observed. Note that the cleaning process has an impact on the signal to noise ratio. The obtained results, compared with the simulations shown in Fig. 5.6, suggest that the liquid crystals are infiltrated in the nanocavity. A better infiltration of the liquid crystals could be obtained using a vacuum chamber [110]. In our experiments, a smaller shift is measured than is predicted numerically. This result is most likely due to a different orientation of the liquid crystals in the holes and at the surface

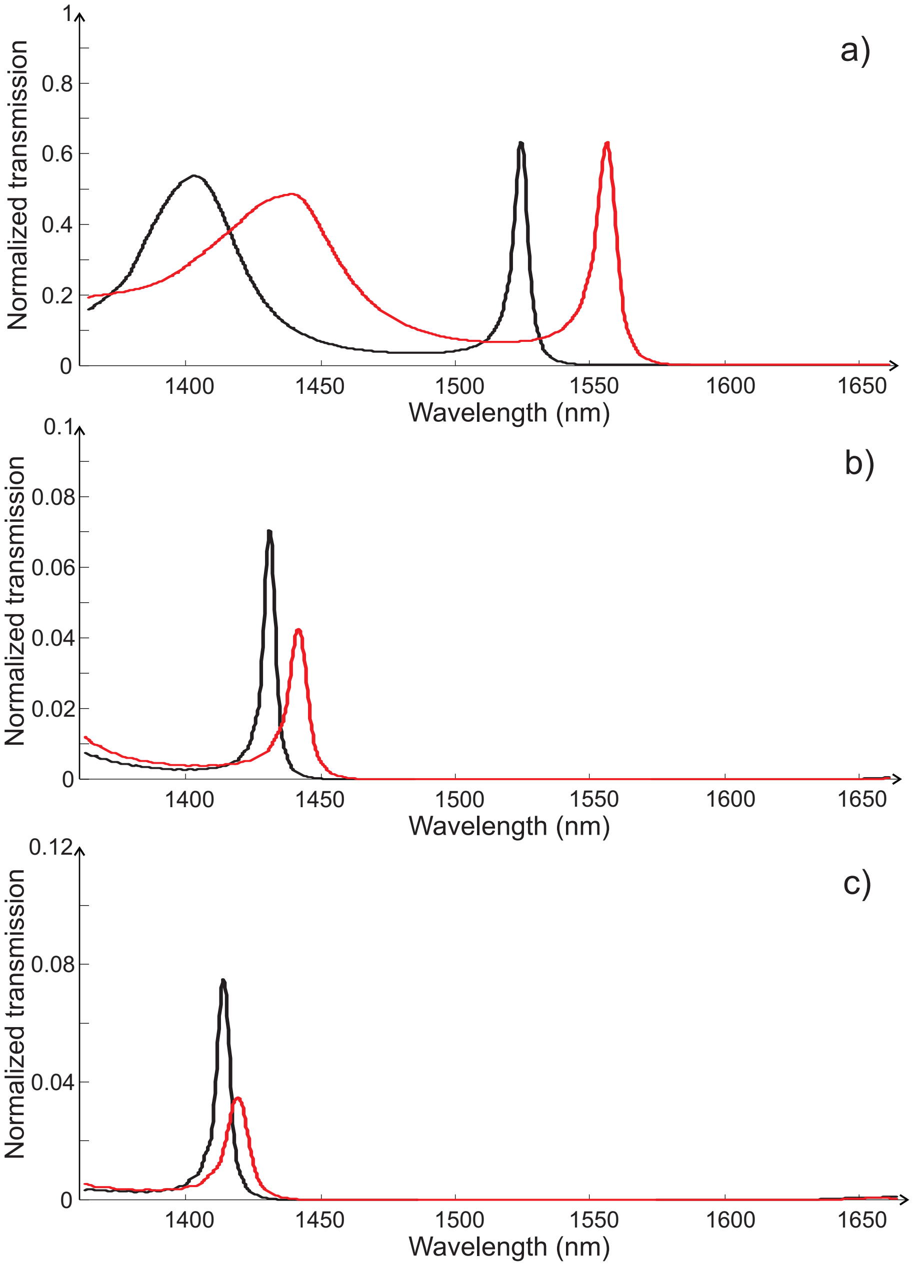

Figure 5.6: Calculated variation in the response of the nanocavity as a function of the infiltration of liquid crystals at room temperature (red curve, $\mathrm{n}_e = 1.63$) and at $\mathrm{T} = 45^\circ C$ (black curve, $\mathrm{n}_i = 1.57$): a) liquid crystals surrounding and infiltrating into the holes of the nanocavity, b) liquid crystals above and bellow the nanocavity but not in the holes, c) liquid crystals only above the membrane (no infiltration of the nanocavity).

of the sample. This orientation can unfortunately not be verified with the present setup.

To summarize, we have shown that our structures exhibit a resonant peak inside the photonic band gap of the PhC slab. The wavelength tunability of the peak has

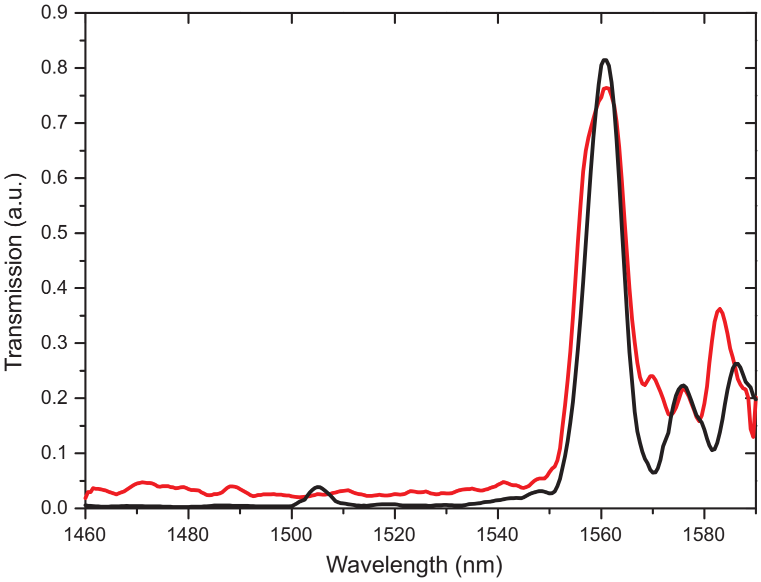

Figure 5.7: Experimental measurements of the response in transmission of the nanocavity infiltrated by liquid crystals. The red curve corresponds to the room temperature (anisotropic liquid crystals), the black curve corresponds to a temperature of 45°C (isotropic liquid crystal).

been demonstrated with simulations and experimental measurement using liquid crystals infiltrated into the cavity. The refractive index variation was obtained using the different phases of the liquid crystals (anisotropic and isotropic).

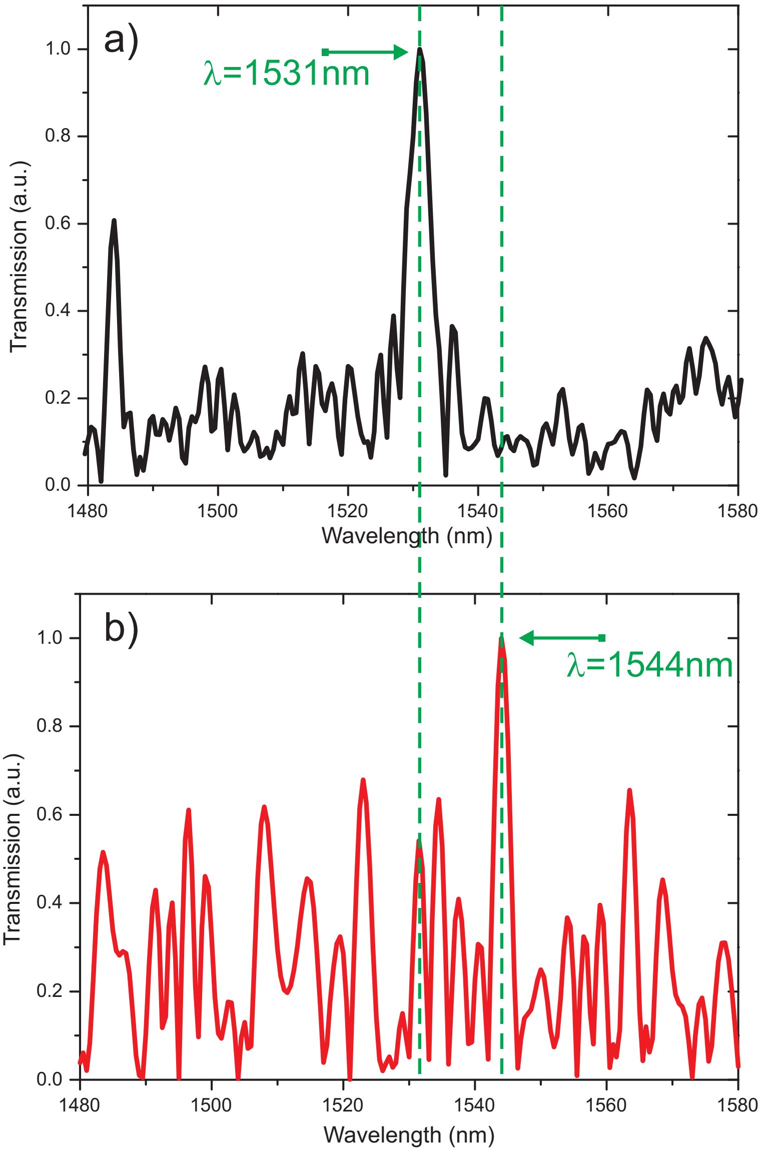

Figure 5.8: Experimental measurements of the response in transmission of the nanocavity infiltrated by liquid crystals (device shown in Fig. 5.2 b). a) The black curve corresponds to a temperature of 45°C (isotropic liquid crystal), b) the red curve corresponds to the room temperature (anisotropic liquid crystal).

5.4 Conclusion

We have demonstrated that the response of a filter based on our specific photonic crystal nanocavity design exhibits a transmission peak in the telecommunications wavelength range. Using the different phases of liquid crystals infiltrated into the cavity, the transmission peak can be tuned. The importance of a good infiltration of liquid crystals inside the cavity has also been demonstrated. to the best of our knowledge, we have shown the first tunable transmission peak produced by a resonant cavity embedded in a PhC waveguide using temperature sensitivity of the liquid crystal phase. In principle, this concept could be used as a filter or sensor for different applications where the response time is not crucial. Some example include environmental sensing, wavelength division multiplexing (WDM) or security sensors. The particular behavior of the liquid crystals with respect to temperature variations has been used to tune the nanocavity. In future work, the sample could be modulated using an applied electric field, which can induce faster index changes and consequently a higher modulation frequency.

Chapter 6

Conclusion

In this thesis, the research that I have conducted at the *Institut de Microtechnique* has been presented. The main topic was sub-micrometer periodic optical structures that have been treated from two different points of view: the fabrication with interference lithography and the characterization of photonic crystal devices in the infrared range.

For the fabrication part, an interference photolithography technique has been used to produce one- and two-dimensional gratings whose periodicity can be chosen between 250 nm and a few micrometers. It has been shown that a large area (a full 4 inch wafer) could be coated in a single step faciliting fast fabrication at a relatively low cost. Methods to reduced standing wave effects have been applied and discussed. As it can be useful to modify the periodic lattice, depending on the target device, a micro mask aligner stand has been developed to be easily combined with the interference lithography process. For the same purpose, a process to introduce defects into the PhC lattice has been developed using a standard microscope stand. The capability of modifying a single row of a sub-micrometer period triangular lattice of pillars has been demonstrated.

The interference lithography technique has been demonstrated to produce 270 nm period square gratings on top of a 4 inch wafer covered by microlenses. A process to coat a very thin photoresist layer onto a non-flat surface (in this case a microlens array), was developed. The nanostructured surface, transferred into the quartz, exhibited a 15 % attenuation of the surface reflectivity and a 3 % enhancement of the transmitted light over the visible spectral range. Due to the monolithic nature of the resulting structure, this device was shown to be extremely durable, showing little variation in its optical characteristics after temperature cycling to 250°C and back to room temperature.

The superprism effect has been studied with simulations as well as demonstrated experimentally on a triangular latice photonic crystal made of silicon pillars infiltrated with liquid crystals. The structures were fabricated by e-beam lithography on a Silicon on Insulator wafer. A displacement of the output light spot of 20.5 μm has been measured for a wavelength variation of 27 nm in the near infrared region for a structure length of 70 μm. Moreover, due to the dependence of the liquid crystal refractive index on temperature, an on/off switching of the output light spot has been demonstrated by modifying the temperature of the liquid crystals from room temperature to 45°C.

Finally, a resonant cavity in a photonic crystal waveguide has been simulated and experimentally characterized. The tunability of the device when infiltrated with liquid crystals has been demonstrated. The resonant peak shift, when heating the device from room temperature to 45°C, has been shown to be 32 nm from the simulations and only 13 nm from the experiment. This difference is explained by the incomplete infiltration of the liquid crystals into the photonic crystal structure.

To conclude, several previously unexplored approaches for optical nanostructure fabrication and design have been investigated, and example devices manufactured as well as characterized. Specifically, optical interference lithography was used to produce nanostructured devices on relatively large areas, and liquid crystal infiltration was used in conjunction with SOI PhC structures to modulate device resonance characteristics. These are but a few examples of a large range of useful photonic elements and devices that could be produced using standard microfabrication materials and processes. Based on this commonality, one can envision larger-scale integration of devices, ultimately leading to the realization of entire photonic systems on a single chip. As this technology evolves, the degree of functional integration will increase, while production costs decrease, facilitating an ever-growing range of practical applications, including optical communications and information processing, spectroscopy and environmental monitoring, as well as biomedical sensing and chemical trace detection.

Bibliography

[1] E. Loewen, *Diffraction Gratings and Applications* (Library of Congress, 1997).

[2] J. W. S. Rayleigh, "On the remarkable phenomenon of crystalline reflexion described by Prof. Stokes," Phil. Mag. **26**, 256–265 (1888).

[3] E. Yablonovitch, "Inhibited Spontaneous Emission in Solid-State Physics and Electronics," Physical Review Letters **58**(20), 2059–2062 (1987).

[4] S. John, "Strong localization of photons in certain disordered dielectric superlattices," Phys. Rev. Lett. **58**(23), 2486– (1987).

[5] H. A. Macleod, *Thin-Film Optical Filters* (Institute of Physics Publishing, London, 1986).

[6] K. O. Hill, Y. Fujii, D. C. Johnson, and B. S. Kawasaki, "Photosensitivity in optical fiber waveguides: Application to reflection filter fabrication," Applied Physics Letters **32**(10), 647–649 (1978).

[7] K. Iga, "Vertical-cavity surface-emitting laser: Its conception and evolution," Japanese Journal of Applied Physics **47**(1, Part 1), 1–10 (2008).

[8] M. Qiu, M. Mulot, M. Swillo, S. Anand, B. Jaskorzynak, A. Karlsson, M. Kamp, and A. Forchel, "Photonic crystal optical filter based on contra-directional waveguide coupling," Appl. Phys. Lett. **83**, 5121 (2003).

[9] S. Olivier, M. Rattier, H. Benisty, C. Weisbuch, C. J. M. Smith, R. M. De La Rue, T. F. Krauss, U. Oesterle, and R. Houdré, "Mini-stopbands of a one-dimensional system: The channel waveguide in a two-dimensional photonic crystal," Phys. Rev. B **63**(11), 113,311– (2001).

[10] S. Olivier, H. Benisty, M. Rattier, C. Weisbuch, M. Qiu, A. Karlsson, C. Smith, R. Houdré, and U. Oesterle, "Resonant and nonresonant transmission through waveguide bends in a planar photonic crystal," Appl. Phys. Lett. **79**, 2514–2516 (2001).

[11] A. Talneau, P. Lalanne, M. Agio, and C. M. Soukoulis, "Low-reflection photonic-crystal taper for efficient coupling between guide sections of arbitrary widths," Opt. Lett. **27**(17), 1522–1524 (2002).

[12] O. J. Painter, A. Husain, A. Scherer, J. D. O'Brien, I. Kim, and P. D. Dapkus, "Room Temperature Photonic Crystal Defect Lasers at Near-Infrared Wavelengths in InGaAsP," J. Lightwave Technol. **17**(11), 2082– (1999).

[13] M. Loncar, T. Yoshie, A. Scherer, P. Gogna, and Y. Qiu, "Low-threshold photonic crystal laser," Appl. Phys. Lett. **81**, 2680–2682 (2002).

[14] Y. Akahane, T. Asano, B.-S. Song, and S. Noda, "High-Q photonic nanocavity in a two-dimensional photonic crystal," Nature **425**(6961), 944–947 (2003).

[15] J. Vuckovic, M. Loncar, H. Mabuchi, and A. Scherer, "Design of photonic crystal microcavities for cavity QED," Phys. Rev. E **65**(1), 016,608– (2001).

[16] L. Fekete, F. Kadlec, P. Kuzel, and H. Nemec, "Ultrafast opto-terahertz photonic crystal modulator." Optics letters **32**(6), 680–682 (2007).

[17] L. Gu, W. Jiang, X. Chen, L. Wang, and R. T. Chen, "High speed silicon photonic crystal waveguide modulator for low voltage operation," Applied Physics Letters **90**, 071,105 (2007).

[18] Y. Jiang, W. Jiang, L. Gu, X. Chen, and R. T. Chen, "80-micron interaction length silicon photonic crystal waveguide modulator," Applied Physics Letters **87**, 221,105 (2005).

[19] D. Beggs, T. White, L. Cairns, L. O'Faolain, and T. Krauss, "Demonstration of an integrated optical switch in a silicon photonic crystal directional coupler," Physica E: Low-dimensional Systems and Nanostructures **41**(6), 1111–1114 (2009).

[20] H. Kosaka, T. Kawashima, A. Tomita, M. Notomi, T. Tamamura, T. Sato, and S. Kawakami, "Superprism phenomena in photonic crystals," Phys. Rev. B **58**(16), 10,096 (1998).

[21] J. Amet, F. I. Baida, G. W. Burr, and M.-P. Bernal, "The superprism effect in lithium niobate photonic crystals for ultra-fast, ultra-compact electro-optical switching," Photonics and Nanostructures - Fundamentals and Applications **6**(1), 47–59 (2008).

[22] S. Diziain, J. Amet, F. I. Baida, and M.-P. Bernal, "Optical far-field and near-field observations of the strong angular dispersion in a lithium niobate photonic crystal superprism designed for double (passive and active) demultiplexer applications," Applied Physics Letters **93**(26), 261103 (2008).

[23] M. M. de Lima Jr and P. V. Santos, "Modulation of photonic structures by surface acoustic waves," Reports on Progress in Physics **68**(7), 1639–1701 (2005).

[24] M. Roussey, F. I. Baida, and M.-P. Bernal, "Experimental and theoretical observations of the slow-light effect on a tunable photonic crystal," Journal of the Optical Society of America **24**(6), 1416–1422 (2007).

[25] E. Camargo, H. Chong, and R. De La Rue, “2D Photonic crystal thermo-optic switch based on AlGaAs/GaAs epitaxial structure,” Optics Express **12**, 588–592 (2004).

[26] H. H. J. E. Kicken, P. F. A. Alkemade, R. W. van der Heijden, F. Karouta, R. Nötzel, E. van der Drift, and H. W. M. Salemink, “Wavelength tuning of planar photonic-crystals by local processing of individualholes,” Opt. Express **17**(24), 22,005–22,011 (2009).

[27] H.-S. Kitzerow, A. Lorenz, and H. Matthias, “Tuneable photonic crystals obtained by liquid crystal infiltration,” Phys. Stat. Sol. (a) **204**(11), 3754–3767 (2007).

[28] H. Graener, A. Abdolvand, S. Wackerow, O. Kiriyenko, and W. Hergert, “Optical properties of photonic/plasmonic structures in nanocomposite glass,” Phys. Stat. Sol. (a) **204**(11), 3838–3847 (2007).

[29] J. R. Wendt, G. A. Vawter, P. L. Gourley, T. M. Brennan, and B. E. Hammons, “Nanofabrication of photonic lattice structures in GaAs/AlGaAs,” vol. 11, pp. 2637–2640 (AVS, 1993).

[30] P. L. Gourley, J. R. Wendt, G. A. Vawter, B. T. M., and H. B. E., “Optical properties of two-dimensional photonic lattices fabricated as honeycomb nanostructures in compound semiconductors,” App. Phys. Let. **64**(6), 687 – 689 (1994).

[31] C. C. Cheng and A. Scherer, “Fabrication of photonic band-gap crystals,” vol. 13, pp. 2696–2700 (AVS, 1995).

[32] J. R. Wendt, G. A. Vawter, R. E. Smith, and M. E. Warren, “Nanofabrication of subwavelength, binary, high-efficiency diffractive optical elements in GaAs,” vol. 13, pp. 2705–2708 (AVS, 1995).

[33] C. C. Cheng, V. Arbet-Engels, A. Scherer, and E. Yablonovitch, “Nanofabricated three dimensional photonic crystals operating at optical wavelengths,” Physica Scripta **68**, 17–20 (1996).

[34] C. C. Cheng, A. Scherer, V. Arbet-Engels, and E. Yablonovitch, “Lithographic band gap tuning in photonic band gap crystals,” vol. 14, pp. 4110–4114 (AVS, 1996).

[35] C. C. Cheng, A. Scherer, R.-C. Tyan, Y. Fainman, G. Witzgall, and E. Yablonovitch, “New fabrication techniques for high quality photonic crystals,” vol. 15, pp. 2764–2767 (AVS, 1997).

[36] O. Dial, C. C. Cheng, and A. Scherer, “Fabrication of high-density nanostructures by electron beam lithography,” vol. 16, pp. 3887–3890 (AVS, 1998).

[37] V. V. Poborchii, T. Tada, and T. Kanayama, “A visible–near infrared range photonic crystal made up of Si nanopillars,” Applied Physics Letters **75**(21), 3276–3278 (1999).

[38] T. Zijlstra, E. van der Drift, M. J. A. de Dood, E. Snoeks, and A. Polman, "Fabrication of two-dimensional photonic crystal waveguides for 1.5 mu m in silicon by deep anisotropic dry etching," vol. 17, pp. 2734–2739 (AVS, 1999).

[39] T. Tada, V. V. Poborchii, and T. Kanayama, "Channel waveguides fabricated in 2D photonic crystals of Si nanopillars," Microelectron. Eng. **63**(1), 259–265 (2002).

[40] V. Poborchii, T. Tada, T. Kanayama, and A. Moroz, "Silver-coated silicon pillar photonic crystals: Enhancement of a photonic band gap," Applied Physics Letters **82**(4), 508–510 (2003).

[41] L. Pang, W. Nakagawa, and Y. Fainman, "Fabrication of optical structures using SU-8 photoresist and chemically assisted ion beam etching," Optical Engineering **42**, 2912–2917 (2003).

[42] D. Pustai, A. S. Sharkawy, S. Shi, G. Jin, J. A. Murakowski, and D. Prather, "Characterization and analysis of photonic crystal coupled waveguides," Journal of Microlithography, Microfabrication, and Microsystems **2**, 292–299 (2003).

[43] S. Y. Lin, E. Chow, J. Bur, S. G. Johnson, and J. D. Joannopoulos, "Low-loss, wide-angle Y splitter at approximately 1.6- μm wavelengths built with a two-dimensional photonic crystal," Opt. Lett. **27**(16), 1400–1402 (2002).

[44] H.-B. Sun, A. Nakamura, K. Kaneko, S. Shoji, and S. Kawata, "Direct laser writing defects in holographic lithography-created photonic lattices," Opt. Lett. **30**(8), 881–883 (2005).

[45] L. Pang, W. Nakagawa, and Y. Fainman, "Fabrication of Two-Dimensional Photonic Crystals with Controlled Defects by Use of Multiple Exposures and Direct Write," Appl. Opt. **42**(27), 5450–5456 (2003).

[46] S. Y. Lin, J. G. Fleming, D. L. Hetherington, B. K. Smith, R. Biswas, K. M. Ho, M. M. Sigalas, W. Zubrzycki, S. R. Kurtz, and J. Bur, "A three-dimensional photonic crystal operating at infrared wavelengths," Nature **394**(6690), 251–253 (1998).

[47] J. G. Fleming and S.-Y. Lin, "Three-dimensional photonic crystal with a stop band from 1.35 to 1.95 μm," Opt. Lett. **24**(1), 49–51 (1999).

[48] D. J. W. Aastuen, N. A. Clark, L. K. Cotter, and B. J. Ackerson, "Nucleation and Growth of Colloidal Crystals," Phys. Rev. Lett. **57**(14), 1733– (1986).

[49] D. Sharp, M. Campbell, E. Dedman, M. Harrison, R. Denning, and A. Turberfield, "Photonic crystals for the visible spectrum by holographic lithography," Optical and Quantum Electronics **34**(1), 3–12 (2002).

[50] M. Land, "The physics and biology of animal reflectors," Progress in Biophysics and Molecular Biology **24**, 75–106 (1972).

[51] P. Vukusic, J. R. Sambles, C. R. Lawrence, and R. J. Wootton, "Structural colour: Now you see it [mdash] now you don't," Nature **410**(6824), 36–36 (2001).

[52] J. J. Cowan, “Aztec surface-relief volume diffractive structure,” J. Opt. Soc. Am. A **7**(8), 1529–1544 (1990).

[53] C. J. Summers, N. Curtis, W, and P. W., “Active photonic crystal nano-architectures,” Journal of Nonlinear Optical Physics & Materials **12**(4), 587 – 597 (2003).

[54] B. E. Allman, A. G. Klein, K. A. Nugent, and G. I. Opat, “Lloyd’s mirage: a variant of Lloyd’s mirror,” European Journal of Physics **14**(6), 272–276 (1993).

[55] J. Lekner, “Analysis of Lloyd’s mirror fringes for graded-index reflectors,” J. Opt. Soc. Am. A **13**(9), 1809–1815 (1996).

[56] S. Traut and H. P. Herzig, “Holographically recorded gratings on microlenses for a miniaturized spectrometer array,” Opt. Eng. **39**, 290–298 (2000).

[57] B. E. A. Saleh and M. C. Teich, *Fundamentals of Photonics* (Wiley Interscience, 1991).

[58] D. L. Flamm and V. M. Donnelly, “The design of plasma etchants,” Plasma Chemistry and Plasma Processing **1**(4), 317–363 (1981).

[59] F. H. Dill, “Optical lithography,” IEEE Trans. Electron Devices **22**, 440–444 (1975).

[60] M. Narasimham, “Projection printed photolithographic images in positive photoresists,” Electron Devices, IEEE Transactions on **22**(7), 478–482 (1975).

[61] L. F. Johnson, G. W. Kammlott, and K. A. Ingersoll, “Generation of periodic surface corrugations,” Appl. Opt. **17**(8), 1165–1181 (1978).

[62] C. A. Mack, “Analytical expression for the standing wave intensity in photoresist,” Appl. Opt. **25**(12), 1958–1961 (1986).

[63] S. Kinoshita, S. Yoshioka, and J. Miyazaki, “Physics of structural colors,” Reports on Progress in Physics **71**(7), 076,401 (2008).

[64] E. Walker, “Reduction of photoresist standing-wave effects by post-exposure bake,” Electron Devices, IEEE Transactions on **22**(7), 464–466 (1975).

[65] S. C. Colak, S. Birdogan, E. Aral, and G. KIlIc, “Formation of black glass to be used in solar collectors as absorbent and CuO and Fe2O3’s effect on this glass,” International Journal of Hydrogen Energy **34**(12), 5196 – 5200 (2009).

[66] M. Rothschild, “A roadmap for Optical Lithography,” Optics & Photonics News pp. 26–31 (2010).

[67] D. Daly, R. F. Stevens, M. C. Hutley, and N. Davies, “The manufacture of microlenses by melting photoresist,” Measurement Science and Technology **1**(8), 759–766 (1990).

[68] P. Nussbaum, R. Volkel, H. P. Herzig, M. Eisner, and S. Haselbeck, "Design, fabrication and testing of microlens arrays for sensors and microsystems," Pure and Applied Optics: Journal of the European Optical Society Part A **6**(6), 617–636 (1997).

[69] V. Bardinal, E. Daran, T. Leïchlé, C. Vergnenègre, C. Levallois, T. Camps, V. Conedera, J. B. Doucet, F. Carcenac, H. Ottevaere, and H. Thienpont, "Fabrication and characterization of microlens arrays using a cantilever-based spotter," Opt. Express **15**(11), 6900–6907 (2007).

[70] S. Calixto, "Silicone Microlenses and Interference Gratings," Appl. Opt. **41**(16), 3355–3361 (2002).

[71] B. Päivänranta, P.-Y. Baroni, T. Scharf, W. Nakagawa, M. Kuittinen, and H. P. Herzig, "Antireflective nanostructured microlenses," Microelectronic Engineering **85**(5-6), 1089–1091 (2008).

[72] M. Karlsson and F. Nikolajeff, "Diamond micro-optics: microlenses and antireflection structured surfaces for the infrared spectral region," Opt. Express **11**(5), 502–507 (2003).

[73] C. J. M. van Rijn, "Laser interference as a lithographic nanopatterning tool," J. Microlith., Microfab., Microsyst. **5**(1), 011,012–6 (2006).

[74] B. Päivänranta, N. Heikkilä, and M. Kuittinen, "Antireflective subwavelength-structured surfaces with enhanced color properties," J. Opt. Soc. Am. A **24**(6), 1680–1686 (2007).

[75] T. Clausnitzer, T. Kämpfe, E.-B. Kley, A. Tünnermann, A. V. Tishchenko, and O. Parriaux, "Highly-dispersive dielectric transmission gratings with 100% diffraction efficiency," Opt. Express **16**(8), 5577–5584 (2008).

[76] S. Traut, M. Rossi, and H. P. Herzig, "Replicated arrays of hybrid elements for application in a low-cost micro-spectrometer array," J. Mod. Opt. **47**, 2391–2397 (2000).

[77] H. Ottevaere, R. Cox, H. P. Herzig, T. Miyashita, K. Naessens, M. Taghizadeh, R. Volkel, H. J. Woo, and H. Thienpont, "Comparing glass and plastic refractive microlenses fabricated with different technologies," Journal of Optics A: Pure and Applied Optics **8**(7), 407–429 (2006).

[78] B. Päivänranta, M. Pudas, O. Pitkanen, K. Leinonen, M. Kuittinen, P.-Y. Baroni, T. Scharf, and H.-P. Herzig, "Liquid phase deposition of polymers on arbitrary shaped surfaces and their suitability for e-beam patterning," Nanotechnology **20**(22), 225,305 (2009).

[79] H. Sickinger, J. Schwider, and B. Manzke, "Fiber based Mach-Zehnder interferometer for measuring wave aberrations of microlenses," Optik **110**, 239–243 (1999).

[80] M. Born and E. Wolf, *Principle of Optics* (Cambridge University Press, 1999).

[81] D. Raguin and G. Morris, "Structured Surfaces Mimic Coating Performance," Laser Focus World **33**, 113–117 (1997).

[82] S.-Y. Lin, V. M. Hietala, L. Wang, and E. D. Jones, "Highly dispersive photonic band-gap prism," Opt. Lett. **21**(21), 1771–1773 (1996).

[83] T. Baba, T. Matsumoto, and M. Echizen, "Finite difference time domain study of high efficiency photonic crystal superprisms," Opt. Express **12**(19), 4608–4613 (2004).

[84] F. Glöckler, S. Peters, U. Lemmer, and M. Gerken, "Tunable superprism effect in photonic crystals," physica status solidi (a) **204**(11), 3790–3804 (2007).

[85] A. Jugessur, L. Wu, A. Bakhtazad, A. Kirk, T. Krauss, and R. De La Rue, "Compact and integrated 2-D photonic crystal super-prism filter-device for wavelength demultiplexing applications," Opt. Express **14**(4), 1632–1642 (2006).

[86] K. B. Chung and S. W. Hong, "Wavelength demultiplexers based on the superprism phenomena in photonic crystals," Applied Physics Letters **81**(9), 1549–1551 (2002).

[87] D. Scrymgeour, N. Malkova, S. Kim, and V. Gopalan, "Electro-optic control of the superprism effect in photonic crystals," Appl. Phys. Lett. **82**(19), 3176–3178 (2003).

[88] S. Xiong and H. Fukshima, "Analysis of light propagation in index-tunable photonic crystals," J. Appl. Phys. **94**(2), 1286–1288 (2003).

[89] N. C. Panoiu, M. Bahl, and R. M. Osgood, Jr., "Optically tunable superprism effect in nonlinear photonic crystals," Opt. Lett. **28**(24), 2503–2505 (2003).

[90] T.-H. Pei and Y.-T. Huang, "Temperature Modulation of the Superprism Effect in Photonic Crystals Composed of the Copper Oxide High-Temperature Superconductor," Japanese Journal of Applied Physics **46**(24), 593–595 (2007).

[91] G. Alagappan, X. W. Sun, P. Shum, and M. B. Yu, "Tunable superprism and polarization splitting in a liquid crystal infiltrated two-dimensional photonic crystal made of silicon oxynitride," Opt. Lett. **31**(8), 1109–1111 (2006).

[92] G. Alagappan, X. W. Sun, M. B. Yu, P. Shum, and D. Den Engelsen, "Tunable dispersion properties of liquid crystal infiltrated into a two-dimensional photonic crystal," IEEE Journal of Quantum Electronics **42**, 404–409 (2006).

[93] T. Matsumoto, S. Fujita, and T. Baba, "Wavelength demultiplexer consisting of Photonic crystal superprism and superlens," Opt. Express **13**(26), 10,768–10,776 (2005).

[94] B. Momeni and A. Adibi, "Preconditioned superprism-based photonic crystal demultiplexers: analysis and design," Appl. Opt. **45**(33), 8466–8476 (2006).

[95] A. Lupu, E. Cassan, S. Laval, L. E. Melhaoui, P. Lyan, and J. Fedeli, "Experimental evidence for superprism phenomena in SOI photonic crystals," Opt. Express **12**(23), 5690–5696 (2004).

[96] X. Ao, L. Liu, L. Wosinski, and S. He, "Polarization beam splitter based on a two-dimensional photonic crystal of pillar type," Appl. Phys. Lett. **89**(17), 171,115–3 (2006).

[97] T. Xu, N. Zhu, M. Y.-C. Xu, L. Wosinski, J. S. Aitchison, and H. E. Ruda, "A pillar-array based two-dimensional photonic crystal microcavity," Appl. Phys. Lett. **94**(24), 241,110–3 (2009).

[98] S. G. Johnson and J. D. Joannopoulos, "Block-iterative frequency-domain methods for Maxwell's equations in a planewave basis," Opt. Express **8**(3), 173–190 (2001).

[99] A. Lupu, A. de Lustrac, A. Ourir, X. Checoury, J.-M. Lourtioz, E. Centeno, D. Cassagne, J.-P. Albert, F. Pommereau, L. Legouezigou, O. Drisse, O. Legouezigou, E. Deroin, and G.-H. Duan, "Discontinuous wavelength super-refraction in photonic crystal superprism," Opt. Express **14**(5), 2003–2013 (2006).

[100] J. Witzens, M. Hochberg, T. Baehr-Jones, and A. Scherer, "Mode matching interface for efficient coupling of light into planar photonic crystals," Phys. Rev. E **69**(4), 046,609 (2004).

[101] F. J. Lawrence, L. C. Botten, K. B. Dossou, and C. M. de Sterke, "Antireflection coatings for two-dimensional photonic crystals using a rigorous impedance definition," Applied Physics Letters **93**(12), 121114 (2008).

[102] A. Thorne, U. Litzn, and S. Johansson, *Spectrophysics: Principles and Applications* (Springer-Verlag Berlin, 1999).

[103] H. E. Cline and T. R. Anthony, "Heat treating and melting material with a scanning laser or electron beam," Journal of Applied Physics **48**(9), 3895–3900 (1977).

[104] D. Bernier, X. L. Roux, A. Lupu, D. Marris-Morini, L. Vivien, and E. Cassan, "Compact, low cross-talk CWDM demultiplexer using photonic crystal superprism," Opt. Express **16**(22), 17,209–17,214 (2008).

[105] H.-S. Kitzerow and J.-P. Reithmaier, *Photonic Crystals: Advances in Design, Fabrication and Characterization* (Wiley-VCH, 2004). Chap.9.

[106] M. Roussey, M.-P. Bernal, N. Courjal, D. V. Labeke, F. I. Baida, and R. Salut, "Electro-optic effect exaltation on lithium niobate photonic crystals due to slow photons," Applied Physics Letters **89**(24), 241110 (pages 3) (2006).

[107] P. Weinberger, "John Kerr and his effects found in 1877 and 1878," Philosophical Magazine Letters **88**(12), 897–907 (2008).

[108] G. E. Town, A. Vasdekis, and I. D. W. Turnbull, G. A. andSamuel, "Temperature tuning of a semiconducting-polymer DFB laser," Proc. LEOS 2005 p. 763 (2005).

[109] I. Märki, M. Salt, and H. P. Herzig, "Tuning the resonance of a photonic crystal microcavity with an AFM probe," Opt. Express **14**(7), 2969–2978 (2006).

[110] J. Martz, R. Ferrini, F. Nüesch, L. Zuppiroli, B. Wild, L. Dunbar, R. Houdré, M. Mulot, and S. Anand, "Liquid crystal infiltration of InP-based planar photonic crystals," Journal of Applied Physics **99**, 103,105 (2006).

[111] K. Takatoh, M. Hasegawa, M. Koden, N. Itoh, R. Hasegawa, and M. Sakamoto, *Alignment technologies and applications of liquid crystal devices*, The liquid crystals book series (Taylor & Francis, 2005).

[112] S. W. Leonard, J. P. Mondia, H. M. van Driel, O. Toader, S. John, K. Busch, A. Birner, U. Gösele, and V. Lehmann, "Tunable two-dimensional photonic crystals using liquid crystal infiltration," Phys. Rev. B **61**(4), 2389– (2000).

[113] G. Mertens, T. Roder, H. Matthias, H. Marsmann, H.-S. R. Kitzerow, S. L. Schweizer, C. Jamois, R. B. Wehrspohn, and M. Neubert, "Two- and three-dimensional photonic crystals made of macroporous silicon and liquid crystals," Applied Physics Letters **83**(15), 3036–3038 (2003).

[114] C. Schuller, F. Klopf, J. P. Reithmaier, M. Kamp, and A. Forchel, "Tunable photonic crystals fabricated in III-V semiconductor slab waveguides using infiltrated liquid crystals," Applied Physics Letters **82**(17), 2767–2769 (2003).

[115] H. H. J. E. Kicken, I. Barbu, R. W. van der Heijden, F. Karouta, R. Nötzel, E. van der Drift, and H. W. M. Salemink, "Wavelength-sized, tunable nanocavity in deeply etched InP/InGaAsP/InP photonic crystals," Opt. Lett. **34**(14), 2207–2209 (2009).

[116] M. A. Dundar, H. H. J. E. Kicken, A. Y. Silov, R. Notzel, F. Karouta, H. W. M. Salemink, and R. W. van der Heijden, "Birefringence-induced mode-dependent tuning of liquid crystal infiltrated InGaAsP photonic crystal nanocavities," Applied Physics Letters **95**(18), 181111 (2009).

[117] R.-P. Pan, C.-F. Hsieh, C.-L. Pan, and C.-Y. Chen, "Temperature-dependent optical constants and birefringence of nematic liquid crystal 5CB in the terahertz frequency range," Journal of Applied Physics **103**(9), 093523 (2008).

[118] T. Scharf, *Polarized light in liquid crystals and polymers* (Wiley Interscience, 2006).

Acknowledgements

I would like to express my gratitude to all the people who have been involved and have supported me morally and by their acts during the last five years I have been working at the *Institut de Microtechnique* as a PhD student and as an assistant in lectures, semester and diploma works for bachelor and master students.

- First of all, I would like to thank Professor Hans Peter Herzig, my thesis director, to have let me enter his research group and to have made the working atmosphere pleasant and constructive.

- The successive supervisors I have had the pleasure to experience: Dr. Toralf Sharf and his incomparable sense of humor who I would like to thank for his availability and his continuous input of new ideas. Prof. Wataru Nakagawa and his American sweeties who I am grateful for his availability and the rigor when we were about to publish an article.
- Dr. Matthieu Roussey and his friendship around coffees or elsewhere for the supplied help.

- Thanks to Vincent Paeder for the interesting discussions and Qing Tan who bore me as her office colleague and most of all for the simulations on photonic crystal structures they provided me.

- The e-beam fabricated devices could not have been tested if Yu-Chi Chang and Armando Cosentino would not have fabricated them. Thanks very much for that.

- For their support and friendship I would like to thank: Dr. Patrick Ruffieux specially for his competencies to repair the Reactive Ion Etching machine, Irène Philipoussis for the *clean room* skills and the bursts of laughter, Dr. Iwan Märki for the cordial welcome at the very beginning and the kind introduction to the nanoworld and Dr.

Olivier Scherler for his swiftness to debug various systems.

- For the friendly and open environment I would like to thank all the members of the applied optics group and more generally of the institute of microtechnology.

- Finally, most importantly I thank my beloved women Cindy and Chiara for their encouragements, patience, love and support during all the last years.

Curriculum vitae

Pierre-Yves Baroni
Rue des Vernes 14
2013 Colombier
Suisse
Tél. : +41 32 841 10 04
Année de naissance : 1979

Etudes

2005–2010	Assistant doctorant dans le Laboratoire d'Optique Appliqué de l'Institut de Microtechnique de l'Ecole Polytechnique Fédérale de Lausanne (EPFL).
2004	Certificat de réalisation du degré " Advanced " en anglais.
1998–2003	Diplôme d'ingénieur en microtechnique à l'Ecole Polytechnique Fédérale de Lausanne. Orientation : Photonique Appliquée.
1995–1998	Maturité fédérale scientifique au Gymnase Cantonal de Neuchâtel.

Expérience

2005–2010	Travail de thèse sur la fabrication et caractérisation de structure périodique sous-longueur d'onde par lithographie interférenciel. Caractérisation de structures optiques résonnantes et de superprisme. Encadrement d'étudiants lors de cours, de projets de semestre et de master.
2002–2003	Projet de diplôme (EPFL): Structuration de TCO par différentes méthodes. En collaboration avec un partenaire industriel.
2003	Projet de semestre : Observation d'objet de phase en microscopie à l'aide de cristaux liquide.
2002	Projet de semestre : Détection de plasmon de surface sur couche d'or.

Langues

Français : langue maternelle.
Anglais : courant.
Allemand : connaissance scolaire.

Divers

Judo : ceinture noire 2ème Dan, Ancien compétiteur individuel et par équipe (LNA), Entraîneur de judo, actifs dans différent comité en tant que responsable de manifestation et activité.
Président de l'Association Neuchâteloise de Judo depuis 2008.

Références

M. Toralf Scharf, Privat-Docent IMT Neuchâtel, Ch. Des Trois Portes 18, 2000 Neuchâtel, tél. +41 32 731 7132.
M. Stéphane Guye, Professeur diplômé de judo, Petite-Berne 5, 2035 Corcelles, tél.+41 32 7312554.